

CHARACTERIZING EXOPLANET ATMOSPHERES: FROM LIGHT-CURVE
OBSERVATIONS TO RADIATIVE-TRANSFER MODELING

by

PATRICIO E. CUBILLOS
B.Sc. Universidad de Chile, 2006
M.Sc. Universidad de Chile, 2011

A dissertation submitted in partial fulfillment of the requirements
for the degree of Doctor of Philosophy in Physics, Planetary Sciences Track
in the Department of Physics
in the College of Sciences
at the University of Central Florida
Orlando, Florida

Fall Term
2015

Major Professor: Joseph Harrington

© 2015 Patricio E. Cubillos

ABSTRACT

Multi-wavelength transit and secondary-eclipse light-curve observations are some of the most powerful techniques to probe the thermo-chemical properties of exoplanets. Although the large planet-to-star brightness contrast and few available spectral bands produce data with low signal-to-noise ratios, a Bayesian approach can robustly reveal what constraints we can set, without over-interpreting the data. Here I performed an end-to-end analysis of transiting exoplanet data. I analyzed space-telescope data for three planets to characterize their atmospheres and refine their orbits, investigated correlated noise estimators, and contributed to the development of the respective data-analysis pipelines. Chapters 2 and 3 describe the Photometry for Orbits, Eclipses and Transits (POET) pipeline to model Spitzer Space Telescope light curves. I analyzed secondary-eclipse observations of the Jupiter-sized planets WASP-8b and TrES-1, determining their day-side thermal emission in the infrared spectrum. The emission data of WASP-8b indicated no thermal inversion, and an anomalously high 3.6 micron brightness. Standard solar-abundance models, with or without a thermal inversion, can fit the thermal emission from TrES-1 well. Chapter 4 describes the most commonly used correlated-noise estimators for exoplanet light-curve modeling, and assesses their applicability and limitations to estimate parameter uncertainties. I show that the residual-permutation method is unsound for estimating parameter uncertainties. The time-averaging and the wavelet-based likelihood methods improve the uncertainty estimations, being within 20 – 50% of the expected value. Chapter 5 describes the open-source Bayesian Atmospheric Radiative Transfer (BART) code to characterize exoplanet atmospheres. BART combines a thermochemical-equilibrium code, a one-dimensional line-by-line radiative-transfer code, and

the Multi-core Markov-chain Monte Carlo statistical module to constrain the atmospheric temperature and chemical-abundance profiles of exoplanets. I applied the BART code to the Hubble and Spitzer Space Telescope transit observations of the Neptune-sized planet HAT-P-11b. BART finds an atmosphere enhanced in heavy elements, constraining the water abundance to 100 times that of the solar abundance.

ACKNOWLEDGMENTS

It's fascinating how these six years at UCF turned out to be much more than just a PhD degree. It certainly went beyond expectations in all aspects, because not only did I had to be a student or researcher, I also had to play the role of a colleague, a teacher, a shrink, a patient, a friend, an much more. This period has been a true life experience with all the ups and downs, it's been at times as hard, hopeless, and lonely as it's been fun, exciting, and fulfilling. Of course, I couldn't have accomplished everything I did without the contributions of many others. First, I have to thank my advisor Joseph Harrington. I really appreciate how much I have learned from you, not only your direct instruction but also your thoroughness and work ethics. I can only regard you with the most respect. I also have to thank Jasmina Blecic. I don't think there is any other person I have argued with so much and so many times, yet I'm still glad to see again. I'm deeply grateful for your advice in the office and especially for your advice out of the office. I really enjoyed having you as a friend and I'm sure I couldn't have graduated without your help. I thank Alejandra, you have been a terrific friend, thanks for your company and support when needed. Thanks to my family for their unconditional support, to all the friends and workmates I met while at UCF, to Nicolas Massu for reminding us that "nada es imposible", and many thanks to Jennifer Parham for taking so much bureaucracy off of my shoulders.

NOTES ABOUT CONTRIBUTIONS FROM COAUTHORS

The work presented in this dissertation consists of published and in-preparation journal articles, each the result of a collaborative effort amongst the coauthors listed in each chapter. Unless otherwise stated below, I have reworded contributed text from coauthors without changing the ideas or implications behind the text. The paragraphs below describe the specific contributions made in each paper using the initials of each author.

In Chapter 2 P.C. wrote the paper with contributions from J.H., N.M., K.S., R.A.H., J.B., D.R.A., M.H., C.J.C; P.C. reduced the data; N.M. produced the atmospheric models.; R.A.H. produced the orbital parameter results; P.C. and J.H. analyzed the results; J.H. developed the POET analysis pipeline in IDL. K.S., P.C., C.J.C, and R.A.H. adapted POET for Python. P.C. implemented the orbital thermal variation model.

In Chapter 3 P.C. wrote the paper with contributions from J.H., N.M., A.S.D.F., N.B.L., R.A.H., M.O.B.; P.C. reduced the data; A.S.D.F. produced the orbital parameter results with contribution from R.A.H.; N.M. produced the atmospheric models; P.C. and J.H. analyzed the results; P.C. implemented the DEMC algorithm, N.B.L. implemented the least-asymmetry methods.

In Chapter 4 P.C. wrote the paper with contributions from J.H. and T.J.L., N.B.L., J.B., and M.S.; T.J.L. provided the statistical background for the residual-permutation method conclusions. P.C. designed and carried out the simulations; P.C. analyzed the results; P.C. wrote the MC³ module with contribution from N.B.L. and M.S.

In Chapter 5, P.C. wrote the paper with contribution from J.H., J.B., R.C.C. and S.D.B.; P.C. analyzed the HAT-P-11b transit data and ran the HAT-P-11b atmospheric analysis.

Regarding the BART code implementation: J.H. is the architect of BART, specifying the components and the information flow between them, identifying major areas of required effort, and assigning personnel to programming and documentation tasks. P.C. reviewed and documented the original Transit code, implemented the opacity-grid calculation, opacity-grid interpolation, Voigt-function pre-calculation, filter-transmission integration; P.C. wrote the MC³ module documentation; P.C., J.B., R.C.C wrote the Transit module documentation with contribution from A.J.F.; P.C. developed the code to read the HITRAN, P&S, Schwenke, and Plez line-transition files; P.C. implemented the MC³ module with contribution from N.B.L. and M.S.; P.C., M.M.S., N.B.L., and A.S.D.F. implemented the MPI communication framework; P.C. and M.M.S. implemented the three-channel Eddington-approximation model; P.C. and M.M.S. reimplemented the C linereader into Python; P.C. implemented the CTIPS module with contribution from A.J.F.; P.C. and R.C.C. implemented the C Simpson integration and spline interpolation routines with contribution from S.D.B..

S.D.B. implemented the VO partition-function code with contribution from P.C.; S.D.B. tested Transit and provided feedback for P.C. to further develop Transit; D.B. implemented HITRAN CIA reader with contribution from P.C..

P.M.R. provided original version of Transit; M.M.S. imported Transit from SVN into Github; A.J.F. redesigned the Transit compilation scripts with contribution from A.S.D.F.; N.B.L. implemented SWIG wrapped to run Transit from Python and several performance speed ups to Transit; J.B. and M.O.B. implemented and wrote documentation for TEA with contribution from M.M.S.; C.M. computed independent radiative-transfer spectra for comparison with Transit; A.J.F. added support for shared memory in BART/Transit. J.B. implemented the contribution-function, best-fit calculations, eclipse-geometry radiative-transfer code. R.C.C. implemented the HITRAN cross-section reader for Transit; R.C.C., J.G., A.J.F., A.S.D.F. contributed in low-level tasks in the development of BART/Transit.

TABLE OF CONTENTS

LIST OF FIGURES	xv
LIST OF TABLESxviii
CHAPTER 1: INTRODUCTION	1
1.1 Exoplanet Characterization	2
1.2 Atmospheric Modeling and Retrieval	5
1.3 List of References	7
CHAPTER 2: WASP-8b: CHARACTERIZATION OF A COOL AND ECCENTRIC EXO- PLANET WITH SPITZER	11
2.1 Abstract	12
2.2 Introduction	12
2.3 Observations	15
2.4 Data Analysis	17
2.4.1 POET: Initial Reduction	17
2.4.2 Centering	18
2.4.3 Photometry	19

2.4.4	Light-curve Modeling	20
2.4.4.1	wa008bs11 Analysis	23
2.4.4.2	wa008bs23 Analysis	26
2.4.4.3	wa008bs21 & wa008bs41 Analysis	28
2.4.4.4	wa008bs22 & wa008bs42 Analysis	31
2.4.4.5	Final Joint-fit Analysis	33
2.5	Orbital Dynamics	33
2.6	Atmospheric Analysis	36
2.7	The Unexpected Brightness Temperature of WASP-8b	39
2.8	Conclusions	43
2.9	Acknowledgments	46
2.10	List of References	46
CHAPTER 3: A SPITZER FIVE-BAND ANALYSIS OF THE JUPITER-SIZED PLANET		
	TrES-1	53
3.1	Abstract	54
3.2	Introduction	54
3.3	Observations	56

3.4	Data Analysis	58
3.4.1	Optimal Photometry	59
3.4.2	Light Curve Modeling	60
3.4.3	Differential Evolution Markov Chain	63
3.4.4	Data Set and Model Selection	64
3.4.5	Light Curve Analyses	65
3.4.5.1	IRAC-3.6 μm Eclipse	66
3.4.5.2	IRAC-4.5 μm Eclipse	68
3.4.5.3	IRAC-5.8 μm Eclipse	72
3.4.5.4	IRAC-8.0 μm Eclipse	74
3.4.5.5	IRS-16 μm Eclipses	75
3.4.5.6	IRS-16 μm Transit	78
3.4.5.7	Joint-fit Analysis	79
3.4.5.8	4.5 and 8.0 μm Eclipse Reanalyses	83
3.5	Orbital Dynamics	84
3.6	Atmosphere	85
3.7	Conclusions	87

3.8	Acknowledgements	89
3.9	Joint Best Fit	90
3.10	Light Curve Data Sets	95
3.11	List of References	95

CHAPTER 4: ON CORRELATED-NOISE ANALYSES APPLIED TO EXOPLANET LIGHT
CURVES 101

4.1	Abstract	102
4.2	Introduction	103
4.3	Model-Fitting Estimation	105
4.3.1	Overview	105
4.3.2	Time Averaging	107
4.3.2.1	Gaussian-noise Test	109
4.3.3	Residual Permutation	111
4.3.4	Wavelet Analysis	112
4.3.4.1	Wavelet-based Likelihood	113
4.3.4.2	Wavelet-likelihood Errata	114
4.4	Correlated-noise Tests for Exoplanet Eclipse Data	114

4.4.1	Synthetic-noise Simulation	115
4.4.1.1	Results	119
4.4.2	Long-duration Synthetic-noise Simulation	121
4.4.3	Simulation with Spitzer-IRAC Noise	122
4.5	Multi-Core Markov-Chain Monte Carlo (MC ³) Code	125
4.6	Conclusions	127
4.7	Acknowledgements	130
4.8	Bayesian Credible Region	130
4.9	Standard Deviation Uncertainty	131
4.10	Wavelet Coefficients Variance	134
4.11	List of References	136
CHAPTER 5: THE BAYESIAN ATMOSPHERIC RADIATIVE TRANSFER CODE FOR		
EXOPLANET MODELING AND APPLICATION TO THE EXOPLANET		
HAT-P-11b 141		
5.1	Abstract	142
5.2	Introduction	143
5.2.1	Atmospheric Modeling and Retrieval	143
5.3	The Bayesian Atmospheric Radiative Transfer Package	146

5.3.1	Thermochemical Equilibrium Abundance Module	148
5.3.2	Atmospheric Model Generator	149
5.3.2.1	Temperature Profile	149
5.3.2.2	Molecular-Abundance Profiles	150
5.3.2.3	Altitude – Pressure	151
5.3.3	Radiative Transfer	151
5.3.3.1	Transit Geometry	154
5.3.3.2	Eclipse Geometry	157
5.3.3.3	Collision-induced Absorption	159
5.3.3.4	Line-transition Absorption	159
5.3.3.5	Opacity Databases	161
5.3.4	Spectrum Band Integration	165
5.3.5	Statistical MCMC Driver	166
5.3.5.1	MC ³ Usage for BART	167
5.3.6	Retrieval Validation Test	167
5.4	Application to HAT-P-11b	169
5.4.1	Analysis of the Spitzer Data	170

5.4.2	Atmospheric Retrieval	173
5.5	Discussion	178
5.5.1	Open Source, Open Development	178
5.5.2	Conclusions	179
5.6	Acknowledgements	182
5.7	List of References	182

LIST OF FIGURES

2.1	<i>Spitzer</i> images of WASP-8b	16
2.2	Secondary-eclipse light curves of WASP-8b	24
2.3	Residuals RMS vs. bin size	25
2.4	wa008bs23 target pointing, position angle, and sky flux	27
2.5	wa008bs21 standard deviation of the normalized residuals vs. aperture	29
2.6	Eclipse depth vs. A aperture for wa008bs21	30
2.7	Joint wa008bs21 and wa008bs41 standard deviation of the normalized residuals vs. aperture radius	31
2.8	Atmospheric models of WASP-8b	38
2.9	Model brightness-temperature lightcurves of WASP-8b	42
3.1	<i>Spitzer</i> detector pointing	58
3.2	3.6- μm detector pointing.	61
3.3	Light curve's SNDR and eclipse depth at 3.6 μm	67
3.4	TrES-1 secondary-eclipse light curves and rms-vs.-bin size plots	69
3.5	Per-AOR mean <i>Spitzer</i> frames at 4.5 μm	70
3.6	Light curve's SNDR and eclipse depth at 4.5 μm	72

3.7	Light curve's SNDR and eclipse depth at 5.8 μm	73
3.8	Light curve's SNDR and eclipse depth at 8.0 μm	74
3.9	Light curve's SNDR and eclipse depth at 16.0 μm	76
3.10	Light curve's SNDR and planet-to-star radius ratio at 16.0 μm	79
3.11	Raw, binned, and systematics-corrected normalized TrES-1 transit light curves at 16 μm	80
3.12	Eclipse-midpoint pairwise and marginal posteriors	82
3.13	Dayside atmospheric spectral emission and Spitzer-band contribution func- tions of TrES-1	87
4.1	Binned residuals rms vs. bin size of WASP-8b Spitzer eclipse	109
4.2	rms vs. bin size for a zero-mean normal-distribution	110
4.3	Simulated Spitzer time-series data sets	117
4.4	β distributions	118
4.5	Distribution of estimated eclipse-depth uncertainties	120
4.6	Distribution of estimated eclipse-depth uncertainties for the time-averaging analysis	121
4.7	Distribution of estimated eclipse-depth uncertainties	124
5.1	BART flow chart	147

5.2	Transit flow chart	153
5.3	Diagram for transit-geometry observation	155
5.4	Diagram for eclipse-geometry observation	157
5.5	Model emission spectra for pure collision-induced absorption	162
5.6	Model planet-to-star flux ratio spectra for water, carbon monoxide, carbon dioxide, and methane	164
5.7	Near-infrared titanium- and vanadium-oxide opacity spectra	165
5.8	Retrieval for a synthetic model spectrum	168
5.9	Fit residuals' rms vs. bin size for second visit at 3.6 μm	174
5.10	Normalized, systematics-corrected Spitzer HAT-P-11b transit light curves . .	176
5.11	HAT-P-11b retrieval transmission spectra and atmosphere	177

LIST OF TABLES

2.1	Observation Information	15
2.2	WASP-8 System	16
2.3	wa008bs11 Ramp Model Fits	23
2.4	wa008bs23 Ramp Model Fits	26
2.5	wa008bs21 Ramp Model Fits	28
2.6	wa008bs41 Ramp Model Fits	30
2.7	wa008bs22 Ramp Model Fits	32
2.8	wa008bs42 Ramp Model Fits	32
2.9	Best-fit Eclipse Light-curve Parameters	34
2.10	Eccentric Orbital Model	35
3.1	Observation Information	57
3.2	3.6- μm Eclipse - Ramp Model Fits	66
3.3	4.5- μm Eclipse - Ramp Model Fits	71
3.4	5.8- μm Eclipse - Ramp Model Fits	73
3.5	8.0- μm Eclipse - Ramp Model Fits	75

3.6	16- μm Eclipse, Visit 2—Individual Ramp Model Fits	75
3.7	16- μm Eclipse, Visit 3—Individual Ramp Model Fits	77
3.8	16- μm Eclipse, Visit 1—Ramp Model Fits	77
3.9	16- μm Transit—Ramp Model Fits	78
3.10	3.6- μm Eclipse Models—Eclipse-joint Fits	81
3.11	Midpoint per Waveband—Eclipse-joint Fit	81
3.12	Eclipse-depth Reanalysis	83
3.13	MCMC Eccentric Orbital Model	85
3.14	Best-Fit Eclipse Light Curve Parameters	91
3.15	TrES-1 Radial-velocity Data	92
3.16	TrES-1 Transit Midpoint Data	93
3.16	TrES-1 Transit Midpoint Data — (Continued)	94
4.1	Synthetic Light-curve Parameters	115
4.2	$\sigma_{\mathcal{N}}$ for Synthetic-data Sets	119
4.3	$\sigma_{\mathcal{N}}$ for the HD 209458b Sets	123
5.1	3.6 μm Visit 1 - Ramp Model Fits	172
5.2	3.6 μm Visit 2 - Ramp Model Fits	172

5.3	4.5 μm visit 1 - Ramp Model Fits	173
5.4	4.5 μm visit 2 - Ramp Model Fits	173
5.5	HAT-P-11b Best Joint-fit Eclipse Light-curve Parameters	175

CHAPTER 1: INTRODUCTION

The study of planets orbiting stars other than the Sun, exoplanets, has become one of the most exciting and fastest-growing fields of astronomy. Since the first exoplanet detection (Mayor & Queloz 1995), the discovery rate has increased exponentially, reaching nearly two thousand confirmed exoplanets to date. There are multiple methods to detect exoplanets, the radial-velocity and transit techniques being the most successful. The radial-velocity method uses high-precision spectrographs to measure the radial velocity of stars. Planet-hosting stars show periodic oscillations around the center of mass of the system. The radial-velocity signal is proportional to the mass of the planet. The transit method monitors the flux of stars as a function of time. If a planet's orbit is aligned such that the planet crosses in front of the star as observed from Earth (a "transit"), the telescope detects the drop of the flux blocked by the planet. The transit signal is proportional to the size of the planet. Given the observational biases of the detection methods, the first objects detected were large and massive planets orbiting extremely close to their host stars; they were named "hot Jupiters".

The further arrival of dedicated, state-of-the-art facilities allowed for important breakthroughs. High-precision spectrographs, like the High Accuracy Radial Velocity Planet Searcher (HARPS, Mayor et al. 2003) and photometers, like the Kepler Space Telescope, yielded the first estimations of the exoplanetary occurrence rate in the Milky Way. Our galaxy hosts billions of planets, with Earth-sized planets the most frequent. To highlight some findings, Fressin et al. (2013) estimated that 52% of stars host at least one exoplanet, Dressing & Charbonneau (2015) determined a planet occurrence rate of 2.5 ± 0.2 planets per M dwarf star, and Bonfils et al. (2013) estimated the fraction of habitable planets around M dwarf stars at 0.41^{+54}_{-13} .

Building on these statistics, future dedicated missions, like the Transiting Exoplanet Survey Satellite (TESS, Ricker et al. 2014), the Next Generation Transit Survey (NGTS, Wheatley et al. 2013), or the Characterizing ExOPlanet Satellite (CHEOPS) mission (Broeg et al. 2013), are expected to find thousands of exoplanets around the brightest stars in the Solar neighborhood. These planets will be the best-suited targets for characterization.

1.1 Exoplanet Characterization

Although exoplanets can hardly be better characterized than any Solar-System planet, their value resides in their much larger number and diversity (Cowan et al. 2015). Exoplanets provide a far more comprehensive view of planetary physics than what we can learn from the Solar System alone. However, to date, no categorization has fully succeeded to describe the observed physical properties of the aggregate of known exoplanets. For example, Fortney et al. (2008) proposed a classification of hot Jupiters based on the incident irradiation. The most highly irradiated planets would show thermal inversions due to TiO and VO absorption. However, subsequent observations and studies challenged the predictions and mechanism of this classification (e.g., Knutson et al. 2010, Spiegel et al. 2009, Madhusudhan 2012). Cowan & Agol (2011) studied the Bond albedo from a sample of 24 exoplanets. They found low albedos, but detected no clear trends between the estimated equilibrium temperatures (an estimation of the planet's energy budget) and the observed effective temperatures. The observed population of exoplanets shows a large diversity of properties; therefore, classifying them is a complex and multi-dimensional problem.

Transiting exoplanets are the most favorable targets for characterization. These planets pass in front and behind their host stars, as seen from Earth, leaving a characteristic signature in the systems' light curves. By combining photometric and radial-velocity measurements, we can constrain their bulk size and mass, and hence, constrain their average density. A further spectral analysis of their time-series photometry allows for atmospheric characterization.

When a planet passes in front of its host star, a transit event, the fraction of light that is blocked, the transit depth, is proportional to the planet-to-star area ratio, constraining the bulk size of the planet. In this configuration, the planetary atmospheric composition modulates the stellar light that travels across the planet's limb (the day-night terminator). Opaque absorbing gasses make the planet look larger. Each atmospheric species imprints a characteristic absorbing pattern as a function of wavelength. Hence, the variation of the transit depth across wavelengths (the modulation spectrum), constrains the composition of the planetary atmosphere. The magnitude of the modulation variation is proportional to the atmospheric scale height, making a transit observation sensitive to the bulk density of the atmosphere as well. Given the geometry of the light ray paths, even low concentrations of an absorber can have a large impact in the modulation spectrum. For the same token, high-altitude haze layers quickly flatten out a spectrum (e.g., Kreidberg et al. 2014, Knutson et al. 2014). Nonetheless, cloudless counter-examples have been observed (e.g., Fraine et al. 2014).

When a planet passes behind its host star (a secondary-eclipse event), the fraction of blocked light is proportional to the thermal (infrared) or reflected (optical) planetary emission. Similar to the transit modulation spectrum, the eclipse depth as a function of wavelength constrains the atmospheric composition and temperature of the integrated day-side hemisphere. The shape of the light curve during ingress and egress constrains the two-dimensional planetary emission pattern (de Wit et al. 2012, Majeau et al. 2012). As the projection of the stellar limb progressively occults and uncovers fractions of the planetary disk, we can relate the flux variation to specific regions on the

planet. Additionally, since the stellar limb at ingress crosses the planetary disk at a different angle than at egress (for an imperfectly edge-on orbit), the time-resolved occultation of the planet allows for a two-dimensional mapping of the emission. For an edge-on orbit, a one-dimensional longitudinal map can still be recovered. Furthermore, a multi-wavelength face mapping would constrain the compositional and temperature variation over the planet surface, putting to test circulation (Showman et al. 2013) and chemical kinetics (Agúndez et al. 2012) theories. Both transit and eclipse spectra around the infrared–visible boundary are also sensitive to Rayleigh scattering (e.g., Biddle et al. 2014).

Finally, measuring the flux of a system along a whole orbit, a phase-curve, allows one to construct a longitudinal phase map of the planetary emission. Only a phase curve can break the degeneracy between the albedo and the day–night energy redistribution. By measuring both the day- and night-side emission, the total emission constrains the energy budget of a planet, whereas the day-to-night temperature contrast constrains the heat redistribution. The longitudinal variation pattern will allow us to infer the general dynamical circulation regime of the atmosphere.

Astronomers have used many ground-based and space facilities to characterize exoplanets in the infrared. Among these, the Spitzer and Hubble space telescopes have provided the most fruitful results. The Spitzer Space Telescope had six broad wavebands covering the 3.6–24 μm range during its cryogenic mission (2003 to 2009). Since then, only the two shortest-wavelength bands (3.6 and 4.5 μm) remain in use. On the other hand, the Hubble Space Telescope’s (HST) spectrograph, the Wide Field Camera 3 (installed in 2009), covers the 1.1–1.7 μm range at a spectral resolution of $\lambda/\Delta\lambda \sim 75$. Note that most of the available instrumentation was not conceived for exoplanet observations. Thus, to succeed, scientists have resorted to observing techniques and post-acquisition calibrations, allowing them to extract signals even fainter than the instruments’ photometric design criteria.

1.2 Atmospheric Modeling and Retrieval

Modeling planetary atmospheres is a multi-disciplinary endeavor, involving radiative processes, atmospheric chemistry, circulation dynamics, cloud physics, etc. The radiative-transfer equation ultimately links the observed spectra (transit or eclipse depths) to the atmospheric properties. The temperature, pressure, and absorbing species abundances are the main factors that determine the resulting spectrum. However, gases that are not spectroscopically active are also important, as they contribute to the bulk density of the atmosphere or modify the abundance of the absorbing gases through chemical reactions.

In general, two data-modeling approaches prevail: forward modeling and retrieval. In the forward-modeling approach, the researcher heuristically adjusts the parameters of a model until it resembles the data well. On the other hand, the retrieval approach uses algorithms that explore and constrain the parameter phase space of a model, given the existing data; for example, a Bayesian retrieval approach uses Markov-chain Monte Carlo (MCMC) algorithms. Currently, exoplanet data is sparse and of low signal-to-noise ratios, often leading to large parameter uncertainties and degenerate solutions. Therefore, the retrieval approach is at an advantage over the forward-modeling approach, since it provides an exhaustive exploration, and statistically-robust constraints of the parameters' phase space. Madhusudhan & Seager (2010) first applied the retrieval approach to characterize exoplanet atmospheres. Quickly after, others groups developed their own retrieval tools (e.g., Lee et al. 2012, Line et al. 2013, Benneke & Seager 2012, Waldmann et al. 2015).

In general, the radiative-transfer problem alone is well understood, though there is a lack of opacity data at temperatures above ~ 1000 K. The statistical treatment varies among the different groups, without a clear superior algorithm so far. More importantly, it is still little understood how radiative processes, equilibrium and disequilibrium chemistry, circulation, and cloud physics combine to determine the atmospheric abundances. Hence, the parameterization and priors of the atmospheric

composition remain one of the most open modeling aspects. The priors (i.e., observational or theoretical constraints) guide—and generally improve—the phase space exploration, limiting the MCMC to physically-plausible regions. How one parameterizes the models affects the statistical treatment efficiency, for example, reducing correlations between parameters. However, the most efficient parameterizations are not necessarily the easiest to interpret in physical terms.

A clear obstacle in laying out significant constraints has been the limited spectral coverage and coarse resolution of current technology (Hansen et al. 2014). However, in the future, better instrumentation will help to overcome these limitations. Expected to be launched in late 2018, the James Webb Space Telescope (JWST) will be the first space telescope truly built for exoplanet characterization. JWST’s unprecedented combination of collecting area, resolving power, and spectral coverage will unveil new and more precise details of these worlds. From the ground, three Extremely-Large Telescopes are planned to start their operations in the 2020s, the Thirty Meter Telescope (TMT), the European Extremely Large Telescope (E-ELT), and the Giant Magellan Telescope (GMT). Together, they will cover both the northern (TMT) and the southern (E-ELT and GMT) hemispheres. Given their much larger collecting area, these telescopes will be optimized to observe fainter targets and perform high resolving-power spectroscopy.

In this work, I analyzed exoplanet secondary eclipse observations and developed an open-source Bayesian retrieval code to model exoplanet atmospheres. The code focuses on developing efficient statistical and radiative-transfer routines. The main goal of the code is to constrain the temperature and composition of exoplanet atmospheres given the available data. To do so, the code explores the phase space of parameterized models of the temperature and species abundances with advanced

MCMC algorithms. In Chapters 2 and 3, I describe the data analysis for Spitzer secondary-eclipse observations for the cases of WASP-8b and TrES-1, respectively. In Chapter 4, I further investigate the statistical methods used in the field to analyze transiting exoplanet data. Finally, in Chapter 5, I describe the Bayesian Atmospheric Radiative Transfer model, provide validation tests, and show the atmospheric analysis for transit observations of the exoplanet HAT-P-11b.

1.3 List of References

- Agúndez, M., Venot, O., Iro, N., Selsis, F., Hersant, F., Hébrard, E., & Dobrijevic, M. 2012, *A&A*, 548, A73
- Benneke, B. & Seager, S. 2012, *ApJ*, 753, 100
- Biddle, L. I., Pearson, K. A., Crossfield, I. J. M., Fulton, B. J., Ciceri, S., Eastman, J., Barman, T., Mann, A. W., Henry, G. W., Howard, A. W., Williamson, M. H., Sinukoff, E., Dragomir, D., Vican, L., Mancini, L., Southworth, J., Greenberg, A., Turner, J. D., Thompson, R., Taylor, B. W., Levine, S. E., & Webber, M. W. 2014, *MNRAS*, 443, 1810
- Bonfils, X., Delfosse, X., Udry, S., Forveille, T., Mayor, M., Perrier, C., Bouchy, F., Gillon, M., Lovis, C., Pepe, F., Queloz, D., Santos, N. C., Ségransan, D., & Bertaux, J.-L. 2013, *A&A*, 549, A109
- Broeg, C., Fortier, A., Ehrenreich, D., Alibert, Y., Baumjohann, W., Benz, W., Deleuil, M., Gillon, M., Ivanov, A., Liseau, R., Meyer, M., Oloffson, G., Pagano, I., Piotto, G., Pollacco, D., Queloz, D., Ragazzoni, R., Renotte, E., Steller, M., & Thomas, N. 2013, in *European Physical Journal Web of Conferences*, Vol. 47, 3005
- Cowan, N. B. & Agol, E. 2011, *ApJ*, 729, 54

Cowan, N. B., Greene, T., Angerhausen, D., Batalha, N. E., Clampin, M., Colón, K., Crossfield, I. J. M., Fortney, J. J., Gaudi, B. S., Harrington, J., Iro, N., Lillie, C. F., Linsky, J. L., Lopez-Morales, M., Mandell, A. M., Stevenson, K. B., & ExoPAG SAG-10. 2015, *PASP*, 127, 311

de Wit, J., Gillon, M., Demory, B.-O., & Seager, S. 2012, *A&A*, 548, A128

Dressing, C. D. & Charbonneau, D. 2015, *ApJ*, 807, 45

Fortney, J. J., Lodders, K., Marley, M. S., & Freedman, R. S. 2008, *ApJ*, 678, 1419

Fraine, J., Deming, D., Benneke, B., Knutson, H., Jordán, A., Espinoza, N., Madhusudhan, N., Wilkins, A., & Todorov, K. 2014, *Nature*, 513, 526

Fressin, F., Torres, G., Charbonneau, D., Bryson, S. T., Christiansen, J., Dressing, C. D., Jenkins, J. M., Walkowicz, L. M., & Batalha, N. M. 2013, *ApJ*, 766, 81

Hansen, C. J., Schwartz, J. C., & Cowan, N. B. 2014, *MNRAS*, 444, 3632

Knutson, H. A., Benneke, B., Deming, D., & Homeier, D. 2014, *Nature*, 505, 66

Knutson, H. A., Howard, A. W., & Isaacson, H. 2010, *ApJ*, 720, 1569

Kreidberg, L., Bean, J. L., Désert, J.-M., Benneke, B., Deming, D., Stevenson, K. B., Seager, S., Berta-Thompson, Z., Seifahrt, A., & Homeier, D. 2014, *Nature*, 505, 69

Lee, J.-M., Fletcher, L. N., & Irwin, P. G. J. 2012, *MNRAS*, 420, 170

Line, M. R., Wolf, A. S., Zhang, X., Knutson, H., Kammer, J. A., Ellison, E., Deroo, P., Crisp, D., & Yung, Y. L. 2013, *ApJ*, 775, 137

Madhusudhan, N. 2012, *ApJ*, 758, 36

Madhusudhan, N. & Seager, S. 2010, *ApJ*, 725, 261

Majeau, C., Agol, E., & Cowan, N. B. 2012, *ApJ*, 747, L20

Mayor, M., Pepe, F., Queloz, D., Bouchy, F., Rupprecht, G., Lo Curto, G., Avila, G., Benz, W., Bertaux, J.-L., Bonfils, X., Dall, T., Dekker, H., Delabre, B., Eckert, W., Fleury, M., Gilliotte, A., Gojak, D., Guzman, J. C., Kohler, D., Lizon, J.-L., Longinotti, A., Lovis, C., Megevand, D., Pasquini, L., Reyes, J., Sivan, J.-P., Sosnowska, D., Soto, R., Udry, S., van Kesteren, A., Weber, L., & Weilenmann, U. 2003, *The Messenger*, 114, 20

Mayor, M. & Queloz, D. 1995, *Nature*, 378, 355

Ricker, G. R., Winn, J. N., Vanderspek, R., Latham, D. W., Bakos, G. Á., Bean, J. L., Berta-Thompson, Z. K., Brown, T. M., Buchhave, L., Butler, N. R., Butler, R. P., Chaplin, W. J., Charbonneau, D., Christensen-Dalsgaard, J., Clampin, M., Deming, D., Doty, J., De Lee, N., Dressing, C., Dunham, E. W., Endl, M., Fressin, F., Ge, J., Henning, T., Holman, M. J., Howard, A. W., Ida, S., Jenkins, J., Jernigan, G., Johnson, J. A., Kaltenegger, L., Kawai, N., Kjeldsen, H., Laughlin, G., Levine, A. M., Lin, D., Lissauer, J. J., MacQueen, P., Marcy, G., McCullough, P. R., Morton, T. D., Narita, N., Paegert, M., Palle, E., Pepe, F., Pepper, J., Quirrenbach, A., Rinehart, S. A., Sasselov, D., Sato, B., Seager, S., Sozzetti, A., Stassun, K. G., Sullivan, P., Szentgyorgyi, A., Torres, G., Udry, S., & Villaseñor, J. 2014, in *Society of Photo-Optical Instrumentation Engineers (SPIE) Conference Series*, Vol. 9143, 20

Showman, A. P., Fortney, J. J., Lewis, N. K., & Shabram, M. 2013, *ApJ*, 762, 24

Spiegel, D. S., Silverio, K., & Burrows, A. 2009, *ApJ*, 699, 1487

Waldmann, I. P., Tinetti, G., Rocchetto, M., Barton, E. J., Yurchenko, S. N., & Tennyson, J. 2015, *ApJ*, 802, 107

Wheatley, P. J., Pollacco, D. L., Queloz, D., Rauer, H., Watson, C. A., West, R. G., Chazelas, B., Loudon, T. M., Walker, S., Bannister, N., Bento, J., Burleigh, M., Cabrera, J., Eigmüller, P., Erikson, A., Genolet, L., Goad, M., Grange, A., Jordán, A., Lawrie, K., McCormac, J., & Neveu, M. 2013, in *European Physical Journal Web of Conferences*, Vol. 47, 13002

CHAPTER 2: WASP-8b: CHARACTERIZATION OF A COOL AND ECCENTRIC EXOPLANET WITH SPITZER

Patricio Cubillos^{1,2}, Joseph Harrington^{1,2}, Nikku Madhusudhan³, Kevin B. Stevenson¹, Ryan A. Hardy¹, Jasmina Blečić¹, David R. Anderson⁴, Matthew Hardin¹, and Christopher J. Campo¹

¹ *Planetary Sciences Group, Department of Physics, University of Central Florida, Orlando, FL 32816-2385*

² *Max-Planck-Institut für Astronomie, Königstuhl 17, D-69117, Heidelberg, Germany*

³ *Department of Physics and Department of Astronomy, Yale University, New Haven, CT 06511, USA*

⁴ *Astrophysics Group, Keele University, Staffordshire ST5 5BG, UK*

Received 6 July 2012.

Accepted 4 March 2013.

Published in *The Astrophysical Journal* 12 April 2013.

Publication reference:

Cubillos, P., Harrington, J., Madhusudhan, N., Stevenson, K., Hardy, R., Blečić, J., Anderson, D., Hardin, M., & Campo, C. 2013, *ApJ*, 768, 42
<http://arxiv.org/abs/1303.5468>

©AAS. Reproduced with permission

2.1 Abstract

WASP-8b has 2.18 times Jupiter’s mass and is on an eccentric ($e = 0.31$) 8.16-day orbit. With a time-averaged equilibrium temperature of 948 K, it is one of the least-irradiated hot Jupiters observed with the *Spitzer Space Telescope*. We have analyzed six photometric light curves of WASP-8b during secondary eclipse observed in the 3.6, 4.5, and 8.0 μm Infrared Array Camera bands. The eclipse depths are $0.113 \pm 0.018\%$, $0.069 \pm 0.007\%$, and $0.093 \pm 0.023\%$, respectively, giving respective brightness temperatures of 1552, 1131, and 938 K. We characterized the atmospheric thermal profile and composition of the planet using a line-by-line radiative transfer code and a MCMC sampler. The data indicated no thermal inversion, independently of any assumption about chemical composition. We noted an anomalously high 3.6- μm brightness temperature (1552 K); by modeling the eccentricity-caused thermal variation, we found that this temperature is plausible for radiative time scales less than $\sim 10^2$ hours. However, as no model spectra fit all three data points well, the temperature discrepancy remains as an open question.

2.2 Introduction

When transiting exoplanets pass behind their host stars (a secondary eclipse), the observed flux drop provides a direct measurement of the planet’s thermal emission and reflected light. Today, secondary-eclipse observations exist for nearly 30 exoplanets. The *Spitzer Space Telescope* (Werner et al. 2004) made most of these observations, capturing broadband photometric light curves in six near- and mid-infrared bands (3 – 24 μm). Each band probes a specific altitude range in a planet’s atmosphere. With Bayesian fitting of model spectra, one can quantitatively

constrain the atmospheric chemical composition and thermal profile of the planet's photosphere (Madhusudhan & Seager 2010). WASP-8b, with a time-averaged equilibrium temperature of 948 ± 22 K (T_{eq} , temperature at which blackbody emission balances absorbed energy, assuming zero albedo and efficient heat redistribution), is one of the coolest Jupiter-sized planets yet observed in eclipse, and thus serves as an end member to the set of measured hot-Jupiter atmospheres.

To classify the hot-Jupiter population, Fortney et al. (2008) proposed a separation between moderately and strongly irradiated planets. The higher atmospheric temperatures of the more strongly irradiated planets allow the presence of highly opaque molecules (like TiO and VO) at high altitudes. These strong absorbers produce hot stratospheres (thermal inversion layers). In contrast, for the moderately irradiated hot Jupiters, these absorbers condense and rain out to altitudes below the photosphere, thus presenting no thermal inversions.

In general, the observations agree with this hypothesis, but exceptions indicate that the picture is not yet completely understood. For example, secondary-eclipse observations of the highly irradiated WASP-12b (Madhusudhan et al. 2011, Crossfield et al. 2012), WASP-14b (Blecic et al. 2012), and TrES-3 (Fressin et al. 2010) do not show evidence of thermal inversions. Conversely, XO-1 has an inversion layer even though it receives a much lower stellar irradiation (Machalek et al. 2008). Photochemistry provides one explanation. The non-equilibrium atmospheric chemistry models of Zahnle et al. (2009) suggested that heating from sulfur compounds in the upper atmospheres of hot Jupiters could explain these inversions. Alternatively, Knutson et al. (2010) suggest that strong UV radiation from active stars destroys the high-altitude absorbers.

The Wide-Angle Search for Planets (WASP) Consortium discovered WASP-8b in 2008 (Queloz et al. 2010). The planet orbits the brighter component (WASP-8A) of a binary stellar system. The angular separation ($4.83''$) with the secondary (WASP-8B) sets a minimum separation of 440 AU between the stars. WASP-8A is a G6 star, with effective temperature $T_{\text{eff}} = 5600$ K. Color and photometric analyses indicate that WASP-8B is a colder M star (Queloz et al. 2010). WASP-8b is a 2.18 Jupiter-mass (M_{Jup}) planet with 1.08 times Jupiter’s radius (R_{Jup}) in a retrograde 8.16 day orbit. Its large eccentricity ($e = 0.31$) should make the planet’s dayside temperature vary by hundreds of degrees along the orbit, possibly forcing an unusual climate.

The age of the host star (4 Gyr) is shorter than the planet’s orbital circularization time (~ 30 Gyr, see, e.g., Goldreich & Soter 1966, Bodenheimer et al. 2001); accordingly, WASP-8b has one of the most eccentric orbits among the ~ 10 -day-period exoplanets (Pont et al. 2011). The Kozai mechanism (Wu & Murray 2003) may explain the combination of high eccentricity and retrograde orbit orientation. The radial-velocity drift and the large eccentricity may also indicate a second planetary companion (Queloz et al. 2010).

We obtained six secondary-eclipse light curves of WASP-8b from four visits of the *Spitzer Space Telescope*, observing in the 3.6, 4.5, and 8.0 μm bands of the Infrared Array Camera (IRAC, Fazio et al. 2004). The eclipse depths determine the planet’s dayside infrared emission. Our Markov-chain Monte Carlo-driven radiative-transfer code constrained the molecular abundances and temperature profile of WASP-8b’s dayside atmosphere, testing for the expected absence of a thermal inversion and estimating the energy redistribution over its surface. We constrained the orbit of WASP-8b by determining the eclipse epochs and durations. We also modeled the thermal variations along the orbit of the planet to explore the effects of the eccentricity.

Section 2.3 presents the *Spitzer* observations of the WASP-8 system. Section 2.4 describes the photometric and modeling analysis of our secondary eclipse observations. Section 2.5 gives the orbital dynamical analysis. Section 2.6 presents our constraints on WASP-8b’s atmospheric composition derived from the photometry. Section 2.7 discusses the effects of eccentricity on the orbital thermal variation of WASP-8b. Finally, Section 2.8 states our conclusions.

2.3 Observations

The *Spitzer Space Telescope* visited WASP-8 four times. From two consecutive eclipse observations, we obtained simultaneous light curves at 4.5 and 8.0 μm . Later, from two more consecutive eclipse observations during the *Warm Spitzer* mission, we obtained one light curve at 3.6 μm and one at 4.5 μm (see Table 2.1). The *Spitzer* pipeline (version 18.18.0) processed the raw data, producing Basic Calibrated Data (BCD).

Table 2.1: Observation Information

Label ^a	Wavel. (μm)	Observation date	Duration (minutes)	Exp. time (seconds)	Cadence (seconds)
wa008bs22	4.5	2008 Dec 13	226	1.20	2.0
wa008bs42	8.0	2008 Dec 13	226	10.40	12.0
wa008bs21	4.5	2008 Dec 21	226	1.20	2.0
wa008bs41	8.0	2008 Dec 21	226	10.40	12.0
wa008bs11	3.6	2010 Jul 23	458	0.36	0.4
wa008bs23	4.5	2010 Jul 31	458	0.36	0.4

Note. ^a *wa008b* designates the planet, *s* specifies secondary eclipse, and the two numbers indicate the wavelength channel and observation serial number (we analyzed the 2008 December 21 data before the 2008 December 13 data and inadvertently inverted the serial numbers).

During the initial minutes of our observations, the telescope pointing drifted ~ 0.25 pixels before stabilizing. Throughout the observations, the pointing also jittered from frame to frame (~ 0.01 pixel) and oscillated in an hour-long periodic movement (~ 0.1 pixel amplitude).

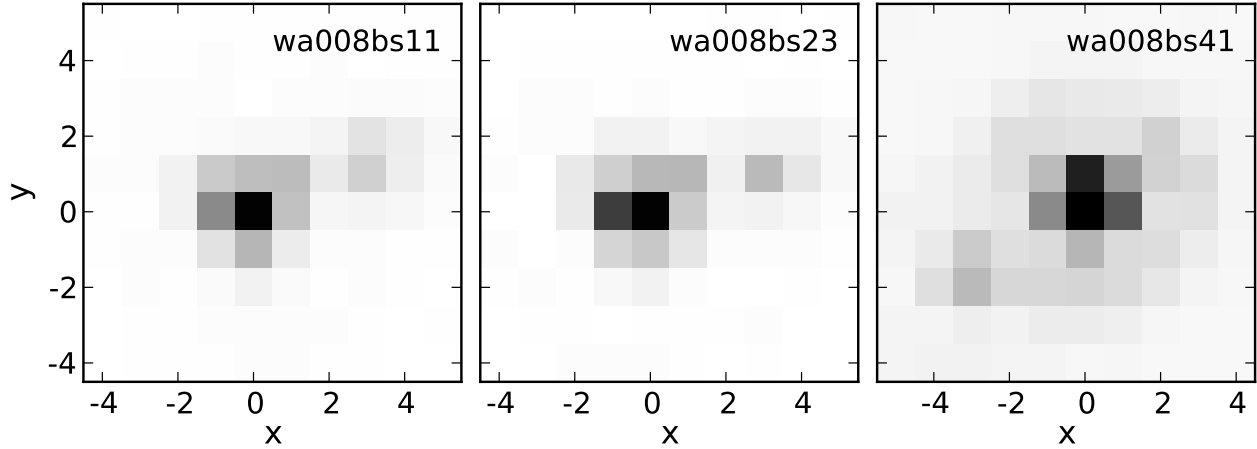


Figure 2.1: *Spitzer* images of WASP-8 at 3.6, 4.5, and 8.0 μm , respectively. The brighter star, WASP-8A, is at the origin. The dimmer WASP-8B signal overlapped that of WASP-8A.

The separation between the centers of WASP-8A and WASP-8B in the IRAC detectors is only 3.7 pixels. Consequently, the signal from the stars overlapped, demanding special care during the data analysis (see Figure 2.1). Table 2.2 shows the average and standard deviation of the flux ratio, separation, and position angle (PA) of the secondary star with respect to WASP-8A (derived from our centering routine, see Section 2.4.2). Our PA values agree with those of Queloz et al. (2010), but our separation values are consistently lower than theirs ($4.83 \pm 0.01''$).

Table 2.2: WASP-8 System

Event	Flux Ratio		Separation (pix)		Separation ($''$)		Position Angle (deg)	
	average	stddev	average	stddev	average	stddev	average	stddev
wa008bs11	0.1420	0.0030	3.760	0.013	4.610	0.016	171.32	0.28
wa008bs21	0.1512	0.0017	3.734	0.007	4.541	0.009	171.00	0.15
wa008bs22	0.1600	0.0022	3.737	0.009	4.544	0.011	170.75	0.16
wa008bs23	0.1648	0.0039	3.726	0.017	4.497	0.020	170.78	0.29
wa008bs41	0.1718	0.0020	3.690	0.009	4.513	0.011	170.84	0.17
wa008bs42	0.1794	0.0023	3.686	0.010	4.506	0.012	170.96	0.16

2.4 Data Analysis

Our Photometry for Orbits, Eclipses, and Transits (POET) pipeline produces light curves from BCD images. Briefly, POET creates a bad pixel mask for each image, finds the center position of the target, executes interpolated aperture photometry, and fits a light curve model that includes physical and systematic parameters.

2.4.1 POET: Initial Reduction

POET created bad pixel masks by discarding the flagged pixels from the Spitzer BCD masks. Then, it discarded outlier pixels with a sigma-rejection method. At each pixel position and in sets of 64 consecutive images, POET calculated the median and standard deviation of the unmasked pixels. Pixels diverging more than four times the standard deviation from the median were masked. We iterated this process twice.

We obtained the Julian Date of each frame from the `UTCS_OBS` and `FRAMTIME` entries of the files' headers. We calculated the Barycentric Julian Date (BJD) by correcting the projected light-travel time from the telescope to the Solar System's barycenter using the Jet Propulsion Laboratory (JPL) Horizons system. We report the times in both Coordinated Universal Time (UTC) and the Barycentric Dynamical Time (TDB); the latter is unaffected by leap seconds (Eastman et al. 2010).

2.4.2 Centering

POET provides three routines to determine the center of the point-spread function (PSF) in each image: center of light, 2D-Gaussian fitting, and least asymmetry (Stevenson et al. 2010, Supplementary Information). The proximity of WASP-8B confuses these methods, so we added a double-PSF fit that shifts supersampled PSFs to the target and secondary, bins them down, and scales their amplitudes, as in Crossfield et al. (2010). For each *Spitzer* band we used Tiny Tim¹ (version 2.0) to create a stellar PSF model with a 5600 K blackbody spectrum at $100\times$ finer resolution than our images. The double-PSF routine has seven free parameters: the position of each star (x_A, y_A, x_B, y_B) , the integrated stellar fluxes (F_A, F_B) , and the background sky flux (f_{sky}) .

To avoid interpolation when binning down, the PSF shifts are quantized at the model’s resolution, such that image and model pixel boundaries coincide. This quantization sets the position precision to 0.01 pixels. It also excludes the position parameters from χ^2 minimizers that assume a continuous function, such as Levenberg-Marquardt. So, we fit F_A , F_B , and f_{sky} for a given position set $\mathbf{x} = \{x_A, y_A, x_B, y_B\}$.

To avoid the computational challenge of performing a χ^2 minimization for each \mathbf{x} in a 4D space at 0.01 pixel resolution, we explored only specific coordinate positions. Starting at an initial guess position, and with an initial jump step of 100 positions (1 image pixel), we calculated χ^2 at that position and the 80 ($= 3^4 - 1$) adjacent positions that are one jump step away along all combinations of coordinate directions. We either moved to the lowest χ^2 or, if already there, shrank the step by half. We repeated the procedure until the step was zero.

¹<http://irsa.ipac.caltech.edu/data/SPITZER/docs/dataanaly-sistools/tools/contributed/general/stinytim/>

2.4.3 Photometry

Circular aperture photometry is unsuitable for this system, since any flux from the secondary star (WASP-8B) contained in the aperture dilutes the eclipse depth of WASP-8b. Small pointing jitter would also increase the light-curve dispersion for any aperture that included much WASP-8B flux. Apertures that are too large or small both produce noisier light curves. Thus, we modified the POET interpolated aperture photometry (Harrington et al. 2007, Supplementary Information) to remove the secondary star two different ways. In both methods, we subtracted the median sky level prior to the stellar flux calculation. The sky annulus included values 7 – 15 pixels from the target.

In our first method (B-Subtract), we subtracted the fitted, binned PSF model of WASP-8B from each image. Then, we performed interpolated aperture photometry centered on the target (A aperture). In the second method (B-Mask), we discarded the pixels within a circular aperture centered at the position of the secondary before performing aperture photometry. The mask’s aperture must encompass most of the contribution from WASP-8B, but not from the target. Therefore, we tested mask apertures with 1.6, 1.8, and 2.0 pixel radii. For each photometry method we tested a broad range of A-aperture radii in 0.25 pixel intervals.

The B-Mask method has less residual dispersion when the mask is located at a fixed vector separation from WASP-8A (using the median of all the measured separations in an event), than when its position is determined for each individual frame. This can be explained by the dimmer signal of WASP-8B, which lowers the accuracy of its position estimation. So, within each dataset using B-Mask, we used the median vector separation of the two objects. For the B-subtract method, the SDNR and eclipse-depths differences are marginal.

2.4.4 Light-curve Modeling

The eclipse depths of WASP-8b are on the order of 0.1% of the system’s flux, well below *Spitzer’s* photometric stability criteria (Fazio et al. 2004). Thus, the eclipse light-curve modeling requires a thorough characterization of the detector systematics. Systematic effects have been largely observed and documented; they can have both temporal and spatial components, and vary in strength and behavior for each dataset.

The main systematic at 3.6 and 4.5 μm is intrapixel sensitivity variation, $M(x, y)$, where the measured flux depends on the precise position of the target on the array (Stevenson et al. 2012, Charbonneau et al. 2005). In addition, the detectors show a time-dependent sensitivity variation called the *ramp* effect, $R(t)$, suspected to be caused by charge trapping (Agol et al. 2010) at 8.0 μm , but there are also reports of a ramp in the 3.6 and 4.5 μm bands (e.g., Campo et al. 2011, Nymeyer et al. 2011, Knutson et al. 2011, Deming et al. 2011, Blecic et al. 2012, Stevenson et al. 2010, 2012). The eclipse and both systematic variations entangle to produce the observed light curve. To account for their contributions, we modeled the light curves as

$$F(x, y, t) = F_s M(x, y) R(t) E(t), \quad (2.1)$$

where F_s is the out-of-eclipse system flux. We used the eclipse model, $E(t)$, from Mandel & Agol (2002). The eclipse is parametrized by the eclipse depth, the mid-point phase, the duration, and the ingress and egress times. For the ingress/egress times we adopted a value of 18.8 min, derived from the orbital parameters of the planet. We used this value in all of our eclipse-model fits.

The strength and behavior of the ramp variations are specific to each dataset. Many formulae have been applied in the literature (e.g., Deming et al. 2007, Harrington et al. 2007, Knutson et al. 2011, Stevenson et al. 2012). The models are formed with combinations of exponential, logarithmic, and polynomial functions. We tested dozens of equations; the best were:

$$\text{risingexp} : R(t) = 1 - e^{-r_0(t-t_0)} \quad (2.2)$$

$$\text{logramp}_q : R(t) = 1 + r_q[\ln(t - t_0)]^q \quad (2.3)$$

$$\text{linramp} : R(t) = 1 + r_1(t - t_c) \quad (2.4)$$

$$\text{quadramp}_1 : R(t) = 1 + r_1(t - t_c) + r_2(t - t_c)^2 \quad (2.5)$$

$$\text{quadramp}_2 : R(t) = 1 + r_2(t - t_c)^2 \quad (2.6)$$

$$\text{loglinear} : R(t) = 1 + r_1(t - t_c) + r_4 \ln(t - t_0) \quad (2.7)$$

where t_c is a constant value at the approximated mid-point phase of the eclipse ($t_c = 0.515$ for this planet). Slight changes in t_c do not significantly affect the fitted eclipse parameters.

We used our Bi-Linearly Interpolated Subpixel Sensitivity (BLISS) mapping technique (Stevenson et al. 2012) to calculate $M(x, y)$. The BLISS method has been found to return a better result than a polynomial fit (Stevenson et al. 2012, Blečić et al. 2012).

To determine the best-fitting parameters of our model (Eq. 2.1), we used a χ^2 minimizer with the Levenberg-Marquardt algorithm. We used Bayesian posterior sampling via a Markov-chain Monte Carlo (MCMC) algorithm to explore the phase space and estimate the uncertainties of the free parameters of the light-curve models. Our code implements the Metropolis random walk, which proposes parameter sets from a multivariate normal distribution centered at the current position in

the chain, computes χ^2 , and accepts (or rejects) the new set with greater probability for a lower (higher) χ^2 . By generating millions of parameters sets, the algorithm samples the posterior distribution of the model parameters. As a necessary condition for chain convergence, we require the Gelman-Rubin statistic (Gelman & Rubin 1992) to be within 1% of unity for each free parameter between four MCMC chains.

The photometry routine uses the BCD uncertainty images to estimate the uncertainties of the light-curve data points, σ_i . However, since the *Spitzer* pipeline in general overestimates these uncertainties (it is designed for absolute photometry), we multiply by a constant factor ($\sigma_i \rightarrow f \cdot \sigma_i$), such that the reduced $\chi^2 = 1$ in the light-curve fit. This is equivalent to estimating a single σ from the scatter of model residuals. Both methods account for red noise, but ours retains the (usually small) σ_i variations due to aberrant frames.

To determine the best raw light curve (i.e., by selection of photometry method and aperture radius), we calculated the standard deviation of the normalized residuals (SDNR) of the light curve fit (Stevenson et al. 2012, Campo et al. 2011). Poor fits or data with high dispersion increase SDNR; the optimum data set minimizes the SDNR value. Once we chose the best light curve, we compared the different ramp models according to the Bayesian Information Criterion (Liddle 2007),

$$\text{BIC} = \chi^2 + k \ln N, \quad (2.8)$$

where k is the number of free parameters and N the number of data points. The best model minimizes the BIC. The probability ratio favoring one model over a second one is $\exp(-\Delta\text{BIC}/2)$.

2.4.4.1 wa008bs11 Analysis

This observation started 2.9 hours before the eclipse’s first contact. The telescope observed the target in sub-array mode, allowing a high cadence (Table 2.1). We discarded the initial 15 minutes of observation while the telescope pointing settled. Our data present both intrapixel and weak ramp systematics.

Table 2.3: wa008bs11 Ramp Model Fits

$R(t)$	SDNR	ΔBIC	Ecl. Depth (%)
quadramp ₁	0.0061141	0.00	0.119
risingexp	0.0061148	1.73	0.106
logramp ₁	0.0061153	2.96	0.096
linramp	0.0061201	6.34	0.063
loglinear	0.0061141	11.10	0.119

The 2.25 pixel A aperture with B-subtract photometry minimized SDNR. Table 2.3 shows the five best-fitting models to the best wa008bs11 light curve. ΔBIC is with respect to the lowest BIC value. The quadramp₁ model is 2.4 times more probable than, and consistent with, the second-best model. The linear (11σ) and quadratic (4σ) terms of the quadramp₁ model (see Table 2.9) confirm the need for a ramp model. As a general remark, we noted that all the logramp_q models produce similar BIC and eclipse parameter values; therefore, we will refer only to the logramp₁ model in the future. Models with more free parameters do not improve BIC. Following Stevenson et al. (2012), we vary the bin size and the minimum number of data points per bin (mnp) of the BLISS map to minimize the dispersion of the residuals. We required at least 4 points per bin for any dataset. The PSF-fitting position precision of 0.01 pixels sets our lower limit for the binsize. For wa008bs11, $mnp = 5$ and a bin size of 0.015 pixels optimized the fit.

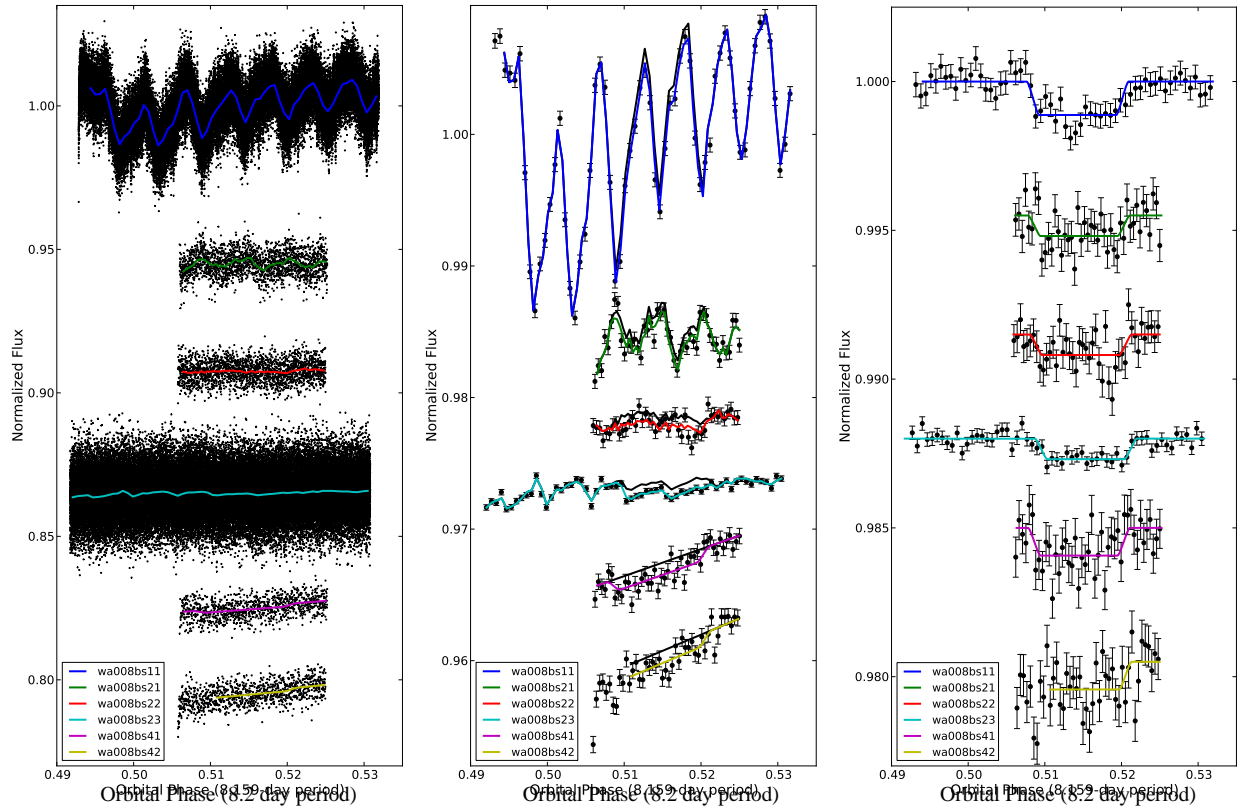


Figure 2.2: Raw (left), binned (center) and systematics-corrected (right) secondary-eclipse light curves of WASP-8b at 3.6, 4.5, and 8.0 μm . The system flux is normalized to unity and the points are shifted vertically for clarity. The colored curves are the best-fit models (see legend). The black curves are the best-fit models excluding the eclipse component. The error bars in the center and right panels are the 1σ uncertainties.

Figure 2.2 shows the raw, binned and systematics-corrected wa008bs11 light curves with their best-fitting model. We considered the correlated noise in the residuals as well (Pont et al. 2006). Figure 2.3 shows the root-mean-square (RMS) of the residuals vs. bin size. The wa008bs11 RMS curve deviates above the expected RMS for pure Gaussian noise. Following Winn et al. (2008), to account for the correlated noise, we weighted the light curve uncertainties by the factor β (the fractional RMS excess above the pure Gaussian RMS at the bin size corresponding to the eclipse duration). For wa008bs11 we found $\beta = 2.4$. We inspected all the pairwise correlation plots and histograms and found only unimodal Gaussian distributions.

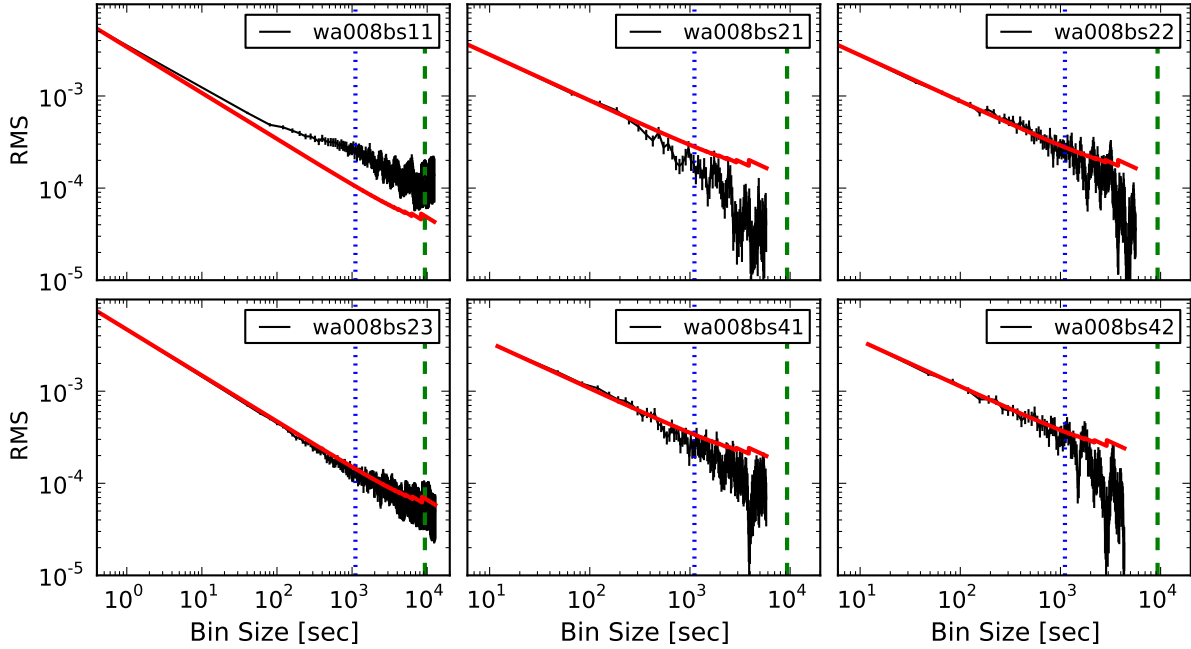


Figure 2.3: RMS of the fit residuals (black curves with 1σ uncertainties) vs. bin size of the WASP-8b light curves. The red curves are the expected RMS for Gaussian noise (extrapolated unbinned RMS scaling by the inverse square root of the bin size). The blue dotted and green dashed vertical lines mark the bin size corresponding to the eclipse ingress and duration time, respectively. wa008bs11’s excess above the red line indicate correlated noise at bin sizes larger than the ingress time.

Alternatively, the residual-permutation (also known as *prayer bead*) algorithm is sometimes used to assess correlated noise in a fit. In this method, we cyclically shift the residuals from the best model by one frame, add them back to that model, and re-fit, repeating until we shift the residuals back to their original positions. This generates a distribution of values for each parameter, from which we estimate the parameter uncertainties. The eclipse-depth uncertainty is 0.021%, similar to the value found with the Winn et al. (2008) method (see Table 2.9). However, we are cautious. Although prayer bead has been broadly used for the analysis of exoplanet lightcurve and radial-velocity fits (e.g., Southworth 2008, Bouchy et al. 2005, Pont et al. 2005, Gillon et al. 2007, Knutson et al. 2008, Cowan et al. 2012), we have found no detailed description of its statistical properties in the literature.

2.4.4.2 wa008bs23 Analysis

With the same observing setup as wa008bs11, this observation started 3.3 hours prior to the eclipse’s first contact. This dataset also presented both intrapixel and ramp variations. Note that the intrapixel systematic is weaker than at 3.6 μm , attributed to the smaller degree of undersampling at larger wavelengths by Charbonneau et al. (2005) and Morales-Calderón et al. (2006). Even though the pointing stabilized only after the initial 20 minutes, the light curve did not deviate significantly; therefore, we included all data points in the analysis. We noted two sudden pointing and PA deviations near phase 0.519. After each incident, the telescope resumed its position within ~ 10 seconds (Figure 2.4). Micrometeorite impacts on the telescope can explain the abrupt deviations. Simultaneously, we measured a slight increase in the background sky flux dispersion, which returned to normality shortly after. The target flux did not show any extraordinary fluctuations during these incidents. However, the points outside the normal pointing range were eliminated by the BLISS map’s mnp criterion.

The analysis is analogous to wa008bs11. The SDNR indicated clearly that the 2.25 pixel A aperture with B-Subtract photometry produced the lowest dispersion. The best-fitting ramp model is logramp_1 , which is 21 times more probable than the rising exponential ramp (Table 2.4). The BLISS map is optimized at $mnp = 4$ and a bin size of 0.025 pixels.

Table 2.4: wa008bs23 Ramp Model Fits

$R(t)$	SDNR	ΔBIC	Ecl. Depth (%)
logramp_1	0.0073830	0.00	0.0677
risingexp	0.0073832	6.10	0.0730
quadramp_1	0.0073833	9.40	0.0777
loglinear	0.0073830	10.84	0.0685
linramp	0.0073846	12.19	0.0564

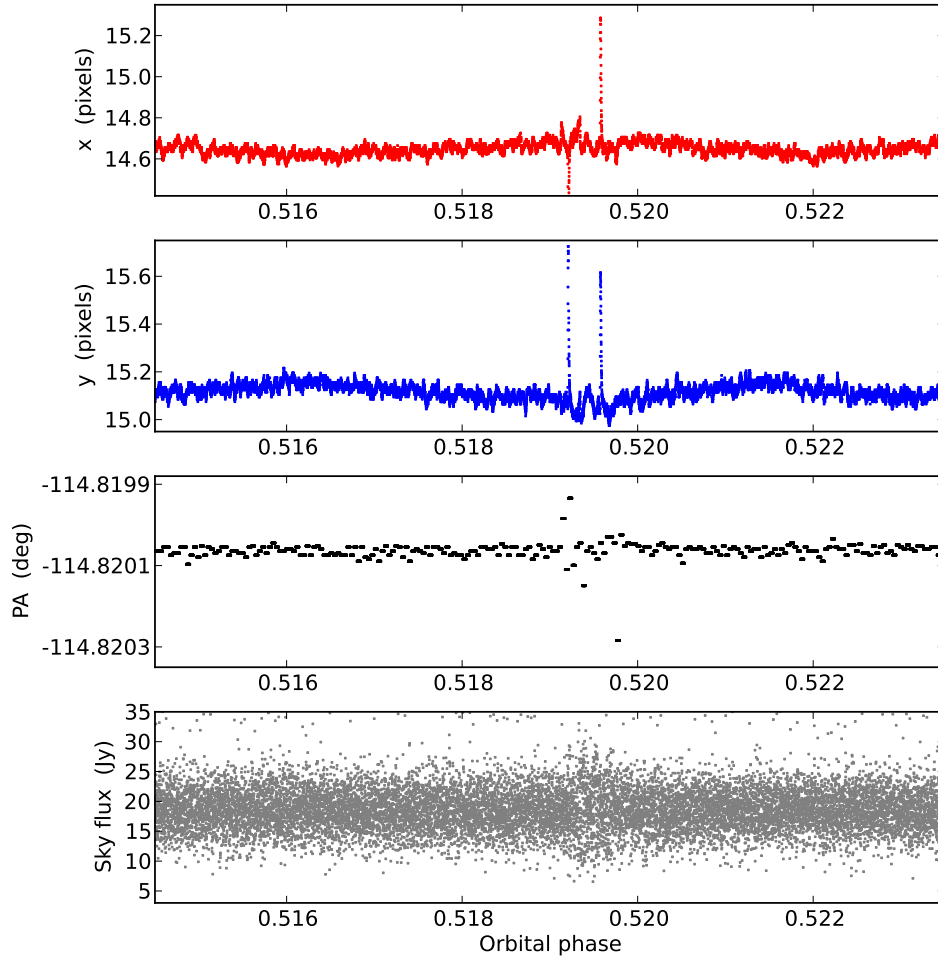


Figure 2.4: wa008bs23 target pointing, position angle and background sky flux near phase 0.519. We observed two sudden position shifts coincident with increases in the background flux. All values returned to normal almost instantly.

An initial MCMC run showed a significant linear correlation between the system flux and the r_1 parameter of the logramp, which prevented the MCMC chain from converging. We solved this problem by transforming the correlated parameters into an orthogonal set of parameters, rerunning the MCMC chain, and inverting the transformation on the resulting parameter values (Stevenson et al. 2012). Figures 2.2 and 2.3 show the wa008bs23 light curves with the best-fitting model and RMS of the residuals vs. bin size.

2.4.4.3 wa008bs21 & wa008bs41 Analysis

We simultaneously observed wa008bs21 and wa008bs41 in full-array mode. Prior to the eclipse observation, we exposed the detector (a “preflash” observation, Knutson et al. 2009) for 25 minutes to a bright HII region, with coordinates $\alpha = 20^{\text{h}} 21^{\text{m}} 39^{\text{s}}.28$ and $\delta = +37^{\circ} 31' 03.6''$, to minimize the ramp systematic variation. The secondary-eclipse observation started only 26 minutes before the first contact. The telescope pointing stabilized quickly, so fortunately we needed to remove only the initial four minutes of observation. Every 12 seconds, the detector recorded two consecutive images (two-second exposures) at $4.5 \mu\text{m}$ and one image at $8.0 \mu\text{m}$. (Table 2.1).

The SDNR analysis of wa008bs21 showed that a 3.5 pixel A aperture with 1.6 pixel B-Mask photometry minimizes the dispersion (Figure 2.5). The ramp models indicated a negligible ramp variation. Accordingly, a fit without a ramp model yielded the lowest BIC. Table 2.5 shows the four best-fitting models for the best wa008bs21 data set. The no-ramp model is 15 times more probable than the quadramp_2 model.

Table 2.5: wa008bs21 Ramp Model Fits

$R(t)$	SDNR	ΔBIC	Ecl. Depth (%)
no ramp	0.0036223	0.00	0.0718
quadramp_2	0.0036195	5.76	0.1189
linramp	0.0036223	7.56	0.0714
quadramp_1	0.0036197	13.14	0.1170

Because of the shorter out-of-eclipse observation, the system flux is less-constrained for wa008bs21 than for the wa008bs11 or wa008bs23 events. Combined with a correlation between the eclipse depth and system flux (revealed by MCMC), the lower precision of the system flux translates into a larger eclipse depth uncertainty. Nevertheless, the wa008bs21 fit parameters were consistent among the different apertures (Figure 2.6). The optimum parameters of the BLISS map are $mnp = 5$ and a bin size of 0.025 pixels.

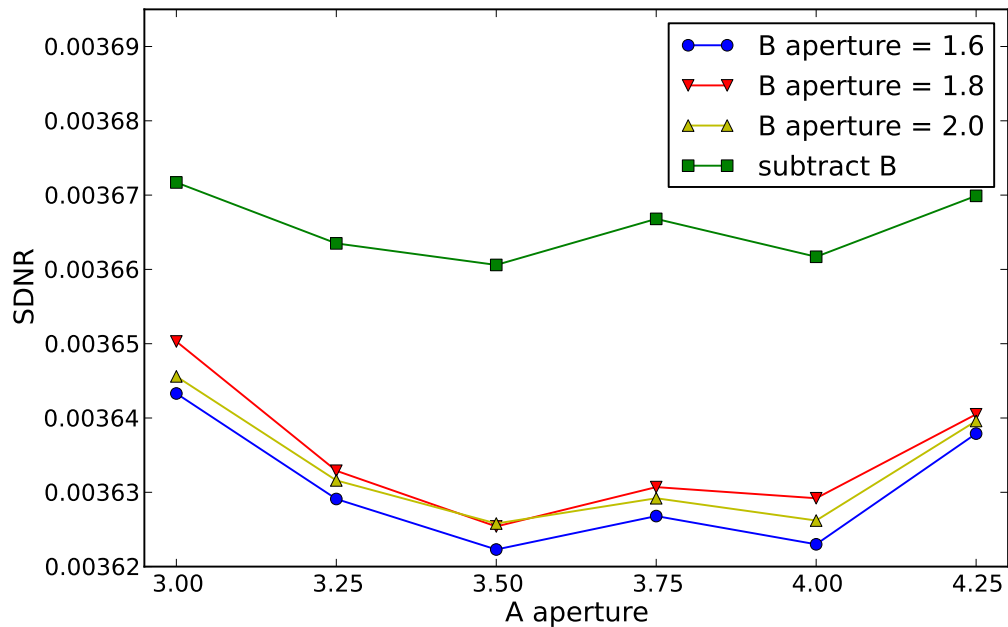


Figure 2.5: wa008bs21 standard deviation of the normalized residuals vs. aperture (in pixels). The SDNR curves use the best ramp model in Table 2.5. The legend indicates the photometry method. SDNR increases at 3.75 pixels (coincident with the stars’ separation). The eclipse parameters are consistent over the 3.0–4.25 aperture range. The optimum dataset uses 1.6 pixel B-Mask photometry with a 3.5 pixel A aperture.

The 8.0 μm detector did not present an intrapixel pattern like the 3.6 or 4.5 μm detectors. However, some of the raw light curves for different apertures and photometry methods showed large scatter and presented strong oscillations, producing implausible fit parameters. A pixelation effect (Anderson et al. 2011, Stevenson et al. 2012) might be responsible. As a consequence, we were unable to fit the eclipse parameters unambiguously for this data set alone. Normally we study the events individually to select the best aperture and photometry method, but in this case we used a joint fit with the best wa008bs21 dataset and model to help constrain the 8.0 μm eclipse curve, sharing the eclipse duration and mid-point parameters. The 3.5 pixel A aperture with 1.6 pixel B-mask photometry for wa008bs41 minimized the joint SDNR (Figure 2.7).

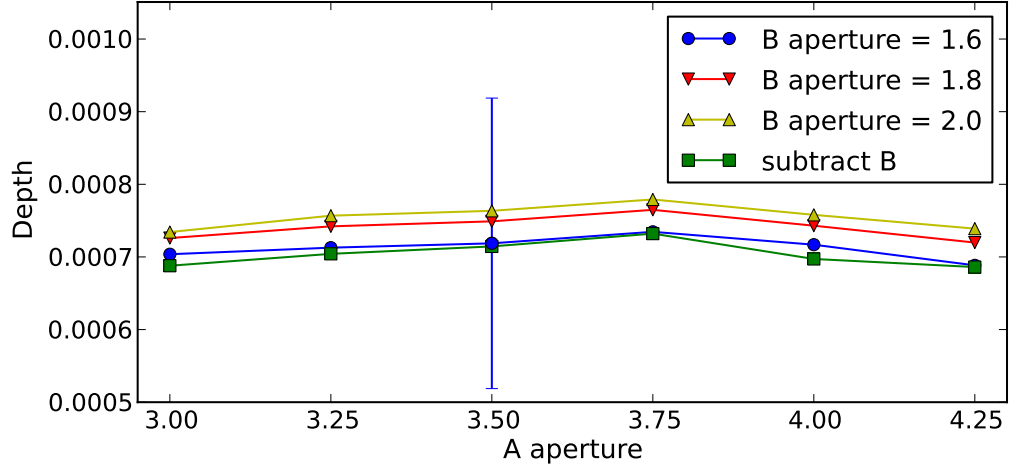


Figure 2.6: Eclipse depth vs. A aperture for wa008bs21. Each color represent a different photometry method as in Figure 2.5. The blue error bar corresponds to the $1\text{-}\sigma$ uncertainty of the best model. The eclipse duration and mid-point phase follow a similar trend.

Table 2.6 compares the four best-fitting ramp models for the best wa008bs41 light curve. A linear ramp minimizes BIC, and is 20 times more probable than the next-best model. Figures 2.2 and 2.3 show the wa008bs21 and wa008bs41 light curves with their best-fitting models and RMS of the residuals vs. bin size, respectively.

Table 2.6: wa008bs41 Ramp Model Fits

$R(t)$	SDNR 4&2	ΔBIC	Ecl. Depth (%)
linramp	0.0030766	0.00	0.0931
quadramp ₁	0.0030744	5.94	0.1308
risingexp	0.0030754	6.33	0.1150
logramp ₁	0.0030758	6.50	0.1078

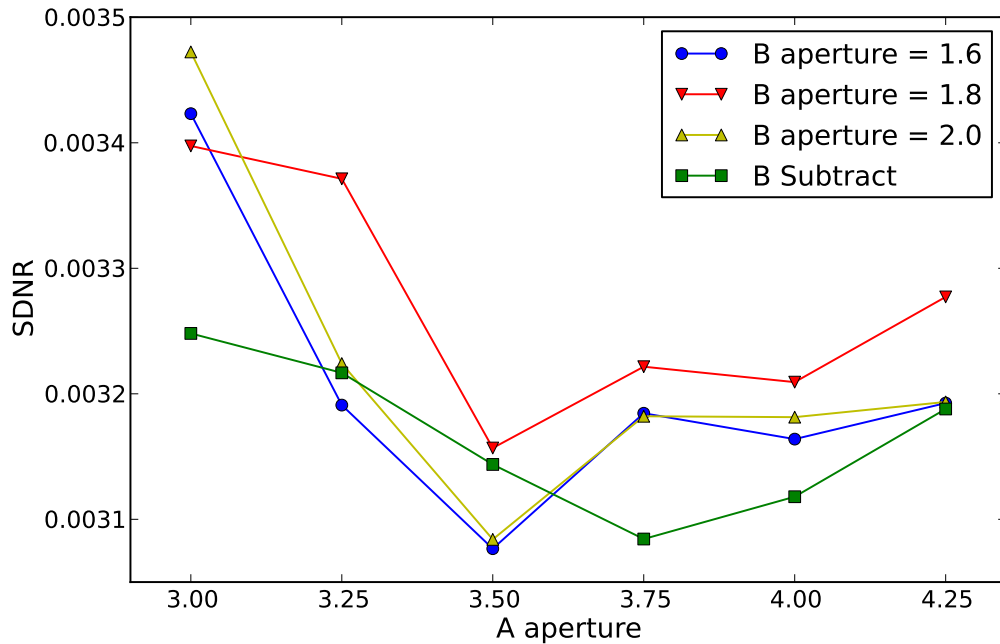


Figure 2.7: Joint wa008bs21+wa008bs41 standard deviation of the normalized residuals vs. aperture radius (in pixels) of wa008bs41, for different photometry methods. All 24 light curves use the best ramp model from Table 2.6. Light curves using 1.6 and 2.0 pixel B-Mask photometry at 3.5 pixel A aperture produce consistent eclipse parameters and outperform the best B-subtract method (with a 3.75 pixel A aperture). The best B-subtract also yields a more scattered raw light curve. Hence, the optimum dataset uses 1.6 pixel B-mask photometry with a 3.5 pixel A aperture.

2.4.4.4 wa008bs22 & wa008bs42 Analysis

The observing setup of these events was identical to wa008bs21 and wa008bs41, including the preflash observation. The pointing of this observation drifted noticeably more than in the other observations, moving more than 0.4 pixels during the initial 30 minutes and stabilizing only during the eclipse. As a consequence, the illumination level of the individual pixels changed during the beginning of the eclipse. The ramp variation, which depends on the illumination (Knutson et al. 2008), was disrupted.

The wa008bs22 event, having a negligible ramp variation, was little affected by the telescope pointing shift. The SDNR calculation for wa008bs22 indicated the 1.8 pixel B-Mask photometry with 3.75 pixel A aperture as the best dataset. A light-curve model without a ramp (Table 2.7) is 639 times more probable than the quadramp_2 model. The optimal BLISS map has $mnp = 4$ and a bin size of 0.02 pixels.

Table 2.7: wa008bs22 Ramp Model Fits

$R(t)$	SDNR	ΔBIC	Ecl. Depth (%)
no ramp	0.0025274	n 0.00	0.0814
quadramp_2	0.0025253	12.94	0.1224
logramp_1	0.0025267	14.22	0.0921
risingexp	0.0025274	15.04	0.0814

In contrast, we discarded the initial wa008bs42 light curve past the eclipse ingress due to the disrupted ramp variation. The eclipse model parameters are thus less constrained. By this point, we already had single-channel fits for the rest of the data, so we tuned the wa008bs42 analysis in a joint fit with all the other events, sharing the eclipse duration and mid-time. SDNR indicates the B-subtract method with 4.00 pixel A aperture as the best dataset. Table 2.8 presents the four best-fitting models. The eclipse depth is consistent with the wa008bs41 depth.

Table 2.8: wa008bs42 Ramp Model Fits

$R(t)$	SDNR	ΔBIC	Ecl. Depth (%)
linramp	0.0032320	0.00	0.0932
quadramp_1	0.0032312	6.19	0.0892
logramp_1	0.0032321	6.67	0.0938
risingexp	0.0032330	7.08	0.0961

2.4.4.5 Final Joint-fit Analysis

From the three individual fits to the 4.5 μm observations we found eclipse depths of $0.072\% \pm 0.021\%$, $0.086\% \pm 0.022\%$, and $0.068\% \pm 0.007\%$ for wa008bs21, wa008bs22, and wa008bs23, respectively. The weighted mean of the depths is $0.0692\% \pm 0.0065\%$. With a dispersion of 0.0062% around the mean, this is not larger than the individual uncertainties, thus we found no evidence for temporal variability. This dispersion corresponds to 10% of the mean eclipse depth. The consistency permitted a joint analysis of all observations. We used the best light curves and models found in the individual fits, where all events shared the eclipse duration, the three 4.5- μm events shared their eclipse depth, the two 8.0- μm events shared their eclipse depth, the simultaneous wa008bs21 and wa008bs41 events shared their eclipse mid-point phases, and the wa008bs22 and the wa008bs42 events shared their eclipse mid-point phases. Table 2.9 shows the light-curve modeling setup and results. We used these joint-fit results for the orbital and atmospheric analysis. An electronic supplement contains the best light curves, including centering, photometry, and the joint fit.

2.5 Orbital Dynamics

WASP-8b's high eccentricity ($e = 0.31$) implies that its separation from WASP-8A at periapsis (0.055 AU) is about half that at apoapsis. Given the argument of periapsis ($\omega = -85.86^\circ$), the secondary eclipse nearly coincides with the periapsis. The planet, therefore, receives over twice as much flux at eclipse as it would if the orbit were circular, explaining in part our high brightness temperature (see Table 2.9).

Table 2.9: Best-fit Eclipse Light-curve Parameters

Parameter	wa008bs11	wa008bs21	wa008bs22	wa008bs23	wa008bs41	wa008bs42
Array Position (\bar{x} , pix)	14.74	20.76	20.39	14.65	19.11	18.72
Array Position (\bar{y} , pix)	15.07	233.30	233.30	15.12	230.27	230.20
Position Consistency ^a (δ_x , pix)	0.0072	0.0223	0.0220	0.0097	0.0273	0.0254
Position Consistency ^a (δ_y , pix)	0.0118	0.0228	0.0236	0.0101	0.0272	0.0274
A Aperture Size (pix)	2.25	3.5	3.75	2.25	3.5	4.0
WASP-8B photometric Correction	subtract	1.6 mask	1.8 mask	subtract	1.6 mask	subtract
System Flux F_s (μ Jy)	144555.0(21.0)	91369.9(8.5)	90850.3(8.5)	87473.0(21.0)	32892.5(6.6)	34949.8(8.9)
Eclipse Depth (%)	0.113(18)	0.0692(68)	0.0692(68)	0.0692(68)	0.093(23)	0.093(23)
Brightness Temperature (K)	1552(85)	1131(35)	1131(35)	1131(35)	938(99)	938(99)
Eclipse Mid-point (orbits)	0.51428(34)	0.51446(37)	0.51468(41)	0.51536(28)	0.51446(37)	0.51468(41)
Eclipse Mid-point (MJD _{UTC}) ^b	5401.4981(28)	4822.2301(31)	4814.0732(33)	5409.6656(23)	4822.2301(31)	4814.0732(33)
Eclipse Mid-point (MJD _{TDB}) ^b	5401.4989(28)	4822.2309(31)	4814.0739(33)	5409.6663(23)	4822.2309(31)	4814.0739(33)
Eclipse Duration (t_{4-1} , hrs)	2.600(78)	2.600(78)	2.600(78)	2.600(78)	2.600(78)	2.600(78)
Ingress/Egress Time (t_{2-1} , hrs)	0.314	0.314	0.314	0.314	0.314	0.314
Ramp Equation ($R(t)$)	quadrap ₁	None	None	lograp ₁	linrap	linrap
Ramp, Linear Term (r_1)	0.0707(70)	0.000504(45)	0.205(22)	0.246(37)
Ramp, Quadratic Term (r_2)	-3.17(75)
Ramp, Phase Offset (t_0)	0.4917
BLISS Map ($M(x, y)$)	Yes	Yes	Yes	Yes	No	No
Minimum Num. of Points Per Bin	5	5	4	4
Total Frames	64320	2024	2024	64320	1012	1012
Frames Used ^c	62203	1936	1879	64072	966	725
Rejected Frames (%)	3.29	4.35	7.16	0.39	4.54	28.36
Free Parameters ^d	6	4	4	5	5	5
BIC Value	80444.5	80444.5	80444.5	80444.5	80444.5	80444.5
SDNR	0.0053772	0.0036250	0.0035698	0.0073926	0.0030768	0.0032320
Uncertainty Scaling Factor	0.3075	1.0280	1.0077	1.0902	1.1187	1.1382
β correction	2.4
Photon-limited S/N (%)	37.00	94.71	96.59	89.66	76.94	71.00

Notes. The values quoted in parentheses are the 1σ uncertainties.

^a rms frame-to-frame position difference.

^b MJD = BJD - 2,450,000.

^c Frames excluded during instrument settling, for insufficient points at a BLISS knot, and for bad pixels in the photometry aperture.

^d In the individual fits. Joint fit had 19 free parameters.

Secondary-eclipse times can refine estimates of $e \cos \omega$ from radial-velocity (RV) data. The four eclipse events occurred at an average eclipse phase of 0.514695 ± 0.00018 . After subtracting a coarse light-time correction of $2a/c = 80$ s from this average phase, we calculated $e \cos \omega = 0.02290 \pm 0.00028$ (see Eq. 3 of Charbonneau et al. 2005). This is consistent with Queloz et al. (2010), and photometrically confirms the nonzero eccentricity of the planet's orbit (we fit $e \cos \omega$ below without relying on the low e approximation).

The eclipse timings were combined with 130 available RV data points and with transit data from Queloz et al. (2010) using the method described by Campo et al. (2011) and Nymeyer et al. (2011). Forty-eight in-transit RV points were removed due to the Rossiter-McLaughlin effect.

Our fit presented a moderate improvement to the orbital parameters of WASP-8b (Table 2.10), except for the period. While Queloz et al. (2010) used several transits to measure the period, we used their published mid-point epoch (a single date); hence, our period is constrained mostly by our eclipses and the RV data, and thus have a larger uncertainty. By themselves, the secondary eclipses have a period of 8.158774 ± 0.00040 days and a midpoint epoch of BJD 2455409.6629 ± 0.0017 (TDB), not significantly ($[5.9 \pm 4.3] \times 10^{-5}$ days) longer than the period found by Queloz et al. (2010). The transit and eclipse periods place a $9.8 \times 10^{-5} \text{ }^\circ \text{ day}^{-1}$ (3σ) upper limit on possible apsidal precession, nearly three orders of magnitude larger than the theoretical expectation for tidal effects (Ragozzine & Wolf 2009).

Table 2.10: Eccentric Orbital Model

Parameter	This Work	Queloz et al. (2010)
$e \sin \omega$	-0.3078 ± 0.0020	-0.3092 ± 0.0029
$e \cos \omega$	0.02219 ± 0.00046	0.023 ± 0.001
e	0.309 ± 0.002	0.310 ± 0.0029
ω ($^\circ$)	-85.00 ± 0.08	-85.73 ± 0.18
P (days)	8.158719 ± 0.000034	8.158715 ± 0.000016
T_0 (MJD _{TDB})	4679.33486 ± 0.00057	4679.33509 ± 0.00050
K (ms^{-1})	221.9 ± 0.6	222.23 ± 0.8
γ_C (ms^{-1})	$-1\,565.9 \pm 0.6$	$-1\,565.8 \pm 0.21$
γ_H (ms^{-1})	$-1\,547.4 \pm 0.4$	$-1\,548.1 \pm 0.6$
$\dot{\gamma}$ ($\text{ms}^{-1}\text{yr}^{-1}$)	58.1 ± 1.2	58.1 ± 1.3
Reduced χ^2	4.1	0.86

2.6 Atmospheric Analysis

We use our IRAC observations of thermal emission from WASP-8b to constrain the thermal structure and composition of the day-side atmosphere of the planet. The *Spitzer* bandpasses at 3.6, 4.5, and 8.0 μm contain strong spectral features due to several carbon and oxygen-based molecules that are expected in hot-Jupiter atmospheres. Methane (CH_4) has strong spectral features in the 3.6 and 8.0 μm bands, carbon monoxide (CO) and carbon dioxide (CO_2) have features at 4.5 μm , while water vapor (H_2O) has features in all three bands (Madhusudhan & Seager 2010). The spectral features of the various molecules appear as absorption troughs or emission peaks in the emergent spectrum depending on whether the temperature decreases or increases with altitude, respectively. Consequently, strong degeneracies exist between the temperature structure and molecular composition derived from a spectral dataset (e.g., Madhusudhan & Seager 2010). Nevertheless, photometric observations made with *Spitzer* have been successfully used to constrain chemical compositions and temperature structures in many exoplanetary atmospheres (e.g., Barman et al. 2005, Burrows et al. 2007, Knutson et al. 2008, Madhusudhan & Seager 2009, Stevenson et al. 2010, Madhusudhan et al. 2011).

We model the dayside emergent spectrum of WASP-8b using the atmospheric modeling and retrieval method of Madhusudhan & Seager (2009, 2010). The model computes line-by-line radiative transfer in a plane-parallel atmosphere assuming hydrostatic equilibrium, local thermodynamic equilibrium, and global energy balance. We assume a Kurucz model for the stellar spectrum (Castelli & Kurucz 2004) given the stellar parameters. The pressure-temperature (P - T) profile and molecular mixing ratios are free parameters in the model, which can be constrained from the data. The P - T profile comprises of six free parameters and the mixing ratio of each molecular species constitutes an additional free parameter. Following Madhusudhan & Seager (2009), we parametrize the mixing ratio of each species as deviations from thermochemical equilibrium as-

suming solar elemental abundances (Burrows & Sharp 1999). We include the dominant sources of opacity expected in hot Jupiter atmospheres, namely molecular absorption due to H₂O, CO, CH₄ and CO₂ (Freedman et al. 2008, Freedman, personal communication 2009), and H₂-H₂ collision induced absorption (Borysow 2002). We explore the model parameter space in a Bayesian way using an MCMC sampler (Madhusudhan & Seager 2010, 2011). Given the limited number of observations ($N_{\text{obs}}=3$), our goal is not to find a unique model fit to the data; instead, we intend to constrain the region of atmospheric parameter space that is allowed or ruled out by the data.

Our observations rule out a thermal inversion in the day-side atmosphere of WASP-8b. This is evident from the planet-star flux contrasts in the three IRAC bands at 3.6, 4.5, and 8.0 μm . In the presence of a thermal inversion, the planet-star flux contrasts in the 4.5 and 8.0 μm bands are both expected to be greater than the flux contrast in the 3.6 μm band (Burrows et al. 2008, Fortney et al. 2008, Madhusudhan & Seager 2010), due to spectral features of the dominant molecules appearing as emission peaks as opposed to absorption troughs. However, the low 4.5 and 8.0 μm flux contrasts relative to the 3.6 μm contrast requires significant absorption due to H₂O and CO across the spectrum, and hence the lack of a thermal inversion in the atmosphere. Figure 2.8 shows model spectra of WASP-8b with no thermal inversion in the temperature profile. The observed 4.5 and 8.0 μm flux contrasts are explained to a good level of fit by a model without a thermal inversion and with solar abundance composition, as shown by the green curve in Fig. 2.8. Our inference of the lack of a thermal inversion in WASP-8b is independent of any assumption about chemical composition or C/O ratio (e.g. Madhusudhan & Seager 2011). The lack of a thermal inversion in WASP-8b is not surprising, since it is amongst the cooler population of irradiated hot Jupiters, which are not expected to host inversion-causing species such as TiO or VO in their upper atmosphere (Fortney et al. 2008, Spiegel et al. 2009).

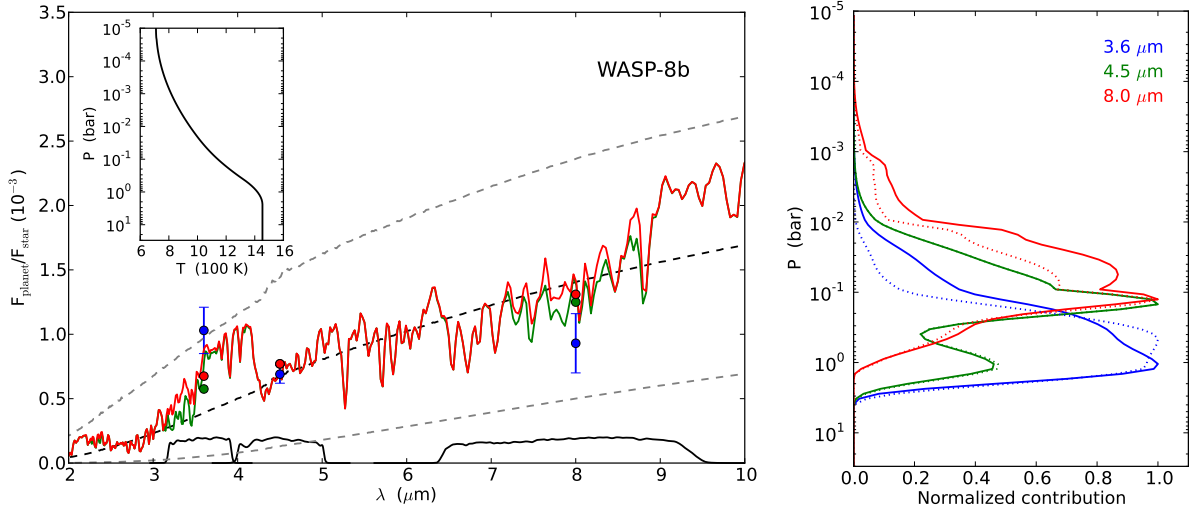


Figure 2.8: Atmospheric models of WASP-8b. **Left:** Atmospheric spectral emission of the dayside of WASP-8b. The blue circles with error bars are the measured eclipse depths, or equivalently, the planet-star flux ratios. The red and green curves show two model spectra with the same temperature profile (shown in the inset) but with different compositions. The green curve shows a model assuming chemical equilibrium with solar elemental abundances. The red curve shows a model with 10^3 times lower methane abundance compared to the green model, but the abundances of the remaining molecules are identical to those in the green model. The red and green filled circles are the corresponding model fluxes integrated over the *Spitzer* bands (bottom solid lines). The black dashed lines represent planetary blackbody spectra with $T = 710, 1100,$ and 1450 K. **Right:** Normalized contribution functions of the solar-composition model (solid lines) and the low- CH_4 -abundance model (dotted lines) in each *Spitzer* band (see legend). The effective pressures of the contribution functions are 0.63, 0.35, and 0.12 bar at 3.6, 4.5, and 8.0 μm , respectively.

Our models are unable to reproduce the high planet-star flux contrast observed in the 3.6 μm IRAC band, independent of the composition. The major sources of absorption in the 3.6 μm band are H_2O and CH_4 . In principle, decreasing the CH_4 and/or H_2O abundances can lead to a higher 3.6 μm contrast. However, as shown by the red curve in Fig. 2.8, such an increase also simultaneously increases the contrast in the 8.0 μm band, thereby worsening the fit overall. Another hindrance to

fitting the observed 3.6 μm contrast is that it requires a hotter P - T profile, with $T \gtrsim 1550$ K in the lower atmosphere, predicts much higher fluxes in the 4.5 and 8.0 μm bands than observed. On the other hand, a cooler P - T profile than shown in Fig. 2.8 would provide a better fit in the 4.5 and 8.0 μm bands, but would further worsen the fit in the 3.6 μm band. Consequently, we choose an intermediate P - T profile that provides a compromise fit to all three data points.

Although the 1D models shown in Fig. 2.8 output less energy than the instantaneous incident irradiation during the eclipse (concurrent with periastron passage), they output $\sim 20\%$ higher energy compared to the time-averaged incident irradiation received at the substellar point. Considering that a pseudo-synchronous rotation should facilitate the redistribution of energy to the night side, the high emission measured suggests that WASP-8b is quickly reradiating the incident irradiation on its day-side hemisphere, i.e. nearly zero day-night redistribution. Such a scenario would lead to a large day-night temperature contrast in the planet which can be confirmed by thermal phase curves of the planet observed using warm Spitzer (e.g., Knutson et al. 2009). The high emergent flux also implies a very low albedo, as with most hot-Jupiter planets (Cowan & Agol 2011b).

2.7 The Unexpected Brightness Temperature of WASP-8b

As seen in the previous section, the 3.6- μm brightness temperature is anomalously higher than expected. The hemisphere-averaged equilibrium temperature for instantaneous re-radiation (time-averaged around the orbit) is only 948 K; even the instantaneous equilibrium temperature at periastron, 1128 K, is far lower than this observation. Thus, we modeled the orbital thermal variation due to the eccentricity to determine if such a high temperature is possible from irradiation alone.

Following Cowan & Agol (2011a), we solved the energy balance equation in a one-layer latitude–longitude grid over the planetary surface. The change in temperature of a cell with time, dT/dt , is determined by the difference between the absorbed flux from the star and the re-emitted blackbody flux,

$$\frac{dT}{dt} = \frac{1}{c_h} \left[(1 - A) \sigma T_{\text{eff}}^4 \left(\frac{R_*}{r(t)} \right)^2 \cos \psi(t) - \sigma T^4 \right], \quad (2.9)$$

where c_h is the heat capacity per unit area; T_{eff} and R_* are the star’s effective temperature and radius, respectively; $r(t)$ is the planet-star separation; $\cos \psi(t) = \sin \lambda \max(\cos \Phi(t), 0)$ is the cosine of the angle between the vectors normal to the planet surface and the incident radiation, with λ the latitude of the cell and $\Phi(t)$ the longitude from the sub-stellar meridian; σ is the Stefan-Boltzmann constant.

Tidal interactions drive the planet’s rotational angular velocity (ω_{rot}) toward synchronization with the orbital angular velocity (ω_{orb}). Hence, if the spin synchronization timescale (e.g., Seager & Hui 2002, Goldreich & Soter 1966) is shorter than the system age, we expect $\omega_{\text{rot}} = \omega_{\text{orb}}$. In the case of WASP-8b, the timescale for tidal synchronization is on the order of 0.05 Gyr, much shorter than the age of the star. However, a planet in an eccentric orbit, where ω_{orb} changes in time, is actually expected to reach a pseudo-synchronization state (e.g., Langton & Laughlin 2008, Hut 1981), in which the planet does not exchange net angular momentum with its orbit. The planet acquires then a constant rotational angular velocity close to the orbital angular velocity at periastron ($\omega_{\text{orb,p}}$). In the literature we found different predictions for this equilibrium angular velocity, from $0.8 \omega_{\text{orb,p}}$ (Hut 1981) to $1.55 \omega_{\text{orb,p}}$ (Ivanov & Papaloizou 2007).

The tidal evolution drives the orbit of a planet toward zero obliquity in a timescale similar to the spin synchronization (Peale 1999). We thus adopted zero obliquity for our simulations. We also assumed $A = 0$, supported by the atmospheric analysis (Section 2.6). Beyond these assumptions, the parameters of interest that control Equation (2.9) are the radiative time $\tau_{\text{rad}} = c_h / \sigma T_0^3$ (where T_0 is the sub-stellar equilibrium temperature at periastron) and the rotational angular velocity of the planet ω_{rot} (which determines the sub-stellar longitude of a cell through the equation $d\Phi(t)/dt = \omega_{\text{rot}} - \omega_{\text{orb}}(t)$). With these definitions Equation (2.9) can be re-written as:

$$\frac{dT}{dt} = \frac{T_0}{\tau_{\text{rad}}} \left[\left(\frac{a(1-e)}{r(t)} \right)^2 \max(\cos \Phi(t), 0) - \left(\frac{T}{T_0} \right)^4 \right]. \quad (2.10)$$

We derived the temperature of each cell as a function of time to study its thermal evolution. Assuming that each cell emits as a blackbody, we calculated the photometric phase curve of the planet by integrating over the hemisphere observable from Earth, weighted by the viewing geometry. Our simulations were for planets nearly in pseudo-synchronous rotation ($\omega_{\text{rot}} = 0.8, 1.0$, and $1.5 \omega_{\text{orb,p}}$). We tested values of τ_{rad} between 1 and 10^3 hours.

Figure 2.9 shows simulated brightness-temperature lightcurves of WASP-8b after reaching a periodic stationary state (after a few τ_{rad}). We noted that the higher irradiation at periastron is not the only contribution to a higher temperature. For $\omega_{\text{rot}} \geq \omega_{\text{orb,p}}$, the sub-stellar angular velocity ($d\Phi/dt$) is minimum during periastron, allowing the temperature to increase due to the longer exposure to the irradiation. For $\omega_{\text{rot}} < \omega_{\text{orb,p}}$, the sub-stellar angular velocity is negative for an instant around periastron. Later, when the planet emerges from secondary eclipse the over-heated region becomes observable from Earth. As a result, the lightcurve shows a delayed maximum.

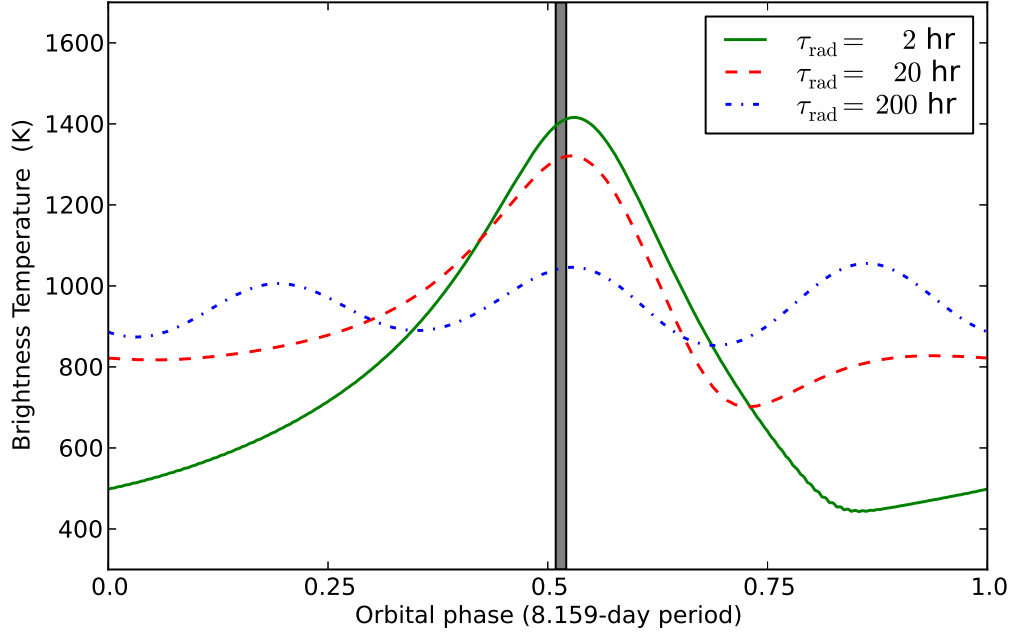


Figure 2.9: Model brightness-temperature lightcurves of WASP-8b as observed from Earth during one orbital period. Phase zero indicates the mid-transit time. The gray region indicates the secondary-eclipse interval, with periastron at phase 0.52. The models simulate super-rotating winds ($\omega_{\text{rot}} = 1.5 \omega_{\text{orb,p}}$) for different radiative times (see legend). The curves with smaller τ_{rad} show larger amplitudes. For τ_{rad} comparable to the orbit period, and since $\omega_{\text{rot}} = 1.5 \omega_{\text{orb,p}}$, opposite sides will face the star during successive periastron passages, leading to two bright spots and hence three periodic peaks per orbit.

Our models show that for large radiative timescales, the temperatures at secondary eclipse are lower than 1150 K, regardless of ω_{rot} . For radiative times shorter than $\sim 10^2$ hr, the temperatures can be as high as 1400 K, similar to the 3.6- μm measurement (Fig. 2.9, top panel). However, these models still cannot explain the observed brightness-temperature discrepancy with wavelength.

The study of eccentric hot-Jupiter atmospheric circulation by Kataria et al. (2012) hints at a resolution to this discrepancy. Their Fig. 4 (top panel) shows that, as the planet passes through periapsis, the time that the peak temperature is reached varies as a function of pressure. This is typical of their simulations (personal communication). If this differential response is significant in WASP-8b, it would introduce a discrepancy in the observations since the *Spitzer* bands sample different altitudes (see Fig. 2.9 right panel).

Another possibility is to compare the radiative and advective timescales at the altitudes sampled by each band. Evaluating equation 1 of Fortney et al. (2008) using WASP-8b's P - T profile, indicates that τ_{rad} increases with depth between 0.1 and 1.0 bar, so there should be less longitudinal temperature contrast at depth. On the other hand, models of Kataria et al. (2012) show that wind speeds decrease with depth, and thus τ_{adv} also increases with depth. If the increase of τ_{adv} with depth is sharper than that of τ_{rad} , then one would expect less-homogenized temperatures at depth (but still above the photosphere). Hence, the rise in temperature (due to the increasing incident irradiation) near periapsis could be more pronounced at 3.6 μm than at longer wavelengths, given the weighting functions of Figure 2.8.

2.8 Conclusions

Spitzer observed secondary eclipses of WASP-8b in the 3.6, 4.5, and 8.0 μm IRAC wavebands. In our joint-fit model, we estimate eclipse depths of $0.113\% \pm 0.018\%$, $0.069\% \pm 0.007\%$, and $0.093\% \pm 0.023\%$ at 3.6, 4.5, and 8.0 μm , respectively. These depths correspond to brightness temperatures of 1552, 1131, and 938 K, respectively. Although the 3.6- μm eclipse depth is unexpectedly large, most of the ramp models had consistent depths (within 1σ), while those with inconsistent depths fit the data poorly.

Considering the P – T profile of WASP-8b, KCl, ZnS, Li₂, LiF, or Na₂S clouds could form (see Fig. 2a of Lodders & Fegley 2006). In analogy to brown dwarfs, partial cloud coverage can cause photometric variability (Artigau et al. 2009); however, our three 4.5 μm observations, spanning 1.5 years, have consistent eclipse depths, suggesting no temporal variation at secondary eclipse above a hemispheric-mean level of ~ 35 K (1σ). A moderate cloud layer at altitudes higher than those probed by *Spitzer* would produce a featureless planetary spectrum at wavelengths shorter than 2 μm (Pont et al. 2008, Miller-Ricci Kempton et al. 2012) and would block some of the stellar flux, decreasing the temperatures at levels probed by *Spitzer*. Yet, the observed temperatures, which exceed the time-averaged equilibrium temperature, challenge this idea.

Given the high eccentricity, spin-orbit misalignment, and observed radial-velocity drift in the of WASP-8 system, Queloz et al. (2010) suggested the existence of an additional, unseen body in the system. Our orbital analysis is consistent with theirs. It also improves the orbital parameters and extends the baseline of sampled epochs. This constrains the long-term evolution of the orbit and aids the search for a second planet, for example through the study of timing variations (e.g., Agol et al. 2005).

The eclipse depths probe the day-side atmosphere of WASP-8b. Our results rule out the presence of a thermal inversion layer, as expected, given the irradiation level from the host star. A model with solar-abundance composition explains the 4.5 and 8.0 μm planet-star flux contrast; however, including the high 3.6 μm flux contrast requires models that output nearly 20% of the orbit-averaged incident irradiation, independent of the atmospheric composition. If the orbit were circular (and thus the irradiation steady-state), the high brightness temperatures would indicate a very low energy redistribution to the night side of the planet. For an eccentric planet, it at least indicates a short τ_{rad} (Figure 2.9).

By modeling the orbital thermal variations due to the eccentricity of the orbit, we determined that it is possible for WASP-8b to achieve temperatures as high as the 3.6 μm brightness temperature. However, the differing brightness temperatures in the other two bands remain puzzling. Neither the radiative-transfer model (Section 2.6) nor the phase-variation model (Section 2.7) embraces all the physics of the problem. The radiative transfer code is a 1D, steady-state model representing typical day-side conditions. The phase-variation model describes emission as a blackbody on a single-layer grid; it does not consider absorption or emission features from the species in the atmosphere. Clouds (e.g., Cushing et al. 2008), atmospheric dynamics (e.g., Showman et al. 2009), and photochemistry (e.g., Moses et al. 2011) are not directly considered by these models.

What we can say for certain is that the assumptions of our simple models have been violated, which is not surprising for this eccentric planet. While it may be possible to construct consistent, realistic models, model uniqueness may be elusive until more and better data are available.

Relatively few exoplanets with equilibrium temperatures below 1500 K have been observed at secondary eclipse (Cowan & Agol 2011b). The same is true for eccentric planets. The characterization of WASP-8b in this work thus addresses a particularly interesting, if challenging, region of the exoplanet phase space. Observation of other planets with similar equilibrium temperatures or eccentricities will help discover the physics that drive these unusual atmospheres.

2.9 Acknowledgments

We thank Ian Crossfield for his help with the Tiny Tim software. We thank contributors to SciPy, Matplotlib, and the Python Programming Language; the free and open-source community; the NASA Astrophysics Data System; and the JPL Solar System Dynamics group for software and services. PC is supported by the Fulbright Program for Foreign Students. NM acknowledges support from the Yale Center for Astronomy and Astrophysics through the YCAA postdoctoral Fellowship. This work is based on observations made with the *Spitzer Space Telescope*, which is operated by the Jet Propulsion Laboratory, California Institute of Technology, under a contract with NASA. Support for this work was provided by NASA through an award issued by JPL/Caltech.

2.10 List of References

- Agol, E., Cowan, N. B., Knutson, H. A., Deming, D., Steffen, J. H., Henry, G. W., & Charbonneau, D. 2010, *ApJ*, 721, 1861
- Agol, E., Steffen, J., Sari, R., & Clarkson, W. 2005, *MNRAS*, 359, 567
- Anderson, D. R., Smith, A. M. S., Lanotte, A. A., Barman, T. S., Collier Cameron, A., Campo, C. J., Gillon, M., Harrington, J., Hellier, C., Maxted, P. F. L., Queloz, D., Triaud, A. H. M. J., & Wheatley, P. J. 2011, *MNRAS*, 416, 2108
- Artigau, É., Bouchard, S., Doyon, R., & Lafrenière, D. 2009, *ApJ*, 701, 1534
- Barman, T. S., Hauschildt, P. H., & Allard, F. 2005, *ApJ*, 632, 1132
- Blecic, J., Harrington, J., Madhusudhan, N., Stevenson, K. B., Hardy, R. A., Campo, C. J., Bowman, W. C., Nymeyer, S., Cubillos, P., & Anderson, D. R. 2012, *ApJ*, submitted, (arXiv:1111.2363)

- Bodenheimer, P., Lin, D. N. C., & Mardling, R. A. 2001, *ApJ*, 548, 466
- Borysow, A. 2002, *A&A*, 390, 779
- Bouchy, F., Pont, F., Melo, C., Santos, N. C., Mayor, M., Queloz, D., & Udry, S. 2005, *A&A*, 431, 1105
- Burrows, A., Budaj, J., & Hubeny, I. 2008, *ApJ*, 678, 1436
- Burrows, A., Hubeny, I., Budaj, J., Knutson, H. A., & Charbonneau, D. 2007, *ApJ*, 668, L171
- Burrows, A. & Sharp, C. M. 1999, *ApJ*, 512, 843
- Campo, C. J., Harrington, J., Hardy, R. A., Stevenson, K. B., Nymeyer, S., Ragozzine, D., Lust, N. B., Anderson, D. R., Collier-Cameron, A., Blecic, J., Britt, C. B. T., Bowman, W. C., Wheatley, P. J., Lored, T. J., Deming, D., Hebb, L., Hellier, C., Maxted, P. F. L., Pollaco, D., & West, R. G. 2011, *ApJ*, 727, 125
- Castelli, F. & Kurucz, R. L. 2004, [arXiv:astro-ph/0405087](https://arxiv.org/abs/astro-ph/0405087)
- Charbonneau, D., Allen, L. E., Megeath, S. T., Torres, G., Alonso, R., Brown, T. M., Gilliland, R. L., Latham, D. W., Mandushev, G., O'Donovan, F. T., & Sozzetti, A. 2005, *ApJ*, 626, 523
- Cowan, N. B. & Agol, E. 2011a, *ApJ*, 726, 82
- . 2011b, *ApJ*, 729, 54
- Cowan, N. B., Machalek, P., Croll, B., Shekhtman, L. M., Burrows, A., Deming, D., Greene, T., & Hora, J. L. 2012, *ApJ*, 747, 82
- Crossfield, I. J. M., Barman, T., Hansen, B. M. S., Tanaka, I., & Kodama, T. 2012, *ApJ*, 760, 140
- Crossfield, I. J. M., Hansen, B. M. S., Harrington, J., Cho, J. Y.-K., Deming, D., Menou, K., & Seager, S. 2010, *ApJ*, 723, 1436

- Cushing, M. C., Marley, M. S., Saumon, D., Kelly, B. C., Vacca, W. D., Rayner, J. T., Freedman, R. S., Lodders, K., & Roellig, T. L. 2008, *ApJ*, 678, 1372
- Deming, D., Harrington, J., Laughlin, G., Seager, S., Navarro, S. B., Bowman, W. C., & Horning, K. 2007, *ApJ*, 667, L199
- Deming, D., Knutson, H., Agol, E., Desert, J.-M., Burrows, A., Fortney, J. J., Charbonneau, D., Cowan, N. B., Laughlin, G., Langton, J., Showman, A. P., & Lewis, N. K. 2011, *ApJ*, 726, 95
- Eastman, J., Siverd, R., & Gaudi, B. S. 2010, *PASP*, 122, 935
- Fazio, G. G., Hora, J. L., Allen, L. E., Ashby, M. L. N., Barmby, P., Deutsch, L. K., Huang, J.-S., Kleiner, S., Marengo, M., Megeath, S. T., Melnick, G. J., Pahre, M. A., Patten, B. M., Polizotti, J., Smith, H. A., Taylor, R. S., Wang, Z., Willner, S. P., Hoffmann, W. F., Pipher, J. L., Forrest, W. J., McMurty, C. W., McCreight, C. R., McKelvey, M. E., McMurray, R. E., Koch, D. G., Moseley, S. H., Arendt, R. G., Mentzell, J. E., Marx, C. T., Losch, P., Mayman, P., Eichhorn, W., Krebs, D., Jhabvala, M., Gezari, D. Y., Fixsen, D. J., Flores, J., Shakoorzadeh, K., Jungo, R., Hakun, C., Workman, L., Karpati, G., Kichak, R., Whitley, R., Mann, S., Tollestrup, E. V., Eisenhardt, P., Stern, D., Gorjian, V., Bhattacharya, B., Carey, S., Nelson, B. O., Glaccum, W. J., Lacy, M., Lowrance, P. J., Laine, S., Reach, W. T., Stauffer, J. A., Surace, J. A., Wilson, G., Wright, E. L., Hoffman, A., Domingo, G., & Cohen, M. 2004, *ApJS*, 154, 10
- Fortney, J. J., Lodders, K., Marley, M. S., & Freedman, R. S. 2008, *ApJ*, 678, 1419
- Freedman, R. S., Marley, M. S., & Lodders, K. 2008, *ApJS*, 174, 504
- Fressin, F., Knutson, H. A., Charbonneau, D., O'Donovan, F. T., Burrows, A., Deming, D., Mandushev, G., & Spiegel, D. 2010, *ApJ*, 711, 374
- Gelman, A. & Rubin, D. B. 1992, *Statistical Science*, 7, 457

- Gillon, M., Demory, B.-O., Barman, T., Bonfils, X., Mazeh, T., Pont, F., Udry, S., Mayor, M., & Queloz, D. 2007, *A&A*, 471, L51
- Goldreich, P. & Soter, S. 1966, *icarus*, 5, 375
- Harrington, J., Luszcz, S. H., Seager, S., Deming, D., & Richardson, L. J. 2007, *Nature*, 447, 691
- Hut, P. 1981, *A&A*, 99, 126
- Ivanov, P. B. & Papaloizou, J. C. B. 2007, *MNRAS*, 376, 682
- Kataria, T., Showman, A. P., Lewis, N. K., Fortney, J. J., Marley, M. S., & Freedman, R. S. 2012, ArXiv e-prints
- Knutson, H. A., Charbonneau, D., Allen, L. E., Burrows, A., & Megeath, S. T. 2008, *ApJ*, 673, 526
- Knutson, H. A., Charbonneau, D., Cowan, N. B., Fortney, J. J., Showman, A. P., Agol, E., & Henry, G. W. 2009, *ApJ*, 703, 769
- Knutson, H. A., Howard, A. W., & Isaacson, H. 2010, *ApJ*, 720, 1569
- Knutson, H. A., Madhusudhan, N., Cowan, N. B., Christiansen, J. L., Agol, E., Deming, D., Désert, J.-M., Charbonneau, D., Henry, G. W., Homeier, D., Langton, J., Laughlin, G., & Seager, S. 2011, *ApJ*, 735, 27
- Langton, J. & Laughlin, G. 2008, *ApJ*, 674, 1106
- Liddle, A. R. 2007, *MNRAS*, 377, L74
- Lodders, K. & Fegley, Jr., B. *Chemistry of Low Mass Substellar Objects*, ed. J. W. Mason, 1
- Machalek, P., McCullough, P. R., Burke, C. J., Valenti, J. A., Burrows, A., & Hora, J. L. 2008, *ApJ*, 684, 1427

- Madhusudhan, N., Harrington, J., Stevenson, K. B., Nymeyer, S., Campo, C. J., Wheatley, P. J., Deming, D., Blečić, J., Hardy, R. A., Lust, N. B., Anderson, D. R., Collier-Cameron, A., Britt, C. B. T., Bowman, W. C., Hebb, L., Hellier, C., Maxted, P. F. L., Pollacco, D., & West, R. G. 2011, *Nature*, 469, 64
- Madhusudhan, N. & Seager, S. 2009, *ApJ*, 707, 24
- . 2010, *ApJ*, 725, 261
- . 2011, *ApJ*, 729, 41
- Mandel, K. & Agol, E. 2002, *ApJ*, 580, L171
- Miller-Ricci Kempton, E., Zahnle, K., & Fortney, J. J. 2012, *ApJ*, 745, 3
- Morales-Calderón, M., Stauffer, J. R., Kirkpatrick, J. D., Carey, S., Gelino, C. R., Barrado y Navascués, D., Rebull, L., Lowrance, P., Marley, M. S., Charbonneau, D., Patten, B. M., Megeath, S. T., & Buzasi, D. 2006, *ApJ*, 653, 1454
- Moses, J. I., Visscher, C., Fortney, J. J., Showman, A. P., Lewis, N. K., Griffith, C. A., Klippenstein, S. J., Shabram, M., Friedson, A. J., Marley, M. S., & Freedman, R. S. 2011, *ApJ*, 737, 15
- Nymeyer, S., Harrington, J., Hardy, R. A., Stevenson, K. B., Campo, C. J., Madhusudhan, N., Collier-Cameron, A., Loredó, T. J., Blečić, J., Bowman, W. C., Britt, C. B. T., Cubillos, P., Hellier, C., Gillon, M., Maxted, P. F. L., Hebb, L., Wheatley, P. J., Pollacco, D., & Anderson, D. R. 2011, *ApJ*, 742, 35
- Peale, S. J. 1999, *ARA&A*, 37, 533
- Pont, F., Bouchy, F., Melo, C., Santos, N. C., Mayor, M., Queloz, D., & Udry, S. 2005, *A&A*, 438, 1123

- Pont, F., Husnoo, N., Mazeh, T., & Fabrycky, D. 2011, MNRAS, 414, 1278
- Pont, F., Knutson, H., Gilliland, R. L., Moutou, C., & Charbonneau, D. 2008, MNRAS, 385, 109
- Pont, F., Zucker, S., & Queloz, D. 2006, MNRAS, 373, 231
- Queloz, D., Anderson, D., Collier Cameron, A., Gillon, M., Hebb, L., Hellier, C., Maxted, P., Pepe, F., Pollacco, D., Ségransan, D., Smalley, B., Triaud, A. H. M. J., Udry, S., & West, R. 2010, A&A, 517, L1+
- Ragozzine, D. & Wolf, A. S. 2009, ApJ, 698, 1778
- Seager, S. & Hui, L. 2002, ApJ, 574, 1004
- Showman, A. P., Fortney, J. J., Lian, Y., Marley, M. S., Freedman, R. S., Knutson, H. A., & Charbonneau, D. 2009, ApJ, 699, 564
- Southworth, J. 2008, MNRAS, 386, 1644
- Spiegel, D. S., Silverio, K., & Burrows, A. 2009, ApJ, 699, 1487
- Stevenson, K. B., Harrington, J., Fortney, J. J., Lored, T. J., Hardy, R. A., Nymeyer, S., Bowman, W. C., Cubillos, P., Bowman, M. O., & Hardin, M. 2012, ApJ, 754, 136
- Stevenson, K. B., Harrington, J., Nymeyer, S., Madhusudhan, N., Seager, S., Bowman, W. C., Hardy, R. A., Deming, D., Rauscher, E., & Lust, N. B. 2010, Nature, 464, 1161
- Werner, M. W., Roellig, T. L., Low, F. J., Rieke, G. H., Rieke, M., Hoffmann, W. F., Young, E., Houck, J. R., Brandl, B., Fazio, G. G., Hora, J. L., Gehrz, R. D., Helou, G., Soifer, B. T., Stauffer, J., Keene, J., Eisenhardt, P., Gallagher, D., Gautier, T. N., Irace, W., Lawrence, C. R., Simmons, L., Van Cleve, J. E., Jura, M., Wright, E. L., & Cruikshank, D. P. 2004, ApJS, 154, 1
- Winn, J. N., Henry, G. W., Torres, G., & Holman, M. J. 2008, ApJ, 675, 1531

Wu, Y. & Murray, N. 2003, *ApJ*, 589, 605

Zahnle, K., Marley, M. S., Freedman, R. S., Lodders, K., & Fortney, J. J. 2009, *ApJ*, 701, L20

CHAPTER 3: A SPITZER FIVE-BAND ANALYSIS OF THE JUPITER-SIZED PLANET TrES-1

Patricio Cubillos^{1,2}, Joseph Harrington^{1,2}, Nikku Madhusudhan³, Andrew S. D. Foster¹, Nate B. Lust¹, Ryan A. Hardy¹, and M. Oliver Bowman¹

¹ *Planetary Sciences Group, Department of Physics, University of Central Florida, Orlando, FL 32816-2385*

² *Max-Planck-Institut für Astronomie, Königstuhl 17, D-69117, Heidelberg, Germany*

³ *Department of Physics and Department of Astronomy, Yale University, New Haven, CT 06511, USA*

Received 6 May 2014.

Accepted 22 October 2014.

Published in *The Astrophysical Journal* 24 November 2014.

Publication reference:

Cubillos, P., Harrington, J., Madhusudhan, N., Foster, A. S. D., Lust, N. B., Hardy, R. A., & Bowman, M. O. 2014, *ApJ*, 797, 42
<http://arxiv.org/abs/1411.3093>

©AAS. Reproduced with permission

3.1 Abstract

With an equilibrium temperature of 1200 K, TrES-1 is one of the coolest hot Jupiters observed by *Spitzer*. It was also the first planet discovered by any transit survey and one of the first exoplanets from which thermal emission was directly observed. We analyzed all *Spitzer* eclipse and transit data for TrES-1 and obtained its eclipse depths and brightness temperatures in the 3.6 μm ($0.083\% \pm 0.024\%$, 1270 ± 110 K), 4.5 μm ($0.094\% \pm 0.024\%$, 1126 ± 90 K), 5.8 μm ($0.162\% \pm 0.042\%$, 1205 ± 130 K), 8.0 μm ($0.0213\% \pm 0.042\%$, 1190 ± 130 K), and 16 μm ($0.33\% \pm 0.12\%$, 1270 ± 310 K) bands. The eclipse depths can be explained, within 1σ errors, by a standard atmospheric model with solar abundance composition in chemical equilibrium, with or without a thermal inversion. The combined analysis of the transit, eclipse, and radial-velocity ephemerides gives an eccentricity $e = 0.033_{-0.031}^{+0.015}$, consistent with a circular orbit. Since TrES-1’s eclipses have low signal-to-noise ratios, we implemented optimal photometry and differential-evolution Markov-chain Monte Carlo (MCMC) algorithms in our Photometry for Orbits, Eclipses, and Transits (POET) pipeline. Benefits include higher photometric precision and $\sim 10\times$ faster MCMC convergence, with better exploration of the phase space and no manual parameter tuning.

3.2 Introduction

Transiting exoplanets offer the valuable chance to measure the light emitted from the planet directly. In the infrared, the eclipse depth of an occultation light curve (when the planet passes behind its host star) constrains the thermal emission from the planet. Furthermore, multiple-band detections allow us to characterize the atmosphere of the planet (e.g., Seager & Deming 2010). Since the first detections of exoplanet occultations—TrES-1 (Charbonneau et al. 2005) and HD 298458b (Deming et al. 2005)—there have been several dozen occultations observed. However, to detect

an occultation requires an exhaustive data analysis, since the planet-to-star flux ratios typically lie below 10^{-3} . For example, for the *Spitzer Space Telescope*, these flux ratios are lower than the instrument's photometric stability criteria (Fazio et al. 2004). In this paper we analyze *Spitzer* follow-up observations of TrES-1, highlighting improvement in light-curve data analysis over the past decade.

TrES-1 was the first exoplanet discovered by a wide-field transit survey (Alonso et al. 2004). Its host is a typical K0 thin-disk star (Santos et al. 2006a) with solar metallicity (Laughlin et al. 2005, Santos et al. 2006b, Sozzetti et al. 2006), effective temperature $T_{\text{eff}} = 5230 \pm 50$ K, mass $M_* = 0.878 \pm 0.040$ solar masses (M_{\odot}), and radius $R_* = 0.807 \pm 0.017$ solar radii (R_{\odot} , Torres et al. 2008). Steffen & Agol (2005) dismissed additional companions (with $M > M_{\oplus}$). Charbonneau et al. (2005) detected the secondary eclipse in the 4.5 and 8.0 μm *Spitzer* bands. Knutson et al. (2007) attempted ground-based eclipse observations in the L band (2.9 to 4.3 μm), but did not detect the eclipse.

The TrES-1 system has been repeatedly observed during transit from ground-based telescopes (Narita et al. 2007, Raetz et al. 2009, Vaňko et al. 2009, Rabus et al. 2009, Hrudková et al. 2009, Sada et al. 2012) and from the *Hubble Space Telescope* (Charbonneau et al. 2007). The analyses of the cumulative data (Butler et al. 2006, Southworth 2008, 2009, Torres et al. 2008) agree (within error bars) that the planet has a mass of $M_p = 0.752 \pm 0.047$ Jupiter masses (M_{Jup}), a radius $R_p = 1.067 \pm 0.022$ Jupiter radii (R_{Jup}), and a circular, 3.03 day orbit, whereas Winn et al. (2007) provided accurate details of the transit light-curve shape. Recently, an adaptive-optics imaging survey (Adams et al. 2013) revealed that TrES-1 has a faint background stellar companion ($\Delta\text{mag} = 7.68$ in the Ks band, or 0.08% of the host's flux) separated by $2.31''$ (1.9 and 1.3 *Spitzer* pixels at 3.6–8 μm and at 16 μm , respectively). The companion's type is unknown.

This paper analyzes all *Spitzer* eclipse and transit data for TrES-1 to constrain the planet’s orbit, atmospheric thermal profile, and chemical abundances. TrES-1’s eclipse has an inherently low signal-to-noise ratio (S/N). Additionally, as one of the earliest *Spitzer* observations, the data did not follow the best observing practices developed over the years. We take this opportunity to present the latest developments in our Photometry for Orbits, Eclipses, and Transits (POET) pipeline (Stevenson et al. 2010, 2012a,b, Campo et al. 2011, Nymeyer et al. 2011, Cubillos et al. 2013) and demonstrate its robustness on low S/N data. We have implemented the differential-evolution Markov-chain Monte Carlo algorithm (DEMC, ter Braak 2006), which explores the parameter phase space more efficiently than the typically-used Metropolis Random Walk with a multivariate Gaussian distribution as the proposal distribution. We also test and compare multiple centering (Gaussian fit, center of light, PSF fit, and least asymmetry) and photometry (aperture and optimal) routines.

Section 3.3 describes the *Spitzer* observations. Section 3.4 outlines our data analysis pipeline. Section 3.5 presents our orbital analysis. Section 3.6 shows the constraints that our eclipse measurements place on TrES-1’s atmospheric properties. Finally, section 3.7 states our conclusions.

3.3 Observations

We analyzed eight light curves of TrES-1 from six *Spitzer* visits (obtained during the cryogenic mission): a simultaneous eclipse observation in the 4.5 and 8.0 μm Infrared Array Camera (IRAC) bands (PI Charbonneau, program ID 227, full-array mode), a simultaneous eclipse observation in the 3.6 and 5.8 μm IRAC bands (PI Charbonneau, program ID 20523, full-array), three consecutive eclipses in the 16 μm Infrared Spectrograph (IRS) blue peak-up array, and one transit visit at 16 μm (PI Harrington, program ID 20605). Table 3.1 shows the *Spitzer* band, date, total duration, frame exposure time, and *Spitzer* pipeline of each observation.

Table 3.1: Observation Information

Event	Band μm	Observation date	Duration hours	Exp. time seconds	<i>Spitzer</i> pipeline
Eclipse	3.6	2005 Sep 17	7.27	1.2	S18.18.0
Eclipse	4.5	2004 Oct 30	5.56	10.4	S18.18.0
Eclipse	5.8	2005 Sep 17	7.27	10.4	S18.18.0
Eclipse	8.0	2004 Oct 30	5.56	10.4	S18.18.0
Ecl. visit 1	16.0	2006 May 17	5.60	31.5	S18.7.0
Ecl. visit 2	16.0	2006 May 20	5.60	31.5	S18.7.0
Ecl. visit 3	16.0	2006 May 23	5.60	31.5	S18.7.0
Transit	16.0	2006 May 15	5.77	31.5	S18.18.0

In 2004, the telescope’s Astronomical Observation Request (AOR) allowed only a maximum of 200 frames (Charbonneau et al. 2005), dividing the 4.8 and 8.0 μm events into eight AORs (Figure 3.1). The later 3.6 and 5.8 μm events consisted of two AORs. The repointings between AORs (~ 0.1 -pixel offsets) caused systematic flux variations, because of IRAC’s well-known position-dependent sensitivity variations (Charbonneau et al. 2005). On the other hand, the pointing of the IRS observations (a single AOR) cycled among four nodding positions every five acquisitions, producing flux variations between the positions.

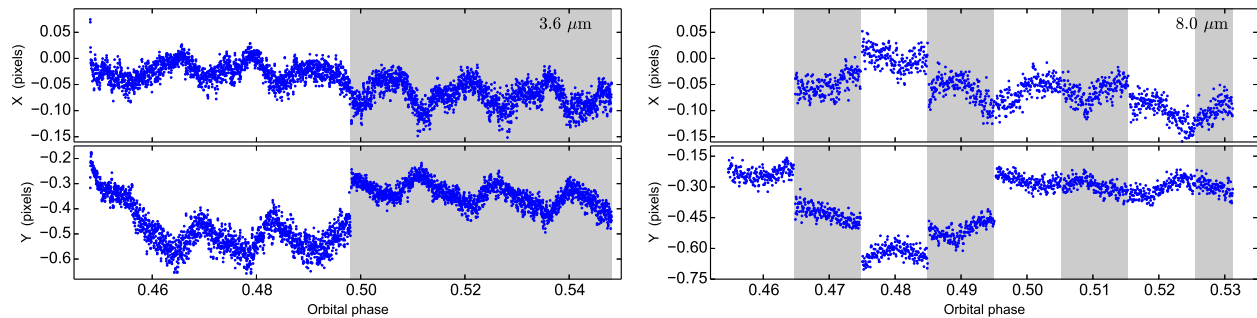


Figure 3.1: **Left:** TrES-1’s x (top) and y (bottom) position on the detector at $3.6\ \mu\text{m}$ vs. orbital phase. The coordinate origin denotes the center of the nearest pixel. The shaded/unshaded areas mark different AORs. The (~ 0.1 pixels) pointing offsets are clear, as well as the usual hour-long pointing oscillation and point-to-point jitter (~ 0.01 pixels). **Right:** Same as the left panel, but for the $8.0\ \mu\text{m}$ light curve. The 5.8 and $4.5\ \mu\text{m}$ datasets were observed simultaneously with the 3.6 and $8.0\ \mu\text{m}$ bands, respectively; hence, their pointing correlates with the ones shown.

3.4 Data Analysis

Our POET pipeline processes Spitzer Basic Calibrated Data to produce light curves, modeling the systematics and eclipse (or transit) signals. Initially, POET flags bad pixels and calculates the frames’ Barycentric Julian Dates (BJD), reporting the frame mid-times in both Coordinated Universal Time (UTC) and Barycentric Dynamical Time (TDB). Next, it estimates the target’s center position using any of four methods: fitting a two-dimensional, elliptical, non-rotating Gaussian with constant background (Stevenson et al. 2010, Supplementary Information); fitting a 100x oversampled point spread function (PSF, Cubillos et al. 2013); calculating the center of light (Stevenson et al. 2010); or calculating the least asymmetry (Lust et al. 2014, submitted). The Gaussian-fit, PSF-fit, and center-of-light methods considered a 15 pixel square window centered on the target’s peak pixel. The least-asymmetry method used a nine pixel square window.

3.4.1 Optimal Photometry

POET generates raw light curves either from interpolated aperture photometry (Harrington et al. 2007, sampling a range of aperture radii in 0.25 pixel increments) or using an optimal photometry algorithm (following Horne 1986), which improves S/N over aperture photometry for low-S/N data sets. Optimal photometry has been implemented by others to extract light curves during stellar occultations by Saturn’s rings (Harrington & French 2010) or exoplanets (Deming et al. 2005, Stevenson et al. 2010). This algorithm uses a PSF model, P_i , to estimate the expected fraction of the sky-subtracted flux, F_i , falling on each pixel, i ; divides it out of F_i so that each pixel becomes an estimate of the full flux (with radially increasing uncertainty); and uses a mean with weights W_i to give an unbiased estimate of the target flux:

$$f = \frac{\sum_i W_i F_i / P_i}{\sum_i W_i}. \quad (3.1)$$

Here, $W_i = P_i^2 / V_i$, with V_i the variance of F_i . Thus,

$$f_{\text{opt}} = \frac{\sum_i P_i F_i / V_i}{\sum_i P_i^2 / V_i}. \quad (3.2)$$

We used the Tiny-Tim program¹ (ver. 2.0) to generate a super-sampled PSF model (100× finer pixel scale than the *Spitzer* data). We shifted the position, binned down the resolution, and scaled the PSF flux to fit the data.

¹<http://irsa.ipac.caltech.edu/data/SPITZER/docs/dataanalysis/tools/contributed/general/stinytim/>

3.4.2 Light Curve Modeling

Considering the position-dependent (intrapixel) and time-dependent (ramp) *Spitzer* systematics (Charbonneau et al. 2005), we modeled the raw light-curve flux, F , as a function of pixel position (x, y) and time t (in orbital phase units):

$$F(x, y, t) = F_s E(t) M(x, y) R(t) A(a), \quad (3.3)$$

where F_s is the out-of-eclipse system flux (fitting parameter). $E(t)$ is an eclipse or transit (small-planet approximation) Mandel & Agol (2002) model. $M(x, y)$ is a Bi-Linearly Interpolated Sub-pixel Sensitivity (BLISS) map (Stevenson et al. 2012a). $R(t)$ is a ramp model and $A(a)$ a per-AOR flux scaling factor. The intrapixel effect is believed to originate from non-uniform quantum efficiency across the pixels (Reach et al. 2005), being more significant at 3.6 and 4.5 μm . At the longer wavebands, the intrapixel effect is usually negligible (e.g., Knutson et al. 2008, 2011, Stevenson et al. 2012a). The BLISS map outperforms polynomial fits for removing *Spitzer*'s position-dependent sensitivity variations (Stevenson et al. 2012a, Blečić et al. 2013).

For the ramp systematic, we tested several equations, $R(t)$, from the literature (e.g., Stevenson et al. 2012a, Cubillos et al. 2013). The data did not support models more complex than:

$$\text{linramp} : R(t) = 1 + r_1(t - t_c) \quad (3.4)$$

$$\text{quadramp} : R(t) = 1 + r_1(t - t_c) + r_2(t - t_c)^2 \quad (3.5)$$

$$\text{logramp} : R(t) = 1 + r_1[\ln(t - t_0)] \quad (3.6)$$

$$\text{risingexp} : R(t) = 1 - e^{-r_1(t-t_0)} \quad (3.7)$$

where t_c is a constant, fixed at orbital phase 0 (for transits) or 0.5 (for eclipses); r_1 and r_2 are a linear and quadratic free parameters, respectively; and t_0 is a time-offset free parameter.

Additionally, the telescope pointing settled at slightly different locations for each AOR, resulting in significant non-overlapping regions between the sets of positions from each AOR (Figure 3.2). Furthermore, the overlapping region is mostly composed of data points taken during the telescope settling (when the temporal variation is stronger). The pointing offsets provided a weak link between the non-overlapping regions of the detector, complicating the construction of the pixel sensitivity map at 3.6 and 4.5 μm . We attempted the correction of Stevenson et al. (2012a), $A(a_i)$, which scales the flux from each AOR, a_i , by a constant factor. To avoid degeneracy, we set $A(a_1) = 1$ and free subsequent factors. This can be regarded as a further refinement to the intrapixel map for 3.6 and 4.5 μm . Just like the ramp models, the AOR-scaling model works as an ad-hoc model that corrects for the *Spitzer* systematic variations.

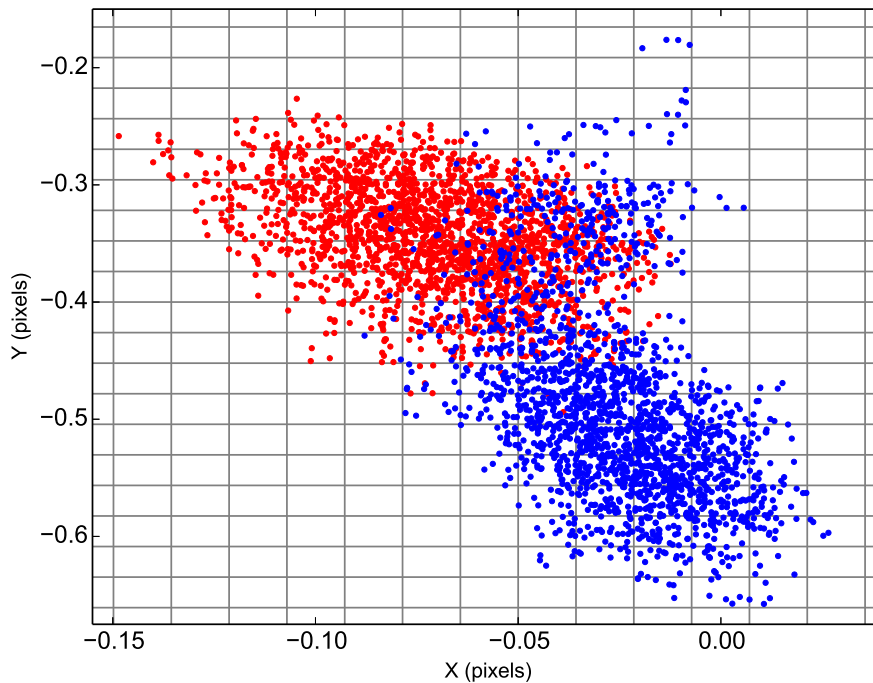


Figure 3.2: 3.6- μm detector pointing. The blue and red points denote the data point from the first and second AOR, respectively. The coordinate origin denotes the center of the nearest pixel. The grid delimits the BLISS-map bin boundaries.

Note that introducing parameters that relate only to a portion of the data violates an assumption of the Bayesian Information Criterion (BIC) used below; the same violation occurs for the BLISS map (see Appendix A of Stevenson et al. 2012a). We have not found an information criterion that handles such parameters, so we ranked these fits with the others, being aware that BIC penalizes them too harshly. It turned out that the AOR-scaling model made a significant improvement only at $3.6 \mu\text{m}$; see Section 3.4.5.7.

To determine the best-fitting parameters, \mathbf{x} , of a model, \mathcal{M} (Equation 3.3 in this case), given the data, \mathbf{D} , we maximize the Bayesian posterior probability (probability of the model parameters given the data and modeling framework, Gregory 2005):

$$P(\mathbf{x}|\mathbf{D}, \mathcal{M}) = P(\mathbf{x}|\mathcal{M}) P(\mathbf{D}|\mathbf{x}, \mathcal{M})/P(\mathbf{D}|\mathcal{M}), \quad (3.8)$$

where $P(\mathbf{D}|\mathbf{x}, \mathcal{M})$ is the usual likelihood of the data given the model and $P(\mathbf{x}|\mathcal{M})$ is any prior information on the parameters. Assuming Gaussian-distributed priors, maximizing Equation (3.8) can be turned into a problem of minimization:

$$\min \left\{ \sum_j \left(\frac{\mathbf{x}_j - p_j}{\sigma_j} \right)^2 + \sum_i \left(\frac{\mathcal{M}_i(\mathbf{x}) - \mathbf{D}_i}{\sigma_i} \right)^2 \right\}, \quad (3.9)$$

with p_j a prior estimation (with standard deviation σ_j). The second term in Equation (3.9) corresponds to χ^2 . We used the Levenberg-Marquardt minimizer to find \mathbf{x}_j (Levenberg 1944, Marquardt 1963). Next we sampled the parameters' posterior distribution through a Markov-chain Monte Carlo (MCMC) algorithm to estimate the parameter uncertainties, requiring the Gelman-Rubin statistic (Gelman & Rubin 1992) to be within 1% of unity for each free parameter before declaring convergence.

3.4.3 Differential Evolution Markov Chain

The MCMC’s performance depends crucially on having good proposal distributions to efficiently explore the parameter space. Previous POET versions used the Metropolis random walk, where new parameter sets are proposed from a multivariate normal distribution. The algorithm’s efficiency was limited by the heuristic tuning of the characteristic jump sizes for each parameter. Too-large values yielded low acceptance rates, while too-small values wasted computational power. Furthermore, highly correlated parameter spaces required additional orthogonalization techniques (Stevenson et al. 2012a) to achieve reasonable acceptance ratios, and even then did not always converge.

We eliminated the need for manual tuning and orthogonalization by implementing the differential-evolution Markov-chain algorithm (DEMC, ter Braak 2006), which automatically adjusts the jumps’ scales and orientations. Consider \mathbf{x}_n^i as the set of free parameters of a chain i at iteration n . DEMC runs several chains in parallel, drawing the parameter values for the next iteration from the difference between the current parameter states of two other randomly-selected chains, j and k :

$$\mathbf{x}_{n+1}^i = \mathbf{x}_n^i + \gamma (\mathbf{x}_n^j - \mathbf{x}_n^k) + \gamma_2 \mathbf{e}_n^i, \quad (3.10)$$

where γ is a scaling factor of the proposal jump. Following ter Braak (2006), we selected $\gamma = 2.38/\sqrt{2d}$ (with d being the number of free parameters) to optimize the acceptance probability ($\gtrsim 25\%$, Roberts et al. 1997). The last term, $\gamma_2 \mathbf{e}$, is a random distribution (of smaller scale than the posterior distribution) that ensures a complete exploration of posterior parameter space. We chose a multivariate normal distribution for \mathbf{e} , scaled by the factor γ_2 .

As noted by Eastman et al. (2013), each parameter of \mathbf{e} requires a specific jump scale. One way to estimate the scales is to calculate the standard deviation of the parameters in a sample chain run. In a second method (similar to that of Eastman et al. 2013), we searched for the limits around the best-fitting value where χ^2 increased by 1 along the parameter axes. We varied each parameter separately, keeping the other parameters fixed. Then, we calculated the jump scale from the difference between the upper and lower limits, $(\mathbf{x}^{\text{up}} - \mathbf{x}^{\text{lo}})/2$. Both methods yielded similar results in our tests. By testing different values for γ_2 , provided that $|\gamma_2 \mathbf{e}_n^i| < |\gamma(\mathbf{x}_n^j - \mathbf{x}_n^k)|$, we found that each trial returned identical posterior distributions and acceptance rates, so we arbitrarily set $\gamma_2 = 0.1$.

3.4.4 Data Set and Model Selection

To determine the best raw light curve (i.e., the selection of centering and photometry method), we minimized the standard deviation of the normalized residuals (SDNR) of the light-curve fit (Campo et al. 2011). This naturally prefers good fits and low-dispersion data.

We use Bayesian hypothesis testing to select the model best supported by the data. Following Raftery (1995), when comparing two models \mathcal{M}_1 and \mathcal{M}_2 on a data set \mathbf{D} , the posterior odds (B_{21} , also known as Bayes factor) indicates the model preferred by the data and the extent to which it is preferred. Assuming that either model is, a priori, equally probable, the posterior odds are given by:

$$B_{21} = \frac{p(\mathbf{D}|\mathcal{M}_2)}{p(\mathbf{D}|\mathcal{M}_1)} = \frac{p(\mathcal{M}_2|\mathbf{D})}{p(\mathcal{M}_1|\mathbf{D})} \approx \exp\left(-\frac{\text{BIC}_2 - \text{BIC}_1}{2}\right). \quad (3.11)$$

This is the \mathcal{M}_2 -to- \mathcal{M}_1 probability ratio for the models (given the data), with $\text{BIC} = \chi^2 + k \ln N$ the Bayesian Information Criterion (Liddle 2007), k the number of free parameters, and N the number of points. Hence, \mathcal{M}_2 has a fractional probability of

$$p(\mathcal{M}_2|\mathbf{D}) = \frac{1}{1 + 1/B_{21}}. \quad (3.12)$$

We selected the best models as those with the lowest BIC, and assessed the fractional probability of the others (with respect to the best one) using Equation (3.12).

Recently, Gibson (2014) proposed to marginalize over systematics models rather than use model selection. Although this process is still subjected to the researcher’s choice of systematics models to test, it is a more robust method. Unfortunately, unless we understand the true nature of the systematics to provide a physically motivated model, the modeling process will continue to be an arbitrary procedure. Most of our analyses prefer one of the models over the others. When a second model shows a significant fractional probability (> 0.2) we reinforce our selection based on additional evidence (is the model physically plausible? or how do the competing models perform in a joint fit?). We are evaluating to include the methods of Gibson (2014) to our pipeline in the future.

3.4.5 *Light Curve Analyses*

We initially fit the eclipse light curves individually to determine the best data sets (centering and photometry methods) and systematics models. Then, we determined the definitive parameters from a final joint fit (Section 3.4.5.7) with shared eclipse parameters. For the eclipse model we fit the midpoint, depth, duration, and ingress time (while keeping the egress time equal to the ingress time). Given the low S/N of the data, the individual events do not constrain all the eclipse

parameters well. However, the final joint fit includes enough data to do the job. For the individual fits, we assumed a negligible orbital eccentricity, as indicated by transit and radial-velocity (RV) data, and used the transit duration (2.497 ± 0.012 hr) and transit ingress/egress time (18.51 ± 0.63 min) from Winn et al. (2007) as priors on the eclipse duration and ingress/egress time. In the final joint-fit experiments, we freed these parameters.

3.4.5.1 IRAC-3.6 μm Eclipse

This observation is divided into two AORs at phase 0.498, causing a systematic flux offset due to IRAC’s intrapixel sensitivity variations. We tested aperture photometry between 1.5 and 3.0 pixels. The eclipse depth is consistent among the apertures, and the minimum SDNR occurs for the 2.5 pixel aperture with Gaussian-fit centering (Figure 3.3).

Table 3.2 shows the best four model fits at the best aperture; ΔBIC is the BIC difference with respect to the lowest BIC. Given the relatively large uncertainties, more-complex models are not supported, due to the penalty of the additional free parameters. The Bayesian Information Criterion favors the AOR-scaling model (Table 3.3, last column).

Table 3.2: 3.6 μm Eclipse - Ramp Model Fits^a

$R(t)$	$A(a)$	Ecl. Depth ^b (%)	Midpoint (phase)	SDNR	ΔBIC	$p(\mathcal{M}_2 D)$
	$A(a)$	0.083(24)	0.501(4)	0.0053763	0.0	...
	quadramp	0.158(29)	0.492(2)	0.0053712	2.8	0.19
	risingexp	0.146(25)	0.492(2)	0.0053715	2.9	0.19
	linramp	0.093(23)	0.492(3)	0.0053814	7.4	0.02

Notes.

^a Fits for Gaussian-fit centering and 2.5 pixel aperture photometry.

^b For this and the following tables, the values quoted in parenthesis indicate the 1σ uncertainty corresponding to the least significant digits.

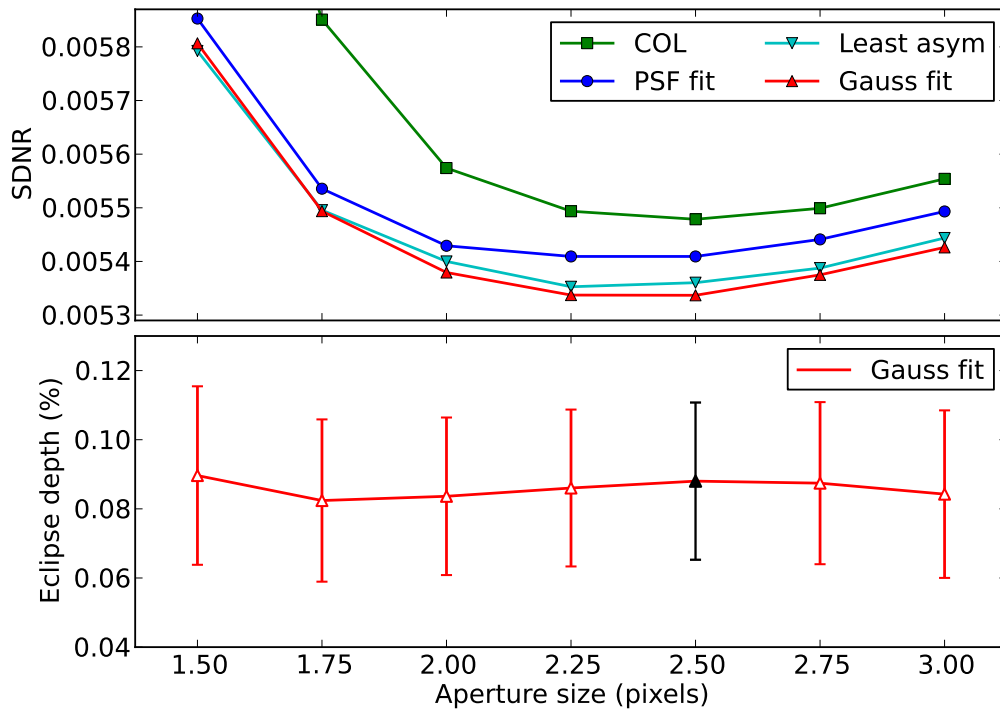


Figure 3.3: **Top:** $3.6\ \mu\text{m}$ eclipse light-curve SDNR vs. aperture. The legend indicates the centering method used. All curves used the best ramp model from Table 3.2. **Bottom:** Eclipse depth vs. aperture for Gaussian-fit centering, with the best aperture (2.5 pixels) in black.

Although the fractional probabilities of the quadratic and exponential ramp models are not negligible, we discard them based on the estimated midpoints, which differ from a circular orbit by 0.008 (twice the ingress/egress duration). It is possible that a non-uniform brightness distribution can induce offsets in the eclipse midpoint (Williams et al. 2006), and these offsets can be wavelength dependent. However, this relative offset can be at most the duration of the ingress/egress. Therefore, disregarding non-uniform brightness offsets, considering the lack of evidence for transit-timing variations and that all other data predict a midpoint consistent with a circular orbit, the $3.6\ \mu\text{m}$ offset must be caused by systematic effects. The AOR-scaling model is the only one that yields a midpoint consistent with the rest of the data. Our joint-fit analysis (Section 3.4.5.7) will provide further support to our model selection.

We adjusted the BLISS map model following Stevenson et al. (2012a). For a minimum of 4 points per bin, the eclipse depth remained constant for BLISS bin sizes similar to the rms of the frame-to-frame position difference (0.014 and 0.026 pixels in x and y , respectively). Figure 3.4 shows the raw, binned, and systematics-corrected light curves with their best-fitting models.

To estimate the contribution from time-correlated residuals we calculated the time-averaging rms-vs.-bin-size curves (Pont et al. 2006, Winn et al. 2008). This method compares the binned-residuals rms to the uncorrelated-noise (Gaussian noise) rms. An excess rms over the Gaussian rms would indicate a significant contribution from time-correlated residuals. Figure 3.4 (bottom-center and bottom-right panels) indicates that time-correlated noise is not significant at any time scale, for any of our fits.

3.4.5.2 *IRAC-4.5 μm Eclipse*

Our analysis of the archival data revealed that the 4.5 μm data suffered from multiplexer bleed, or “muxbleed”, indicated by flagged pixels near the target in the mask frames and data-frame headers indicating a muxbleed correction. Muxbleed is an effect observed in the IRAC InSb arrays (3.6 and 4.5 μm) wherein a bright star trails in the fast-read direction for a large number of consecutive readouts. Since there are 4 readout channels, the trail appears every 4 pixels, induced by one or more bright pixels² (Figure 3.5).

² <http://irsa.ipac.caltech.edu/data/SPITZER/docs/irac/iracinstrumenthandbook/59/>

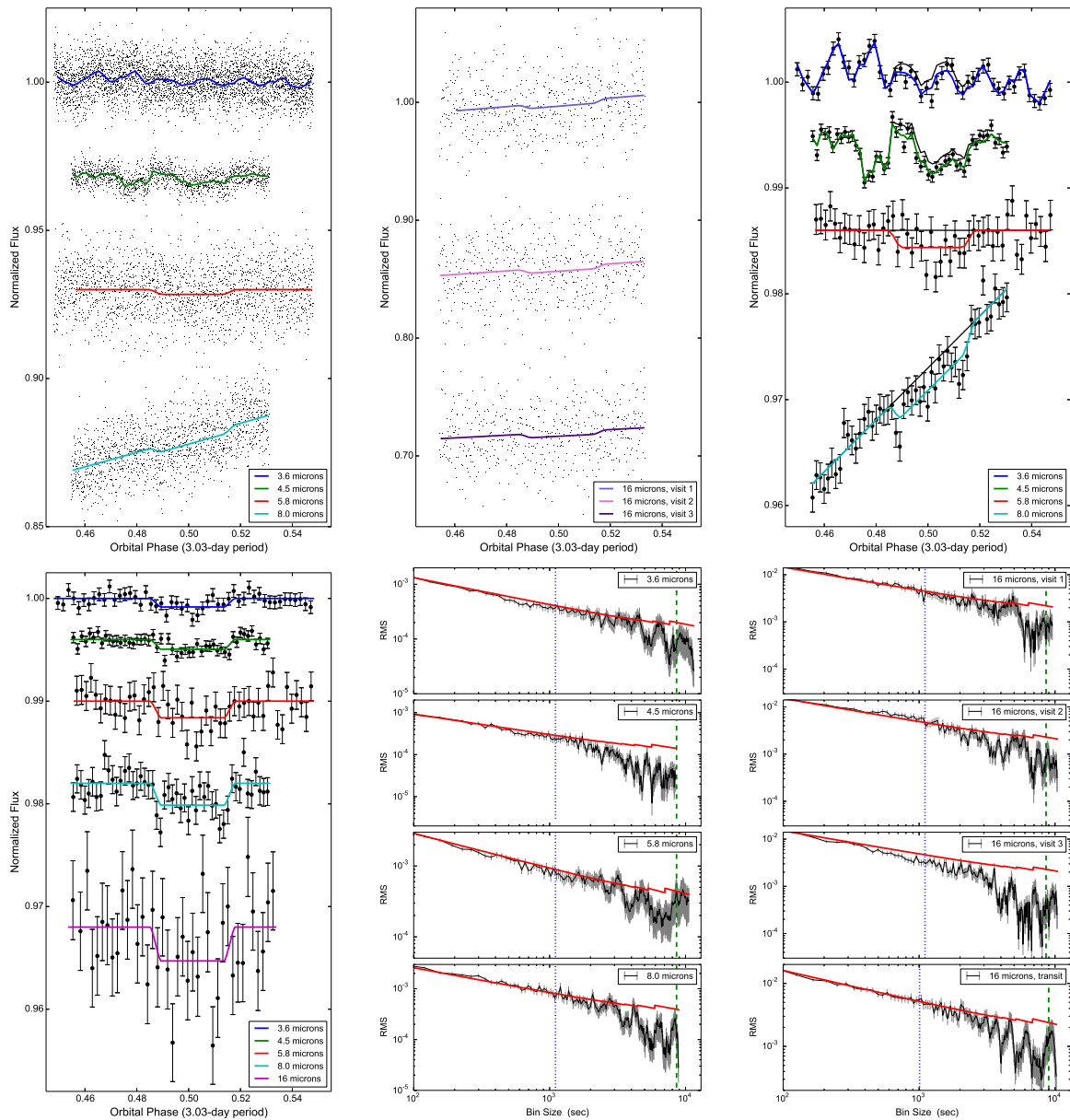


Figure 3.4: TrES-1 secondary-eclipse light curves and rms-vs.-bin size plots. Raw light curves are in the top-left and top-center panels. Binned IRAC data are in the top-right panel, and systematics-corrected traces are in the bottom-left panel. The system flux is normalized and the curves are shifted vertically for clarity. The colored solid curves are the best-fit models, while the black solid curves are the best-fit models excluding the eclipse component. The error bars give the 1σ uncertainties. The bottom-center and bottom-right panels show the fit residuals' rms (black curves with 1σ uncertainties) vs. bin size. The red curves are the expected rms for Gaussian noise. The blue dotted and green dashed vertical lines mark the ingress/egress time and eclipse duration, respectively.

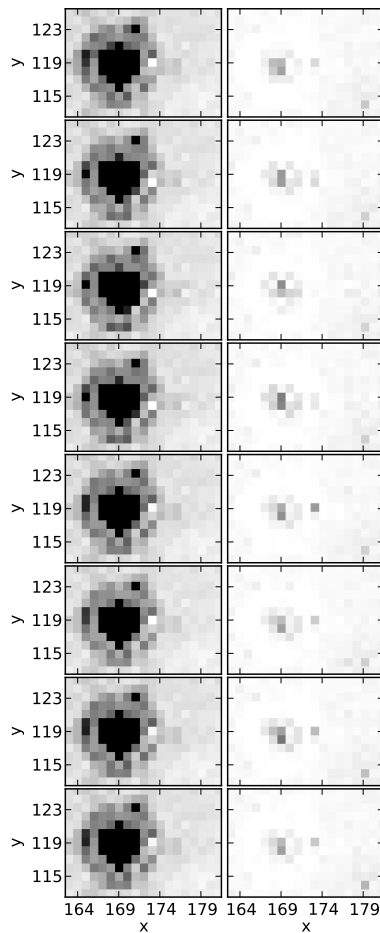


Figure 3.5: **Left:** Per-AOR mean of the *Spitzer* BCD frames at $4.5 \mu\text{m}$ around TrES-1. **Right:** Per-AOR rms divided by the square root of the mean BCD frames at $4.5 \mu\text{m}$. The flux is in electron counts, the color scales range from the 2.5th (white) to the 97.5th (black) percentile of the flux distribution. TrES-1's center is located near $x = 169, y = 119$. The miscalculated muxbleed-corrected pixels stand out at 4 and (sometimes) 8 pixels to the right of the target center. The excess in the scaled rms confirms that the muxbleed correction is not linearly scaled with the flux. The pixels around the target center also show high rms values, which might be due to the 0.2 pix motion of the PSF centers.

TrES-1 (whose flux was slightly below the nominal saturation limit at $4.5 \mu\text{m}$) and a second star that is similarly bright fit the muxbleed description. We noted the same feature in the BCD frames used by Charbonneau et al. (2005, *Spitzer* pipeline version S10.5.0). Their headers indicated a muxbleed correction as well, but did not clarify whether or not a pixel was corrected.

Since the signal is about 10^{-3} times the stellar flux level, every pixel in the aperture is significant and any imperfectly made local correction raises concern (this is why we do not interpolate bad pixels in the aperture, but rather discard frames that have them). Nevertheless, we analyzed the data, ignoring the muxbleed flags, to compare it to the results of Charbonneau et al. (2005). In the atmospheric analysis that follows, we model the planet both with and without this data set.

This light curve is also mainly affected by the intrapixel effect. Since the $4.5 \mu\text{m}$ light curve consisted of 8 AORs, some of which are entirely in- or out-of-eclipse, making the AOR-scale model to overfit the data. We tested apertures between 2.5 and 4.5 pixels, finding the lowest SDNR for the center-of-light centering method at the 3.75-pixel aperture (Figure 3.6). This alone is surprising, as it may be the first time in our experience that center of light is the best method. In the same manner as for the $3.6 \mu\text{m}$ data, we selected BLISS bin sizes of 0.018 (x) and 0.025 (y) pixels, for 4 minimum points per bin. A fit with no ramp model minimized BIC (Table 3.3). Figure 3.4 shows the data and best-fitting light curves and the rms-vs.-bin size plot.

Table 3.3: $4.5 \mu\text{m}$ Eclipse - Ramp Model Fits^a

$R(t)$	$A(a)$	Ecl. Depth (%)	SDNR	ΔBIC	$p(\mathcal{M}_2 D)$
no-model		0.090(28)	0.0026543	0.0	...
linramp		0.091(27)	0.0026531	6.0	0.05
risingexp		0.131(32)	0.0026469	7.1	0.03
quadamp		0.153(39)	0.0026481	8.7	0.01
logramp		0.090(22)	0.0026532	13.3	1×10^{-3}
$A(a)$		0.140(43)	0.0026474	38.5	4×10^{-9}

Note. ^a Fits for center-of-light centering and 3.75-pixel aperture photometry.

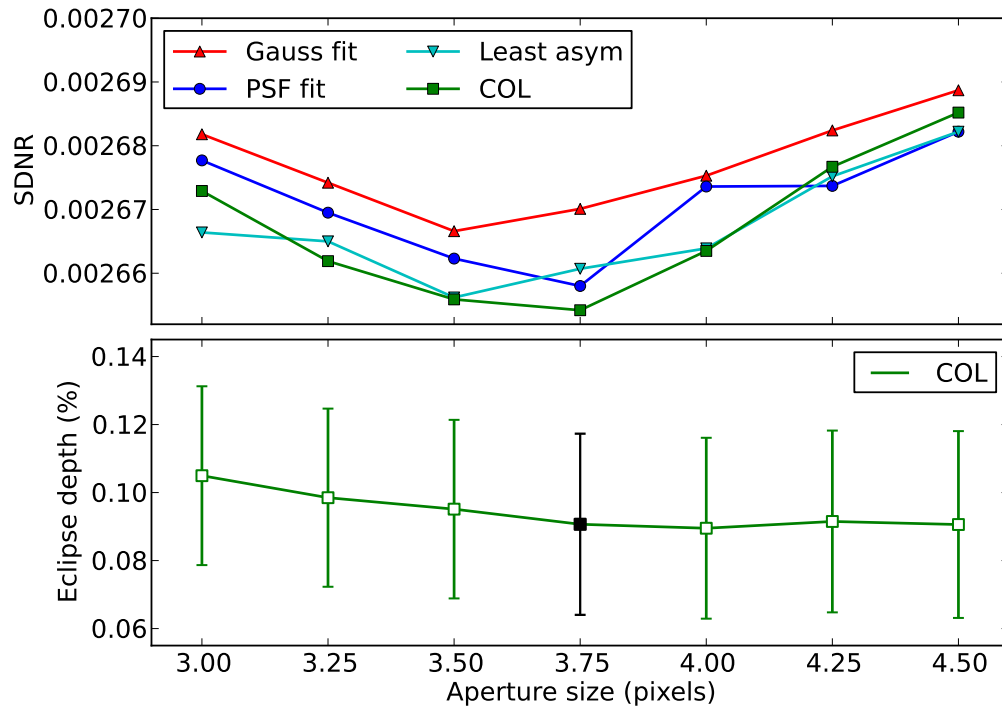


Figure 3.6: **Top:** 4.5 μm eclipse light-curve SDNR vs. aperture. The legend indicates the centering method used. All curves used the best ramp model from Table 3.3. **Bottom:** Eclipse depth vs. aperture for center-of-light centering, with the best aperture (3.75 pixels) in black.

3.4.5.3 IRAC-5.8 μm Eclipse

These data are not affected by the intrapixel effect. We sampled apertures between 2.25 and 3.5 pixels. Least-asymmetry centering minimized the SDNR at 2.75 pixels, with all apertures returning consistent eclipse depths (Figure 3.7). The BIC comparison favors a fit without AOR-scale nor ramp models, although, at some apertures the midpoint posterior distributions showed a hint of bi-modality. The eclipse depth, however, remained consistent for all tested models (Table 3.4). Figure 3.4 shows the data and best-fitting light curves and rms-vs.-bin size plot.

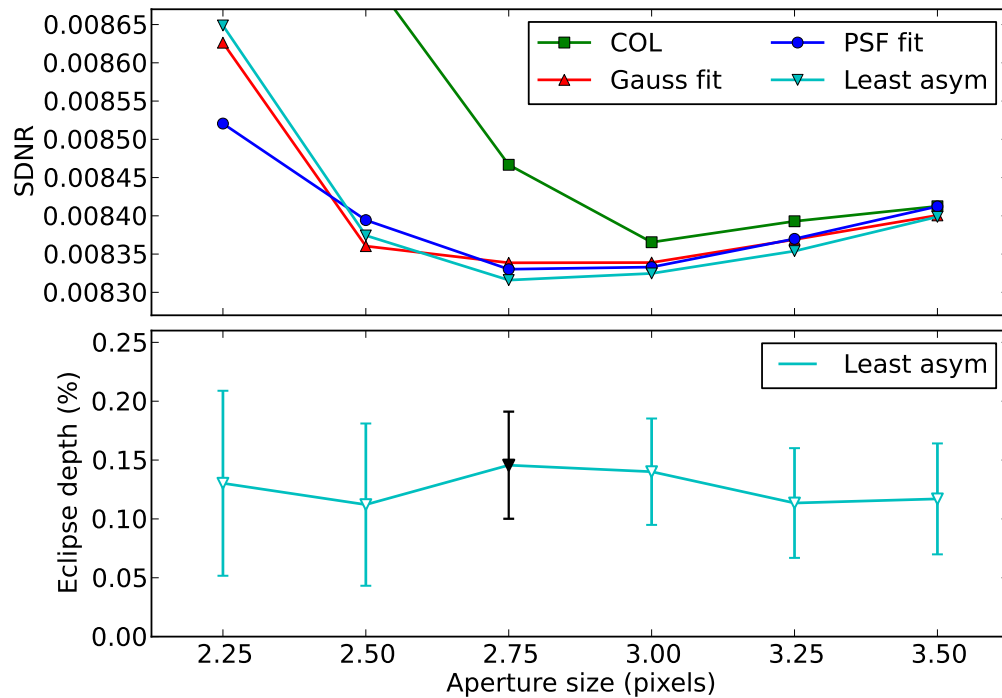


Figure 3.7: **Top:** 5.8 μm eclipse light-curve SDNR vs. aperture. The legend indicates the centering method used. All curves used the best ramp model from Table 3.4. **Bottom:** Eclipse depth vs. aperture for least-asymmetry centering, with the best aperture (2.75 pixels) in black.

Table 3.4: 5.8 μm Eclipse - Ramp Model Fits^a

$R(t)$	$A(a)$	Ecl. Depth (%)	SDNR	ΔBIC	$p(\mathcal{M}_2 D)$
no-model		0.158(44)	0.0083287	0.0	...
	$A(a)$	0.142(45)	0.0083220	4.4	0.10
	linramp	0.154(44)	0.0083281	7.2	0.03
	quadramp	0.100(54)	0.0083259	13.0	2×10^{-3}
	risingexp	0.158(44)	0.0083287	14.9	6×10^{-4}

Note. ^a Fits for least-asymmetry centering and 2.75-pixel aperture photometry.

3.4.5.4 IRAC-8.0 μm Eclipse

This data set had eight AOR blocks. We tested aperture photometry from 1.75 to 3.5 pixels. Again, least-asymmetry centering minimized the SDNR for the 2.75-pixel aperture (Figure 3.8). We attempted fitting with the per-AOR adjustment $A(a)$, but the seven additional free parameters introduced a large BIC penalty, and the many parameters certainly alias with the eclipse. The linear ramp provided the lowest BIC (Table 3.5). Figure 3.4 shows the data and best-fitting light curves and rms-vs.-bin size plot.

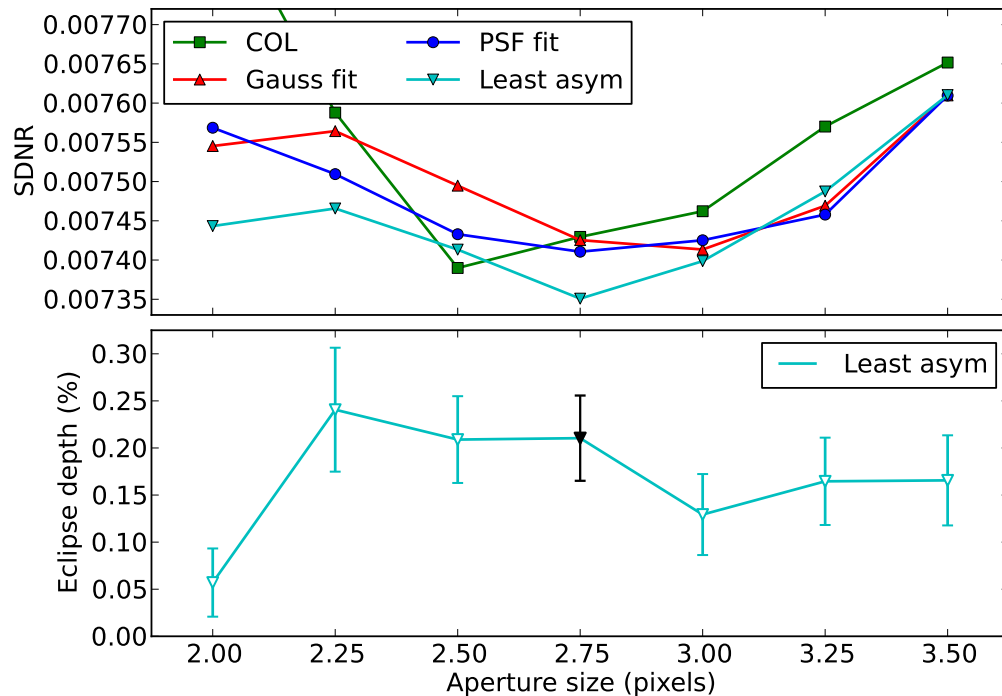


Figure 3.8: **Top:** 8.0 μm eclipse light-curve SDNR vs. aperture. The legend indicates the centering method used. All curves used the best ramp model from Table 3.5. **Bottom:** Eclipse depth vs. aperture for least-asymmetry centering, with the best aperture (2.75 pixels) in black. This data set had the greatest eclipse-depth variations per aperture.

Table 3.5: 8.0 μm Eclipse - Ramp Model Fits^a

$R(t) A(a)$	Ecl. Depth (%)	SDNR	ΔBIC	$p(\mathcal{M}_2 D)$
linramp	0.208(45)	0.0073506	0.0	...
quadramp	0.267(62)	0.0073388	3.3	0.16
risingexp	0.278(53)	0.0073389	3.4	0.15
logramp	0.304(45)	0.0073471	7.0	0.03
linramp- $A(a)$	0.759(185)	0.0073112	41.8	8×10^{-10}

Note. ^a Fits for least-asymmetry centering and 2.75-pixel aperture photometry.

3.4.5.5 IRS-16 μm Eclipses

These data come from three consecutive eclipses and present similar systematics. The telescope cycled among four nodding positions every five acquisitions. As a result, each position presented a small flux offset ($\lesssim 2\%$). Since the four nod positions are equally sampled throughout the entire observation, they should each have the same mean level. We corrected the flux offset by dividing each frame’s flux by the nodding-position mean flux and multiplying by the overall mean flux, improving SDNR by $\sim 6\%$. We tested aperture photometry from 1.0 to 5.0 pixels. In all visits the SDNR minimum was at an aperture of 1.5 pixels; however, optimal photometry outperformed aperture photometry (Figure 3.9). The second visit provided the clearest model determination (Table 3.6).

Table 3.6: 16 μm Eclipse, Visit 2—Individual Ramp Model Fits^a

$R(t)$	Ecl. Depth (%)	SDNR	ΔBIC	$p(\mathcal{M}_2 D)$
linramp	0.50(24)	0.0233022	0.0	...
no-ramp	0.40(19)	0.0235462	4.1	0.11
quadramp	0.74(28)	0.0232539	5.3	0.06
risingexp	0.68(22)	0.0232595	5.3	0.06

Note. ^a Fits for PSF-fit centering and optimal photometry.

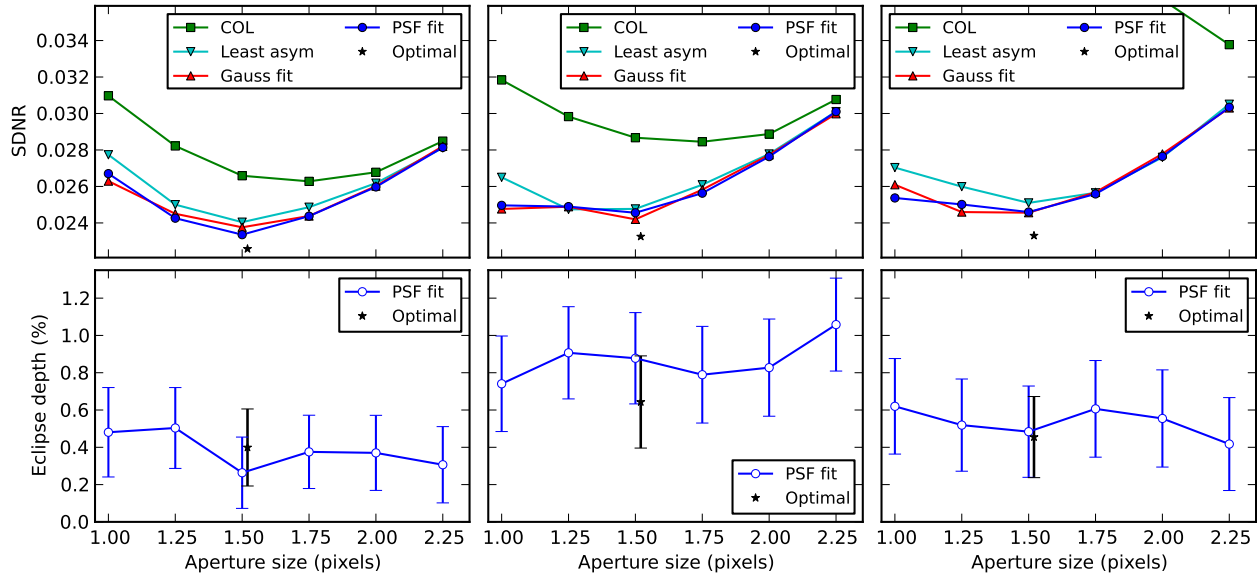


Figure 3.9: **Top:** 16- μm eclipse light-curves SDNR vs. aperture (from left to right, the first, second, and third visits, respectively). The legend indicates the centering method used; additionally, the optimal-photometry calculation uses the PSF-fit centering positions but does not involve an aperture. We plotted the optimal-photometry results next to the best-aperture location (for ease of comparison). Each curve used the best ramp model from Tables 3.6, 3.7, and 3.8, respectively. **Bottom:** Eclipse depth vs. aperture for PSF-fit centering, with the best one (optimal photometry) in black.

At the beginning of the third visit (40 frames, ~ 28 min), the target position departs from the rest by half a pixel; omitting the first 40 frames did not improve SDNR. The linear ramp model minimized BIC (Table 3.7). Even though ΔBIC between the linear and the no-ramp models was small, the no-ramp residuals showed a linear trend, thus we are confident on having selected the best model. The eclipse light curve in this visit is consistent with that of the second visit.

Table 3.7: 16 μm Eclipse, Visit 3—Individual Ramp Model Fits^a

$R(t)$	Ecl. Depth (%)	SDNR	ΔBIC	$p(\mathcal{M}_2 D)$
linramp	0.48(21)	0.0233010	0.0	...
no-ramp	0.24(18)	0.0234888	1.1	0.37
quadramp	0.38(22)	0.0233004	5.8	0.05
risingexp	0.48(20)	0.0233011	6.2	0.04

Note. ^a Fits for PSF-fit centering and optimal photometry.

The eclipse of the first visit had the lowest S/N of all. The free parameters in both minimizer and MCMC easily ran out of bounds towards implausible solutions. For this reason we determined the best model in a joint fit combining all three visits. The events shared the eclipse midpoint, duration, depth, and ingress/egress times. We used the best data sets and models from the second and third visits and tested different ramp models for the first visit. With this configuration, the linear ramp model minimized the BIC of the joint fit (Table 3.8). Here, the target locations in the first two nodding cycles also were shifted with respect to the rest of the frames. Clipping them out improved the SDNR. Figure 3.4 shows the data and best-fitting light curves and rms-vs.-bin size plot.

Table 3.8: 16 μm Eclipse, Visit 1—Ramp Model Fits^a

$R(t)$	Ecl. Depth (%)	SDNR	ΔBIC	$p(\mathcal{M}_2 D)$
tr001bs51	Joint	Joint	Joint	tr001bs51
linramp	0.35(14)	0.0230156	0.00	...
quadramp	0.32(14)	0.0230172	7.10	0.03
risingexp	0.36(11)	0.0230152	7.31	0.02
no-ramp	0.33(13)	0.0231502	10.16	6×10^{-3}

Note. ^a Fits for PSF-fit centering and optimal photometry.

3.4.5.6 IRS-16 μm Transit

To fit this light curve we used the Mandel & Agol (2002) small-planet transit model with a quadratic limb-darkening law. We included priors on the model parameters that were poorly constrained by our data. We adopted $\cos(i) = 0.0_{-0.0}^{+0.019}$ and $a/R_\star = 10.52_{-0.18}^{+0.02}$ from Torres et al. (2012) and the quadratic-limb darkening coefficients $u_1 = 0.284 \pm 0.061$ and $u_2 = 0.21 \pm 0.12$, which translate into our model parameters as $c_2 = u_1 + 2u_2 = -0.7 \pm 0.25$ and $c_4 = -u_2 = -0.21 \pm 0.12$ (with $c_1 = c_3 = 0$) from Winn et al. (2007). The midpoint and planet-to-star radius ratio completed the list of free parameters for the transit model.

We tested aperture photometry between 1 and 2 pixels, finding the SDNR minimum at 1.5 pixels for the Gaussian-fit centering method (Figure 3.10). Table 3.9 shows the ramp-model fitting results. The linear ramp minimized BIC followed by the quadratic ramp with a 0.33 fractional probability; however, the quadratic fit shows an unrealistic upward curvature due to high points at the end of the observation. Figures 3.11 and 3.4 show the best fit to the light curve and the rms-vs.-bin size plot, respectively.

Table 3.9: 16 μm Transit—Ramp Model Fits^a

$R(t)$	R_p/R_\star	SDNR	ΔBIC	$p(\mathcal{M}_2 D)$
linramp	0.1314(86)	0.0247755	0.0	...
quadramp	0.1069(224)	0.0247118	1.4	0.33
risingexp	0.1314(92)	0.0247757	6.2	0.04
logramp	0.1316(81)	0.0247768	6.3	0.04
no-ramp	0.1306(89)	0.0250938	6.9	0.03

Note. ^a Fits for Gaussian-fit centering and 1.5-pixel aperture photometry.

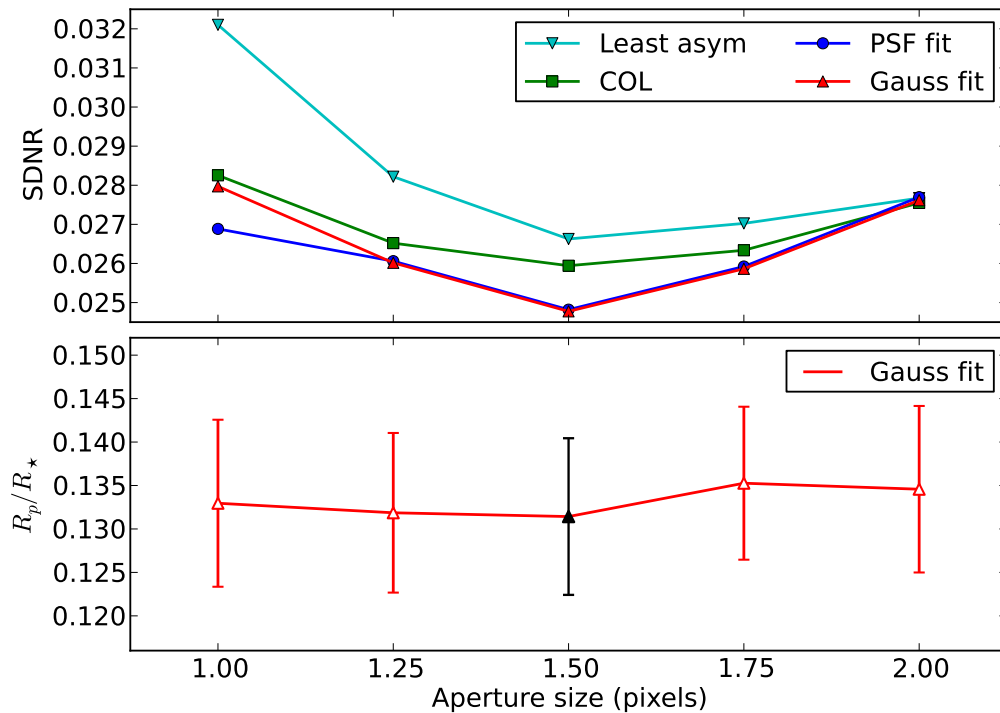


Figure 3.10: **Top:** 16- μm transit light-curve SDNR vs. aperture. All curves used the best ramp model from Table 3.9. **Bottom:** Planet-to-star radius ratio vs. aperture for least asymmetry centering, with the best aperture (2.75 pixels) in black.

3.4.5.7 Joint-fit Analysis

We used the information from all eclipse light curves combined to perform a final joint-fit analysis. The simultaneous fit shared a common eclipse duration, eclipse midpoint and eclipse ingress/egress time among all light curves. Additionally, the three IRS eclipses shared the eclipse-depth parameter. We further released the duration prior (which assumed a circular orbit). We also performed experiments related to the 3.6 and 4.5 μm datasets.

First, to corroborate our selection of the 3.6 μm model, we compared the different 3.6 μm models in the joint-fit configuration both with the shared-midpoint constraint and with independently-fit midpoints per waveband (Tables 3.10 and 3.11).

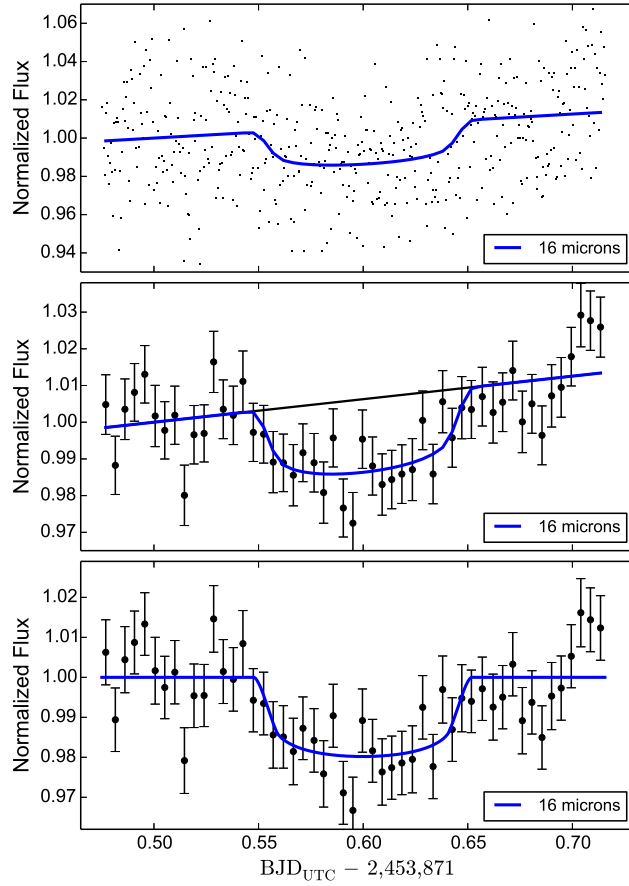


Figure 3.11: Raw (top), binned (middle), and systematics-corrected (bottom) normalized TrES-1 transit light curves at 16 μm . The colored curves are the best-fit models. The black curve is the best-fit model excluding the transit component. The error bars are 1σ uncertainties.

All wavebands other than 3.6 μm agreed with an eclipse midpoint slightly larger than 0.5. When we fit the midpoint separately for each waveband, only the AOR-scale model at 3.6 μm agreed with the other bands' midpoint (note that the 5.8 μm data were obtained simultaneously with the 3.6 μm data, and should have the same midpoint). The posterior distributions also showed midpoint multimodality between these two solutions (Figure 3.12). On the other hand, with a shared midpoint, the 3.6 μm band assumed the value of the other bands for all models, with no multimodality. All but the AOR-scale model showed time-correlated noise, further supporting it as the best choice.

Table 3.10: 3.6 μm Eclipse Models—Eclipse-joint Fits

$R(t)A(a)$	ΔBIC 3.6 μm	3.6 μm Ecl. Depth (%)	Midpoint (phase)	Duration (phase)
Independently fit midpoints ^a :				
$A(a)$	0.0	0.09(2)	...	0.032(1)
quadrap	2.3	0.16(2)	...	0.032(1)
risingexp	2.9	0.15(2)	...	0.032(1)
linramp	6.9	0.10(2)	...	0.032(1)
Shared midpoint:				
$A(a)$	0.0	0.08(2)	0.5015(6)	0.0328(9)
quadrap	13.3	0.14(3)	0.5013(5)	0.0331(9)
linramp	14.2	0.08(2)	0.5015(6)	0.0328(9)
risingexp	15.0	0.12(2)	0.5013(5)	0.0330(9)

Note. ^a Midpoint values in Table 3.11.

Table 3.11: Midpoint per Waveband—Eclipse-joint Fit

$R(t)A(a)$	3.6 μm (phase)	4.5 μm (phase)	5.8 μm (phase)	8.0 μm (phase)	16 μm (phase)
$A(a)$	0.500(3)	0.503(1)	0.502(4)	0.501(1)	0.499(3)
quadrap	0.493(2)	0.503(1)	0.502(4)	0.501(1)	0.500(4)
risingexp	0.493(1)	0.503(1)	0.502(4)	0.501(1)	0.500(3)
linramp	0.491(1)	0.503(1)	0.507(4)	0.501(1)	0.499(3)

Second, we investigated the impact of the (potentially corrupted) 4.5 μm data set on the joint-fit values. Excluding the 4.5 μm event from the joint fit does not significantly alter the midpoint (phase 0.5011 ± 0.0006) nor the duration (0.0326 ± 0.013). Our final joint fit configuration uses the AOR-scaling model for the 3.6 μm band, includes the 4.5 μm light curve, and shares the eclipse midpoint (Table 3.14).

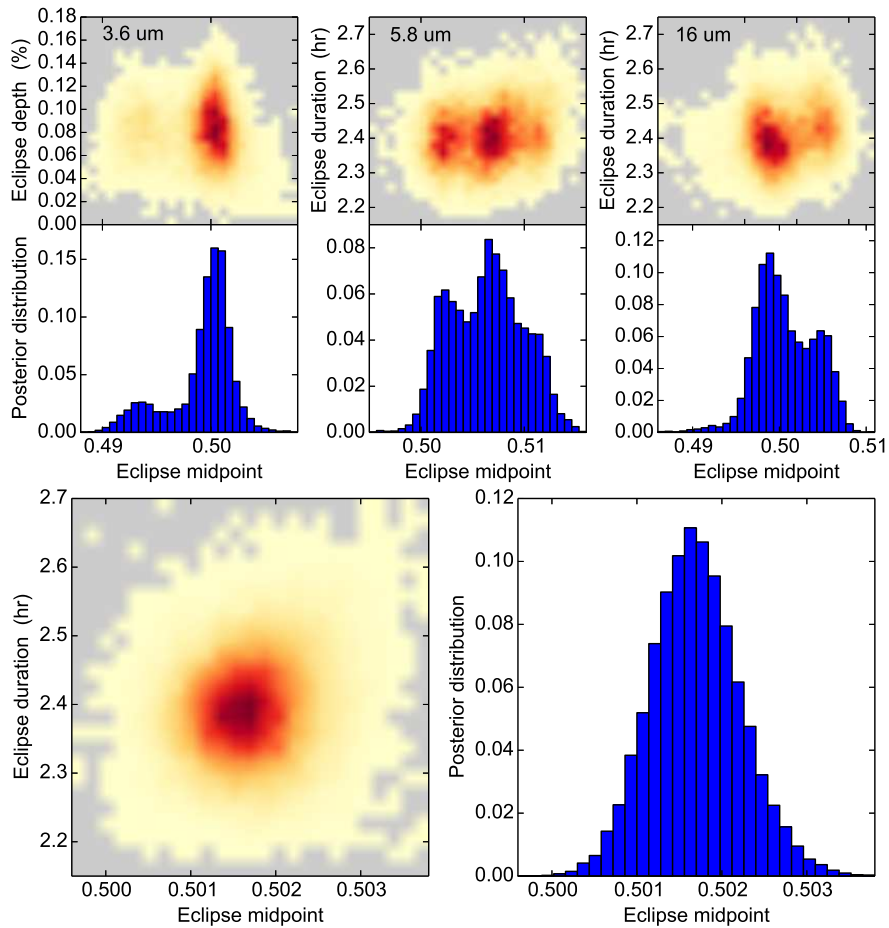


Figure 3.12: Eclipse-midpoint pairwise and marginal posteriors. **Top:** Independently-fit posterior eclipse depth or duration *vs.* midpoint for (left to right) 3.6, 5.8, and 16.0 μm . The multi-modality did not replicate for the eclipse depth (same eclipse depth for each of the posterior modes). **Bottom:** Eclipse-duration *vs.* midpoint pairwise (left) and midpoint marginal (right) posterior distributions for the fit with shared midpoint.

3.4.5.8 4.5 and 8.0 μm Eclipse Reanalyses

Our current analysis methods differ considerably from those of nearly a decade ago, with better centering, subpixel aperture photometry, BLISS mapping, simultaneous fits across multiple data sets, and evaluation of multiple models using BIC. Furthermore, MCMC techniques were not yet prominent in most exoplanet analyses, among other improvements. Charbonneau et al. (2005) used two field stars (with similar magnitudes to TrES-1) as flux calibrators. They extracted light curves using aperture photometry with an optimal aperture of 4.0 pixels, based on the rms of the calibrators' flux. At 4.5 μm , they decorrelated the flux from the telescope pointing, but gave no details. At 8.0 μm , they fit a third-order polynomial to the calibrators to estimate the ramp. Their eclipse model had two free parameters (depth and midpoint), which they fit by mapping χ^2 over a phase-space grid. Table 3.12 compares their eclipse depths with ours, showing a marginal 1σ difference at 4.5 μm . In both channels our MCMC found larger eclipse-depth uncertainties compared to those of Charbonneau et al. (2005), who calculated them from the χ^2 contour in the phase-space grid. The introduction of MCMC techniques and the further use of more efficient algorithms (e.g., differential-evolution MCMC) that converge faster enabled better error estimates. In the past, for example, a highly-correlated posterior prevented the MCMC convergence of some nuisance (systematics) parameters. The non-convergence forced one to fix these parameters to their best-fitting values. In current analyses, however, marginalization over nuisance parameters often leads to larger but more realistic error estimates.

Table 3.12: Eclipse-depth Reanalysis

Eclipse depth (%)	4.5 μm	8.0 μm
Charbonneau et al. (2005)	0.066(13)	0.225(36)
This work	0.094(24)	0.213(42)

The muxbleed correction was likely less accurately made than required for atmospheric characterization, given the presence of a visible muxbleed trail in the background near the star. We cannot easily assess either the uncertainty or the systematic offset added by the muxbleed and its correction, given, e.g., that the peak pixel flux varies significantly with small image motions. Our stated 4.5 μm uncertainty contains no additional adjustment for this unquantified noise source, which makes further use of the 4.5 μm eclipse depth difficult. However, our minimizer and the χ^2 map of Charbonneau et al. clearly find the eclipse, so the timing and duration appear less affected than the depth. In the analyses below, we include fits both with and without this dataset. The large uncertainty found by MCMC limits the 4.5 μm point's influence in the atmospheric fit.

3.5 Orbital Dynamics

As a preliminary analysis, we derived $e \cos(\omega)$ from the eclipse data alone. Our seven eclipse midpoint times straddle phase 0.5. After subtracting a light-time correction of $2a/c = 39$ seconds, where a is the semimajor axis and c is the speed of light, we found an eclipse phase of 0.5015 ± 0.0006 . This implies a marginal non-zero value for $e \cos(\omega)$ of 0.0023 ± 0.0009 (under the small-eccentricity approximation, Charbonneau et al. 2005).

It is possible that a non-uniform brightness emission from the planet can lead to non-zero measured eccentricity (Williams et al. 2006). For example, a hotspot eastward from the substellar point can simulate a late occultation ingress and egress compared to the uniform-brightness case. However, as pointed out by (de Wit et al. 2012), to constrain the planetary brightness distribution requires a higher photometric precision than what TrES-1 can provide.

Further, using the MCMC routine described by Campo et al. (2011), we fit a Keplerian-orbit model to our secondary-eclipse midpoints simultaneously with 33 radial-velocity (Table 3.15) and 84 transit data points (Table 3.16). We discarded nine radial-velocity points that were affected by the Rossiter-McLaughlin effect. We were able to constrain $e \cos(\omega)$ to 0.0017 ± 0.0003 . Although this 3σ result may suggest a non-circular orbit, when combined with the fit to $e \sin(\omega)$ of -0.033 ± 0.025 , the posterior distribution for the eccentricity only indicates a marginally eccentric orbit with $e = 0.033^{+0.015}_{-0.031}$. Table 3.13 summarizes our orbital MCMC results.

Table 3.13: MCMC Eccentric Orbital Model

Parameter	Best-fitting Value
$e \sin \omega$	-0.033 ± 0.025
$e \cos \omega$	0.0017 ± 0.0003
e	$0.033^{+0.015}_{-0.031}$
ω ($^\circ$)	$273^{+1.4}_{-2.8}$
Orbital period (days)	$3.0300699 \pm 1 \times 10^{-7}$
Transit time, T_0 (MJD) ^a	3186.80692 ± 0.00005
RV semiamplitude, K (m s^{-1})	115.5 ± 3.6
system RV, γ (m s^{-1})	-3.9 ± 1.3
Reduced χ^2	6.2

Note. ^a MJD = BJD_{TDB} - 2,450,000.

3.6 Atmosphere

We modeled the day-side emergent spectrum of TrES-1 with the retrieval method of Madhusudan & Seager (2009) to constrain the atmospheric properties of the planet. The code solves the plane-parallel, line-by-line, radiative transfer equations subjected to hydrostatic equilibrium, local thermodynamic equilibrium, and global energy balance. The code includes the main sources of opacity for hot Jupiters: molecular absorption from H₂O, CH₄, CO, and CO₂ (Freedman et al. 2008, Freedman, personal communication 2009), and H₂-H₂ collision induced absorption (Borysow 2002). We assumed a Kurucz stellar spectral model (Castelli & Kurucz 2004).

The model's atmospheric temperature profile and molecular abundances of H₂O, CO, CH₄, and CO₂ are free parameters, with the abundance parameters scaling initial profiles that are in thermochemical equilibrium. The output spectrum is integrated over the *Spitzer* bands and compared to the observed eclipse depths by means of χ^2 . An MCMC module supplies millions of parameter sets to the radiative transfer code to explore the phase space (Madhusudhan & Seager 2010, 2011).

Even though the features of each molecule are specific to certain wavelengths (Madhusudhan & Seager 2010), our independent observations (4 or 5) are less than the number of free parameters (10), and thus the model fitting is a degenerate problem. Thus, we stress that our goal is not to reach a unique solution, but to discard and/or constrain regions of the parameter phase space given the observations, as has been done in the past (e.g., Barman et al. 2005, Burrows et al. 2007, Knutson et al. 2008, Madhusudhan & Seager 2009, Stevenson et al. 2010, Madhusudhan et al. 2011).

Figure 3.13 shows the TrES-1 data points and model spectra of its day-side emission. An isothermal model can fit the observations reasonably well, as shown by the black dashed line (blackbody spectrum with a temperature of 1200 K). However, given the low S/N of the data, we cannot rule out non-inverted nor strong thermal-inversion models (with solar abundance composition in chemical equilibrium), as both can fit the data equally well (green and red models). Generally speaking, the data allow for efficient day-night heat redistribution; the models shown have maximum possible heat redistributions of 60% (non-inversion model) and 40% (inversion model).

As shown in Fig. 3.13, the data sets with and without the 4.5 μm point are nearly identical. Combined with the large error bars (especially at 16 μm), there is no significant difference between the atmospheric model results of the two cases. Both CO and CO₂ are dominant absorbers at 4.5 μm . Combined with the 16- μm detection, which is mainly sensitive to CO₂, the data could constrain the abundances of CO and CO₂. Unfortunately, the error bar on the 16 μm band is too large to derive any meaningful constraint.

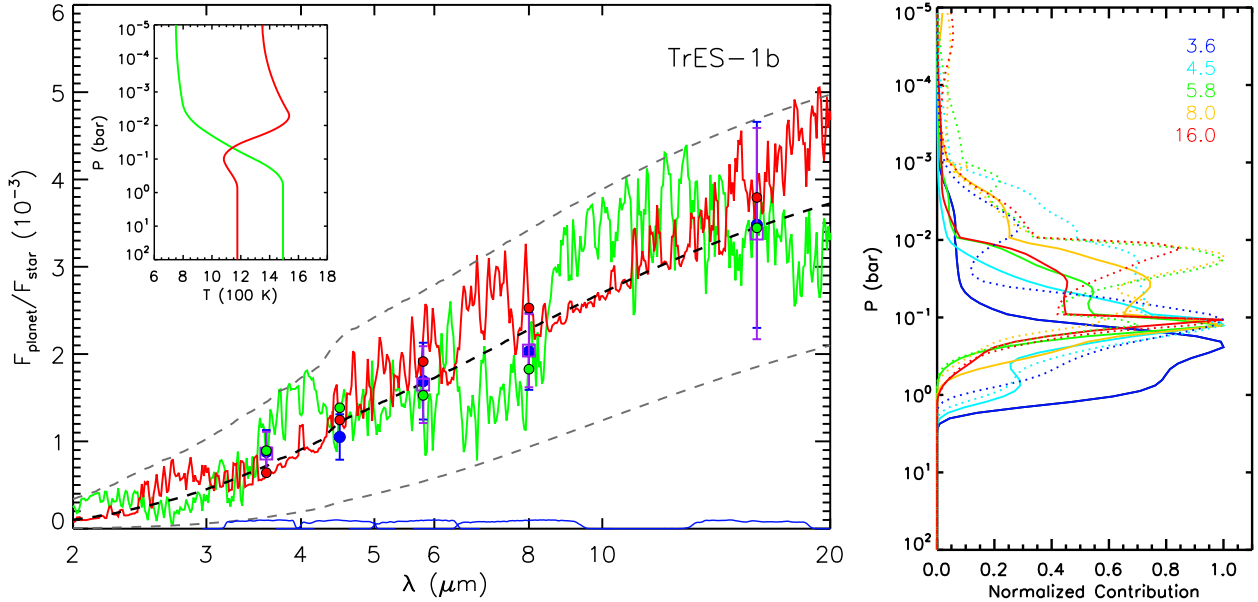


Figure 3.13: **Left:** Dayside atmospheric spectral emission of TrES-1. The blue circles and purple squares with error bars are the measured eclipse depths (including and excluding the 4.5 μm data point, respectively). The red and green curves show representative model spectra with and without thermal inversion (see inset), based on the data including the 4.5 μm point. Results omitting this point are similar. Both models have a solar abundance atomic composition and are in chemical equilibrium for the corresponding temperature profiles. The red and green circles give the band-integrated (bottom curves) fluxes of the corresponding models, for comparison to data. The dashed lines represent planetary blackbody spectra with $T = 800, 1200,$ and 1500 K. **Right:** Normalized contribution functions of the models over each *Spitzer* band (see legend). The dotted and solid lines are for the models with and without thermal inversion, respectively.

3.7 Conclusions

We have analyzed all the *Spitzer* archival data for TrES-1, comprising eclipses in five different bands (IRAC and IRS blue peak-up) and one IRS transit. There has been tremendous improvement in data-analysis techniques for *Spitzer*, and exoplanet light curves in general, since Charbonneau et al. (2005), one of the first two reported exoplanet secondary eclipses. A careful look at the 4.5 μm data frames revealed pixels affected by muxbleed that, although corrected by the *Spitzer* pipeline, still showed a clear offset output level. Unable to know the effect on the eclipse depth

and uncertainty, we conducted subsequent modeling both with and without the 4.5 μm point. The already-large uncertainty resulted in similar conclusions either way. Without adjusting our point for either the systematic or random effects of the muxbleed correction, the depth and uncertainty at 4.5 μm are both substantially larger than the original analysis. However, at 8.0 μm (which does not have similar problems) the eclipse depths are consistent, with our MCMC giving a larger uncertainty.

Our measured eclipse depths from our joint light-curve fitting (with and without the 4.5 μm point) are consistent with a nearly-isothermal atmospheric dayside emission at ~ 1200 K. This is consistent with the expected equilibrium temperature of 1150 K (assuming zero albedo and efficient energy redistribution). Furthermore, neither inverted nor non-inverted atmospheric models can be ruled out, given the low S/N of the data. Our transit analysis unfortunately does not improve the estimate of the planet-to-star radius ratio ($R_p/R_\star = 0.119 \pm 0.009$). Our comprehensive orbital analysis of the available eclipse, transit, and radial-velocity data indicates an eccentricity of $e = 0.034^{+0.014}_{-0.032}$, consistent with a circular orbit at the 1σ -level. Longitudinal variations in the planet's emission can induce time offsets in eclipse light curves, and could mimic non-zero eccentricities (e.g., Williams et al. 2006, de Wit et al. 2012). However, the S/N required to lay such constraints are much higher than that of the TrES-1 eclipse data.

We also described the latest improvements of our POET pipeline. Optimal photometry provides an alternative to aperture photometry. We first applied optimal photometry in Stevenson et al. (2010), but describe it in more detail here. Furthermore, the Differential-Evolution Markov-chain algorithm poses an advantage over a Metropolis Random Walk MCMC, since it automatically tunes the scale and orientation of the proposal distribution jumps. This dramatically increases the algorithm's efficiency, converging nearly ten times faster. We also now avoid the need to orthogonalize highly correlated posterior distributions.

3.8 Acknowledgements

We thank D. Charbonneau for sharing the original *Spitzer* pipeline data for the 4.5 and 8.0 μm bands and for helpful discussions. We thank the amateur observers from ETD, including Alfonso Carreño Garcerán, Zonalunar Observatory; Ferran Grau, Ca l’Ou observatory, Sant Mart’i Seseigüeles; Hana Kučáková, Altan Observatory, Czech Republic and Johann Palisa Observatory and Planetarium, Technical University Ostrava, Czech Republic; Prof. Dr. Johannes M. Ohlert; Christopher De Pree, Agnes Scott College and SARA; Peter Roomian, College of San Mateo Observatory; Stan Shadick, Physics and Engineering Physics Dept., University of Saskatchewan; Bradley Walter, Meyer Observatory, Central Texas Astronomical Society. Thanks Colo Colo for its Camp30n campaign. We thank contributors to SciPy, Matplotlib, and the Python Programming Language, the free and open-source community, the NASA Astrophysics Data System, and the JPL Solar System Dynamics group for software and services. PC is supported by the Fulbright Program for Foreign Students. This work is based on observations made with the *Spitzer Space Telescope*, which is operated by the Jet Propulsion Laboratory, California Institute of Technology under a contract with NASA. Support for this work was provided by NASA through an award issued by JPL/Caltech and through the NASA Science Mission Directorate’s Astrophysics Data Analysis Program, grant NNH12ZDA001N.

3.9 Joint Best Fit

Table 3.14 summarizes the model setting and results of the light-curve joint fit. The midpoint phase parameter was shared among the IRS eclipse observations.

Table 3.15 lists the aggregate TrES1 radial-velocity measurements.

Table 3.16 lists the aggregate TrES1 transit-midpoint measurements.

Table 3.14: Best-Fit Eclipse Light Curve Parameters

Parameter	tr001bs11	tr001bs21 ^a	tr001bs31	tr001bs41	tr001bs51	tr001bs52	tr001bs53	tr001bp51
Centering algorithm	Gauss fit	Center of Light	Least Asymmetry	Least Asymmetry	PSF fit	PSF fit	PSF fit	Gauss fit
Mean x position (pix)	119.95	169.02	113.74	167.92
Mean y position (pix)	82.58	118.63	83.29	117.62
x -position consistency ^b (pix)	0.014	0.019	0.021	0.019	0.038	0.036	0.040	0.045
y -position consistency ^b (pix)	0.026	0.025	0.024	0.030	0.044	0.036	0.043	0.037
Optimal/Aperture photometry size (pix)	2.50	3.75	2.75	2.75	optimal	optimal	optimal	1.5
Inner sky annulus (pix)	7.0	7.0	7.0	7.0	5.0	5.0	5.0	5.0
Outer sky annulus (pix)	15.0	15.0	15.0	15.0	10.0	10.0	10.0	10.0
BLISS mapping	Yes	Yes	No	No	No	No	No	No
Minimum Points Per Bin	4	4
System flux F_s (μ Jy)	33191.4(5.9)	21787.0(2.3)	14184.5(3.3)	8440.7(2.3)	1792.3(2.1)	1797.2(2.3)	1796.6(2.3)	857(1.8)
Eclipse depth (%)	0.083(24)	0.094(24)	0.162(42)	0.213(42)	0.33(12)	0.33(12)	0.33(12)	...
Brightness temperature (K)	1270(110)	1126(90)	1205(130)	1190(130)	1270(310)	1270(310)	1270(310)	...
Eclipse midpoint (orbital phase)	0.5015(5)	0.5015(5)	0.5015(5)	0.5015(5)	0.5015(5)	0.5015(5)	0.5015(5)	...
Eclipse/Transit midpoint (MJD _{UTC}) ^c	3630.7152(16)	3309.5283(16)	3630.7152(16)	3309.5283(16)	3873.1204(16)	3876.1504(16)	3879.1805(16)	3871.5998(38)
Eclipse/Transit midpoint (MJD _{TDB}) ^c	3630.7159(16)	3309.5290(16)	3630.7159(16)	3309.5290(16)	3873.1211(16)	3876.1512(16)	3879.1812(16)	3871.6005(38)
Eclipse/Transit duration (t_{4-1} , hrs)	2.39(7)	2.39(7)	2.39(7)	2.39(7)	2.39(7)	2.39(7)	2.39(7)	2.496(33)
Ingress/egress time (t_{2-1} , hrs)	0.31(1)	0.31(1)	0.31(1)	0.31(1)	0.31(1)	0.31(1)	0.31(1)	0.28(2)
R_p/R_*	0.1295(95)
$\cos(i)$	$0.0^{+0.000008}_{-0.0}$
a/R_*	$10.494^{+0.092}_{-0.135}$
Limb darkening coefficient, c_2	0.75(22)
Limb darkening coefficient, c_2	-0.19(11)
Ramp equation ($R(t)$)	$A(a)$	None	None	linramp	linramp	linramp	linramp	linramp
Ramp, linear term (r_1)	0.2455(82)	0.182(49)	0.151(42)	0.118(47)	0.063(17)
AOR scaling factor ($A(a_2)$)	1.00234(33)
Number of free parameters ^d	6	5	5	6	6	6	6	8
Total number of frames	3904	1518	1952	1518	500	500	500	500
Frames used ^e	3827	1407	1763	1482	460	500	500	492
Rejected frames (%)	1.97	7.31	9.68	2.37	8.0	0.0	0.0	1.6
BIC value	10103.0	10103.0	10103.0	10103.0	10103.0	10103.0	10103.0	533.4
SDNR	0.0053766	0.0026650	0.0083273	0.0074324	0.0223287	0.0233603	0.0233306	0.0248263
Uncertainty scaling factor	0.946	1.065	1.186	0.962	0.543	0.574	0.590	0.489
Photon-limited S/N (%)	99.34	89.67	74.04	63.01	8.34	7.98	7.99	10.7

Notes.
^a Data corrupted by muxbleed.

^b rms frame-to-frame position difference.

^c MJD = BJD - 2,450,000.

^d In the individual fits.

^e We exclude frames during instrument/telescope settling, for insufficient points at a given BLISS bin, and for bad pixels in the photometry aperture.

Table 3.15: TrES-1 Radial-velocity Data

Date BJD(TDB) – 2450000.0	RV (m s^{-1})	Reference
3191.77001	60.4 ± 12.8	1
3192.01201	115.1 ± 8.3	1
3206.89101	87.1 ± 16.0	1
3207.92601	15.8 ± 10.4	1
3208.73001	-113.3 ± 15.0	1
3208.91701	-98.1 ± 19.8	1
3209.01801	-118.4 ± 15.3	1
3209.73101	49.8 ± 15.7	1
3237.97926	68.32 ± 3.66	2
3238.83934	-102.23 ± 3.27	2
3239.77361	-24.53 ± 3.25	2
3239.88499	10.00 ± 3.11	2
3240.97686	70.68 ± 3.73	2
3907.87017	18.7 ± 14.0	3
3907.88138	30.5 ± 12.5	3
3907.89261	54.6 ± 12.0	3
3907.90383	24.3 ± 10.4	3
3907.91505 ^a	26.4 ± 11.4	3
3907.92627 ^a	30.4 ± 10.9	3
3907.93749 ^a	22.4 ± 14.3	3
3907.94872 ^a	2.9 ± 11.0	3
3907.95995 ^a	-7.1 ± 12.1	3
3907.97118 ^a	-22.3 ± 13.3	3
3907.98240 ^a	-40.5 ± 13.3	3
3907.99363 ^a	-39.2 ± 13.0	3
3908.00487 ^a	-9.8 ± 12.2	3
3908.01609 ^a	-30.5 ± 13.8	3
3908.02731	-17.7 ± 13.6	3
3908.03853	-24.7 ± 12.2	3
3908.04977	-27.5 ± 11.1	3
3908.06099	-38.2 ± 13.3	3
3908.07222	-23.7 ± 11.2	3
3908.08344	-23.0 ± 9.6	3

Note.

^a Discarded due to Rossiter-McLaughlin effect.

References. (1) Alonso et al. 2004; (2) Laughlin et al. 2005; (3) Narita et al. 2007.

Table 3.16: TrES-1 Transit Midpoint Data

Midtransit Date BJD(TDB) – 2450000.0	Error	Source ^a
6253.23986	0.00105	ETD: Sokov E. N.
6198.69642	0.00119	ETD: Roomian P.
6198.69600	0.00056	ETD: Shadic S.
6177.47937	0.00099	ETD: Emering F.
6168.39577	0.00042	ETD: Mravik J., Grnja J.
6107.79376	0.00032	ETD: Shadic S.
6074.46334	0.00117	ETD: Bachschmidt M.
6074.46253	0.00112	ETD: Emering F.
6071.43377	0.00055	ETD: Carreño
6071.43165	0.00072	ETD: Gaitan J.
6071.43099	0.0007	ETD: Horta F. G.
5886.59953	0.00048	ETD: Shadic S.
5801.75506	0.0004	ETD: Shadic S.
5798.73056	0.00049	ETD: Shadic S.
5795.69991	0.00053	ETD: Walter B., Strickland W., Soriano R.
5795.69903	0.00064	ETD: Walter B., Strickland W., Soriano R.
5795.69797	0.00055	ETD: Walter B., Strickland W., Soriano R.
5777.51807	0.00056	ETD: Centenera F.
5768.42617	0.00042	ETD: V. Krushevska, Yu. Kuznietsova, M. Andreev
5765.39585	0.0004	ETD: V. Krushevska, Yu. Kuznietsova, M. Andreev
5762.36407	0.00037	ETD: V. Krushevska, Yu. Kuznietsova, M. Andreev
5759.33530	0.00049	ETD: V. Krushevska, Yu. Kuznietsova, M. Andreev
5707.81338	0.00093	ETD: Marlowe H., Makely N., Hutcheson M., DePree C.
5680.55402	0.00064	ETD: Sergison D.
5671.46700	0.00114	ETD: Kučáková H.
5671.46384	0.00088	ETD: Vrašťák M.
5671.46382	0.0009	ETD: Brát L.
5371.48766	0.00074	ETD: Mihelčič M.
5304.82572	0.00084	ETD: Shadick S.
5095.75034	0.00075	ETD: Rozema G.
5089.69043	0.00109	ETD: Vander Haagen G.
5068.48006	0.00062	ETD: Trnka J.
5062.42088	0.00053	ETD: Sauer T.
5062.42078	0.00046	ETD: Trnka J., Klos M.
5062.42012	0.00046	ETD: Dřevěný R., Kalisch T.
5062.41959	0.0006	ETD: Brát L.
5062.41797	0.00102	ETD: Kučáková H., Speil J.
4998.79649	0.0016	ETD: Garlitz
4971.51779	0.001	ETD: Gregorio
4968.48904	0.00192	ETD: Příb'ík V.
4968.48811	0.00053	ETD: Trnka J.
4968.48753	0.00028	ETD: Andreev M., Kuznietsova Y., Krushevska V.
4671.54149	0.0021	ETD: Mendez
4662.44989	0.001	ETD: Forne
4383.68459	0.0019	ETD: Sheridan
4380.65579	0.0014	ETD: Sheridan

Table 3.16: TrES-1 Transit Midpoint Data — (Continued)

Midtransit Date BJD(TDB) – 2450000.0	Error	Source ^a
4362.47423	0.0002	Hrudková et al. (2009)
4359.44430	0.00015	Hrudková et al. (2009)
4356.41416	0.0001	Hrudková et al. (2009)
4356.41324	0.00096	ETD: Andreev M., Kuznietsova Y., Krushevska V.
4350.35296	0.00036	ETD: Andreev M., Kuznietsova Y., Krushevska V.
4347.32322	0.00028	ETD: Andreev M., Kuznietsova Y., Krushevska V.
3907.96406	0.00034	Narita et al. (2007)
3901.90372	0.00019	Winn et al. (2007)
3901.90371	0.0016	Narita et al. (2007)
3898.87342	0.00014	Narita et al. (2007)
3898.87341	0.00014	Winn et al. (2007)
3898.87336	0.00008	Winn et al. (2007)
3895.84298	0.00015	Narita et al. (2007)
3895.84297	0.00018	Winn et al. (2007)
3856.45180	0.0005	ETD: Hentunen
3650.40752	0.00045	ETD: NYX
3550.41568	0.0003	ETD: NYX
3547.38470	0.0012	ETD: NYX
3256.49887	0.00044	ETD: Ohlert J.
3253.46852	0.00057	ETD: Pejcha
3253.46812	0.00038	ETD: Ohlert J.
3247.40751	0.0004	Charbonneau et al. (2005)
3189.83541	0.0019	Charbonneau et al. (2005)
3186.80626	0.00054	Alonso et al. (2004)
3186.80611	0.0003	Charbonneau et al. (2005)
3183.77521	0.0005	Charbonneau et al. (2005)
3174.68641	0.0004	Charbonneau et al. (2005)
2868.65031	0.0022	Charbonneau et al. (2005)
2856.52861	0.0015	Charbonneau et al. (2005)
2847.43631	0.0015	Charbonneau et al. (2005)
2850.47091	0.0016	Charbonneau et al. (2005)
3171.65231	0.0019	Charbonneau et al. (2005)
3192.86941	0.0015	Charbonneau et al. (2005)
3180.75291	0.0010	Charbonneau et al. (2005)
4356.41492	0.00010	Hrudková et al. (2009)
4359.44506	0.00015	Hrudková et al. (2009)
4362.47499	0.00020	Hrudková et al. (2009)

Note. ^a ETD: amateur transits from the Exoplanet Transit Database (<http://var2.astro.cz/ETD/index.php>) with reported error bars and quality indicator of 3 or better.

3.10 Light Curve Data Sets

All the light curve data sets are available in Flexible Image Transport System (FITS) format in a tar.gz package in the electronic edition.

3.11 List of References

Adams, E. R., Dupree, A. K., Kulesa, C., & McCarthy, D. 2013, ArXiv e-prints

Alonso, R., Brown, T. M., Torres, G., Latham, D. W., Sozzetti, A., Mandushev, G., Belmonte, J. A., Charbonneau, D., Deeg, H. J., Dunham, E. W., O'Donovan, F. T., & Stefanik, R. P. 2004, *ApJ*, 613, L153

Barman, T. S., Hauschildt, P. H., & Allard, F. 2005, *ApJ*, 632, 1132

Blecic, J., Harrington, J., Madhusudhan, N., Stevenson, K. B., Hardy, R. A., Cubillos, P. E., Hardin, M., Campo, C. J., Bowman, W. C., Nymeyer, S., Loredo, T. J., Anderson, D. R., & Maxted, P. F. L. 2013, *ApJ*, 779, 5

Borysow, A. 2002, *A&A*, 390, 779

Burrows, A., Hubeny, I., Budaj, J., Knutson, H. A., & Charbonneau, D. 2007, *ApJ*, 668, L171

Butler, R. P., Wright, J. T., Marcy, G. W., Fischer, D. A., Vogt, S. S., Tinney, C. G., Jones, H. R. A., Carter, B. D., Johnson, J. A., McCarthy, C., & Penny, A. J. 2006, *ApJ*, 646, 505

Campo, C. J., Harrington, J., Hardy, R. A., Stevenson, K. B., Nymeyer, S., Ragozzine, D., Lust, N. B., Anderson, D. R., Collier-Cameron, A., Blecic, J., Britt, C. B. T., Bowman, W. C., Wheatley, P. J., Loredo, T. J., Deming, D., Hebb, L., Hellier, C., Maxted, P. F. L., Pollaco, D., & West, R. G. 2011, *ApJ*, 727, 125

- Castelli, F. & Kurucz, R. L. 2004, ArXiv Astrophysics e-prints
- Charbonneau, D., Allen, L. E., Megeath, S. T., Torres, G., Alonso, R., Brown, T. M., Gilliland, R. L., Latham, D. W., Mandushev, G., O'Donovan, F. T., & Sozzetti, A. 2005, ApJ, 626, 523
- Charbonneau, D., Brown, T. M., Burrows, A., & Laughlin, G. 2007, Protostars and Planets V, 701
- Cubillos, P., Harrington, J., Madhusudhan, N., Stevenson, K., Hardy, R., Blečić, J., Anderson, D., Hardin, M., & Campo, C. 2013, ApJ, Submitted
- de Wit, J., Gillon, M., Demory, B.-O., & Seager, S. 2012, A&A, 548, A128
- Deming, D., Seager, S., Richardson, L. J., & Harrington, J. 2005, Nature, 434, 740
- Eastman, J., Gaudi, B. S., & Agol, E. 2013, PASP, 125, 83
- Fazio, G. G., Hora, J. L., Allen, L. E., Ashby, M. L. N., Barmby, P., Deutsch, L. K., Huang, J.-S., Kleiner, S., Marengo, M., Megeath, S. T., Melnick, G. J., Pahre, M. A., Patten, B. M., Polizotti, J., Smith, H. A., Taylor, R. S., Wang, Z., Willner, S. P., Hoffmann, W. F., Pipher, J. L., Forrest, W. J., McMurty, C. W., McCreight, C. R., McKelvey, M. E., McMurray, R. E., Koch, D. G., Moseley, S. H., Arendt, R. G., Mentzell, J. E., Marx, C. T., Losch, P., Mayman, P., Eichhorn, W., Krebs, D., Jhabvala, M., Gezari, D. Y., Fixsen, D. J., Flores, J., Shakoorzadeh, K., Jungo, R., Hakun, C., Workman, L., Karpati, G., Kichak, R., Whitley, R., Mann, S., Tollestrup, E. V., Eisenhardt, P., Stern, D., Gorjian, V., Bhattacharya, B., Carey, S., Nelson, B. O., Glaccum, W. J., Lacy, M., Lowrance, P. J., Laine, S., Reach, W. T., Stauffer, J. A., Surace, J. A., Wilson, G., Wright, E. L., Hoffman, A., Domingo, G., & Cohen, M. 2004, ApJS, 154, 10
- Freedman, R. S., Marley, M. S., & Lodders, K. 2008, ApJS, 174, 504
- Gelman, A. & Rubin, D. B. 1992, Statistical Science, 7, 457
- Gibson, N. P. 2014, ArXiv e-prints

- Gregory, P. 2005, *Bayesian Logical Data Analysis for the Physical Sciences* (New York, NY, USA: Cambridge University Press)
- Harrington, J. & French, R. G. 2010, *ApJ*, 716, 398
- Harrington, J., Luszcz, S., Seager, S., Deming, D., & Richardson, L. J. 2007, *Nature*, 447, 691
- Horne, K. 1986, *PASP*, 98, 609
- Hrudková, M., Skillen, I., Benn, C., Pollacco, D., Gibson, N., Joshi, Y., Harmanec, P., & Tulloch, S. 2009, in *IAU Symposium*, Vol. 253, *IAU Symposium*, ed. F. Pont, D. Sasselov, & M. J. Holman, 446–449
- Knutson, H. A., Charbonneau, D., Allen, L. E., Burrows, A., & Megeath, S. T. 2008, *ApJ*, 673, 526
- Knutson, H. A., Charbonneau, D., Deming, D., & Richardson, L. J. 2007, *PASP*, 119, 616
- Knutson, H. A., Madhusudhan, N., Cowan, N. B., Christiansen, J. L., Agol, E., Deming, D., Désert, J.-M., Charbonneau, D., Henry, G. W., Homeier, D., Langton, J., Laughlin, G., & Seager, S. 2011, *ApJ*, 735, 27
- Laughlin, G., Wolf, A., Vanmunster, T., Bodenheimer, P., Fischer, D., Marcy, G., Butler, P., & Vogt, S. 2005, *ApJ*, 621, 1072
- Levenberg, K. 1944, *Quart. Applied Math.*, 2, 164
- Liddle, A. R. 2007, *MNRAS*, 377, L74
- Madhusudhan, N., Harrington, J., Stevenson, K. B., Nymeyer, S., Campo, C. J., Wheatley, P. J., Deming, D., Blečić, J., Hardy, R. A., Lust, N. B., Anderson, D. R., Collier-Cameron, A., Britt, C. B. T., Bowman, W. C., Hebb, L., Hellier, C., Maxted, P. F. L., Pollacco, D., & West, R. G. 2011, *Nature*, 469, 64

- Madhusudhan, N. & Seager, S. 2009, *ApJ*, 707, 24
- . 2010, *ApJ*, 725, 261
- . 2011, *ApJ*, 729, 41
- Mandel, K. & Agol, E. 2002, *ApJ*, 580, L171
- Marquardt, D. W. 1963, *SIAM Journal on Applied Mathematics*, 11, 431
- Narita, N., Enya, K., Sato, B., Ohta, Y., Winn, J. N., Suto, Y., Taruya, A., Turner, E. L., Aoki, W., Yoshii, M., Yamada, T., & Tamura, Y. 2007, *PASJ*, 59, 763
- Nymeyer, S., Harrington, J., Hardy, R. A., Stevenson, K. B., Campo, C. J., Madhusudhan, N., Collier-Cameron, A., Lored, T. J., Blečić, J., Bowman, W. C., Britt, C. B. T., Cubillos, P., Hellier, C., Gillon, M., Maxted, P. F. L., Hebb, L., Wheatley, P. J., Pollacco, D., & Anderson, D. R. 2011, *ApJ*, 742, 35
- Pont, F., Zucker, S., & Queloz, D. 2006, *MNRAS*, 373, 231
- Rabus, M., Deeg, H. J., Alonso, R., Belmonte, J. A., & Almenara, J. M. 2009, *A&A*, 508, 1011
- Raetz, S., Mugrauer, M., Schmidt, T. O. B., Roell, T., Eisenbeiss, T., Hohle, M. M., Tetzlaff, N., Vaňko, M., Seifahrt, A., Broeg, C., Koppenhoefer, J., & Neuhäuser, R. 2009, *Astronomische Nachrichten*, 330, 475
- Raftery, A. E. 1995, *Sociological Methodology*, 25, 111
- Reach, W. T., Megeath, S. T., Cohen, M., Hora, J., Carey, S., Surace, J., Willner, S. P., Barmby, P., Wilson, G., Glaccum, W., Lowrance, P., Marengo, M., & Fazio, G. G. 2005, *PASP*, 117, 978
- Roberts, G., Gelman, A., & Gilks, W. 1997, *Annals of Applied Probability*, 7, 110

Sada, P. V., Deming, D., Jennings, D. E., Jackson, B. K., Hamilton, C. M., Fraine, J., Peterson, S. W., Haase, F., Bays, K., Lunsford, A., & O’Gorman, E. 2012, *PASP*, 124, 212

Santos, N. C., Ecuivillon, A., Israelian, G., Mayor, M., Melo, C., Queloz, D., Udry, S., Ribeiro, J. P., & Jorge, S. 2006a, *A&A*, 458, 997

Santos, N. C., Pont, F., Melo, C., Israelian, G., Bouchy, F., Mayor, M., Moutou, C., Queloz, D., Udry, S., & Guillot, T. 2006b, *A&A*, 450, 825

Seager, S. & Deming, D. 2010, *ARA&A*, 48, 631

Southworth, J. 2008, *MNRAS*, 386, 1644

—. 2009, *MNRAS*, 394, 272

Sozzetti, A., Yong, D., Carney, B. W., Laird, J. B., Latham, D. W., & Torres, G. 2006, *AJ*, 131, 2274

Steffen, J. H. & Agol, E. 2005, *MNRAS*, 364, L96

Stevenson, K. B., Harrington, J., Fortney, J. J., Lored, T. J., Hardy, R. A., Nymeyer, S., Bowman, W. C., Cubillos, P., Bowman, M. O., & Hardin, M. 2012a, *ApJ*, 754, 136

Stevenson, K. B., Harrington, J., Lust, N. B., Lewis, N. K., Montagnier, G., Moses, J. I., Visscher, C., Blecic, J., Hardy, R. A., Cubillos, P., & Campo, C. J. 2012b, *ApJ*, 755, 9

Stevenson, K. B., Harrington, J., Nymeyer, S., Madhusudhan, N., Seager, S., Bowman, W. C., Hardy, R. A., Deming, D., Rauscher, E., & Lust, N. B. 2010, *Nature*, 464, 1161

ter Braak, C. 2006, *Statistics and Computing*, 16, 239, 10.1007/s11222-006-8769-1

Torres, G., Fischer, D. A., Sozzetti, A., Buchhave, L. A., Winn, J. N., Holman, M. J., & Carter, J. A. 2012, *ApJ*, 757, 161

Torres, G., Winn, J. N., & Holman, M. J. 2008, *ApJ*, 677, 1324

Vaňko, M., Raetz, S., Mugrauer, M., Schmidt, T. O. B., Roell, T., Eisenbeiss, T., Hohle, M., Seifahrt, A., Koeltzsch, A., Broeg, C., Koppenhoefer, J., & Neuhäuser, R. 2009, in *IAU Symposium*, Vol. 253, *IAU Symposium*, ed. F. Pont, D. Sasselov, & M. J. Holman, 440–442

Williams, P. K. G., Charbonneau, D., Cooper, C. S., Showman, A. P., & Fortney, J. J. 2006, *ApJ*, 649, 1020

Winn, J. N., Holman, M. J., & Roussanova, A. 2007, *ApJ*, 657, 1098

Winn, J. N., Holman, M. J., Torres, G., McCullough, P., Johns-Krull, C., Latham, D. W., Shporer, A., Mazeh, T., Garcia-Melendo, E., Foote, C., Esquerdo, G., & Everett, M. 2008, *ApJ*, 683, 1076

CHAPTER 4: ON CORRELATED-NOISE ANALYSES APPLIED TO EXOPLANET LIGHT CURVES

**Patricio Cubillos¹, Joseph Harrington¹, Thomas J. Loredo², Nate B. Lust¹, Jasmina Blečić¹,
and Madison M. Stemm¹**

*¹Planetary Sciences Group, Department of Physics, University of Central Florida, Orlando, FL
32816-2385, USA*

*²Center for Radiophysics and Space Research, Space Sciences Building, Cornell University, Ithaca,
NY 14853-6801, USA*

*In preparation for *The Astrophysical Journal*.*

4.1 Abstract

Time-correlated noise is a significant source of uncertainty when modeling exoplanet light-curve data. A correct assessment of the correlated noise is fundamental to determining the true statistical significance of our findings. In the field, the time-averaging, residual-permutation, and wavelet-based likelihood methods are three of the most widely used time-correlated noise estimators. Yet, there are few studies that investigate these methods quantitatively. We have reviewed these three techniques and evaluated their performance on the eclipse-depth estimation for synthetic exoplanet light-curve data. For the time-averaging method we found artifacts in the rms-vs.-bin-size curves that led to underestimated uncertainties. This is most noticeable when the time scale of the feature under study is a large fraction of the total observation time. We show that the residual-permutation method is unsound as a tool for estimating uncertainty in parameter estimates. For the wavelet-likelihood method, we noted errors in the published equations and provide a list of corrections. We further tested these techniques by injecting eclipse signals into a synthetic dataset and into a real Spitzer dataset, allowing us to assess the competence of the methods for data with controlled and real correlated noise, respectively. Both the time-averaging and wavelet-likelihood methods improved the estimate of the eclipse-depth uncertainty with respect to a white-noise analysis (a Markov-chain Monte Carlo exploration that assumes uncorrelated data errors). The time-averaging and wavelet-analysis methods estimated eclipse-depth errors within $\sim 20 - 50\%$ of the expected value. Lastly, we present our open-source model-fitting tool, Multi-Core Markov-Chain Monte Carlo (MC³). This module uses Bayesian statistics to estimate the best-fitting values and the credible region of the (user-provided) model fitting parameters. MC³ is a Python and C code, available to the community at <https://github.com/pcubillos/MCcubed>.

4.2 Introduction

Whether our goal is the detection or the characterization of exoplanets through transit or eclipse observations, the large contrast between the stellar and planetary emission (about a thousand times in the infrared) make the data analysis an intrinsically challenging task. For example, for the Spitzer Space Telescope, most planetary signals (e.g., Stevenson et al. 2010, Demory et al. 2012) lie below the instrument’s design criteria for photometric stability (Fazio et al. 2004). Extracting planetary signals at this precision requires meticulous data reduction. Despite our best attempts to account for all known systematics, time-correlated residuals (or red noise) between the data and models often remain. These systematics may originate from instrumental or astrophysical sources, for example: stellar flux variations from flares or granulation; imperfect flat fielding; or telluric variations from changing weather conditions, differential extinction, or imperfect telescope systematics corrections from changing telescope pointing. Many authors have acknowledged correlated noise as an important source of noise in time-series data sets (e.g., Pont et al. 2006, Winn et al. 2007, Agol et al. 2010, Cubillos et al. 2013).

Correlated noise affects both the accuracy and the precision of model parameters. The typical statistical analyses neglect the correlation between data points (e.g., likelihood functions based on uncorrelated noise). Hence, their estimated best-fitting values may be biased, whereas their credible regions (Appendix 4.8) are too small, because they do not account for correlated noise. This paper examines three correlated-noise estimators found in the exoplanet literature. First, the time-averaging method (Pont et al. 2006, Winn et al. 2007) compares the standard deviation of the data to the (expected) uncorrelated-noise standard deviation, scaling the uncertainties accordingly. Next, the residual-permutation (or “prayer bead”) method (Bouchy et al. 2005) uses a bootstrap

algorithm that preserves the structure of the residuals. Lastly, Carter & Winn (2009) calculated the likelihood function in a wavelet basis, where the correlation between the wavelet coefficients is negligible. Qualitatively speaking, these methods do return larger parameter uncertainties for stronger correlated noise. However, besides Carter & Winn (2009), there are few efforts to validate their quantitative accuracy.

We have implemented these methods, testing them with real and synthetic exoplanet eclipse data. We did not consider other correlated-noise modeling frameworks. We explicitly excluded Gaussian processes (Gibson et al. 2012) since this technique becomes computationally prohibitive for large datasets like the ones explored in this work (over ~ 1000 data points, Gibson 2014). With a focus on atmospheric characterization, we concentrated on estimating the depth of exoplanet light curves. The eclipse depth constrains the planet-to-star flux ratio, whereas the transit depth constrains the planet-to-star radius ratio (Seager & Deming 2010). Moreover, a multi-wavelength analysis of the depth samples the planetary spectrum (e.g., Madhusudhan & Seager 2009), constraining the atmospheric properties of the planet.

We focused on Spitzer observations, since they represent the largest and best-quality sample of exoplanet data beyond $2 \mu\text{m}$. Additionally, many of the Spitzer light curves show time-correlated noise. We simulated realistic Spitzer secondary-eclipse observations in terms of known systematics, signal-to-noise ratio (S/N), cadence, duration, and eclipse shape. Spitzer data are affected by two well-known systematics: time-varying sensitivity (ramp) and intra-pixel sensitivity variations (Knutson et al. 2009, Charbonneau et al. 2005). Although several models have been proposed to correct for these systematics (Harrington et al. 2007, Knutson et al. 2008, Ballard et al. 2010, Agol et al. 2010, Stevenson et al. 2012a, Lewis et al. 2013, Deming et al. 2014), the corrections are not always perfect, and thus many light-curve fits exhibit time-correlated residuals.

In Section 4.3, we summarize the model-fitting estimation problem and review the correlated-noise estimators. In Section 4.4, we test and compare the correlated-noise methods by retrieving injected synthetic eclipse curves into synthetic and real light-curve data. In Section 4.5 we present our open-source module, Multi-Core Markov-Chain Monte Carlo (MC³), to calculate the model-parameters' credible regions. Finally, in Section 4.6 we present our conclusions.

4.3 Model-Fitting Estimation

A meaningful model-fitting analysis consists of two fundamental tasks, estimating the model parameters' best-fitting values and estimating the credible region. In this section we provide a brief description of the model-fitting problem under the Bayesian-statistics perspective. For a more detailed discussion see, for example, Gregory (2005) and Sivia & Skilling (2006). The following subsections then describe three of the most common methods to account for correlated noise.

4.3.1 Overview

To determine the set of best-fitting values, \mathbf{x} , of a model, M , given a data set, \mathbf{D} , one maximizes the posterior probability distribution:

$$P(\mathbf{x}|\mathbf{D}, M) = P(\mathbf{x}|M)P(\mathbf{D}|\mathbf{x}, M), \quad (4.1)$$

where $P(\mathbf{x}|M)$ is the prior probability distribution and $P(\mathbf{D}|\mathbf{x}, M)$ is the likelihood function, $\mathcal{L}(\mathbf{x})$. In the most general case, the likelihood function is given by

$$\mathcal{L}(\mathbf{x}) = \frac{1}{(2\pi)^{N/2}|\Sigma|^{\frac{1}{2}}} \exp\left(-\frac{1}{2}\mathbf{r}^T\Sigma^{-1}\mathbf{r}\right), \quad (4.2)$$

where Σ is the data covariance matrix and $\mathbf{r} = \mathbf{r}(\mathbf{x})$ are the residuals between the data points and the model. If the data values are uncorrelated, the off-diagonal terms in the covariance matrix become negligible, and the likelihood function simplifies to:

$$\mathcal{L}(\mathbf{x}) = \prod_i \frac{1}{\sqrt{2\pi\sigma_i^2}} \exp\left(-\frac{r_i^2(\mathbf{x})}{2\sigma_i^2}\right), \quad (4.3)$$

with $\sigma_i^2 \equiv \Sigma_{ii}$ the variance of the data point i . When the data-point uncertainties are known, maximizing the likelihood function translates into minimizing chi squared, $\chi^2 = \sum (r_i/\sigma_i)^2$. The reduced chi squared, χ_{red}^2 (χ^2 divided by the number of degrees of freedom), is the ratio of the variance of the fit to the variance of the data (Bevington & Robinson 2003). Then, χ_{red}^2 serves as a measure of the goodness of fit; if the model is a good approximation of the observations, we expect $\chi_{\text{red}}^2 \approx 1$.

In the Bayesian framework, the credible region of the parameters can be estimated via the Markov-chain Monte Carlo (MCMC) algorithm. The MCMC method generates random samples from the parameter phase space with a probability density proportional to the posterior probability distribution, $P(\mathbf{x}|\mathbf{D}, M)$. The credible region for each parameter is then obtained from the interval that contains a certain fraction of the highest posterior density (typically 68%, 95%, or 99%) of the marginalized posterior (see Appendix 4.8). For example, when the posterior follows a normal distribution, the 68.3% credible interval corresponds to the interval contained within 1 standard deviation from the mean.

The data uncertainties, σ_i , determine the span of the sampled distribution: the smaller the uncertainties, the more concentrated are the marginal posterior distributions. If there is no information on the data uncertainties, one might adopt a uniform uncertainty value for every data point. If the uncertainties of a time-series data set are known to be under- (or over-) estimated ($\chi_{\text{red}}^2 \neq 1$), one often scales them:

$$\sigma'_i = \sqrt{\chi_{\text{red}}^2} \sigma_i. \quad (4.4)$$

An MCMC guided by Equation (4.3) works well when the data points are independent and identically distributed; however, it does not account for time-correlated noise. Alternatively, an MCMC that uses the full covariance matrix of Equation (4.2) should account for correlated noise, although its calculation often becomes computationally prohibitive.

4.3.2 Time Averaging

Pont et al. (2006) developed a method to estimate the uncertainty of a transit or eclipse-depth calculation using the light-curve data points themselves. They considered the noise as the sum in quadrature of two components, a purely white (uncorrelated) source (characterized by a standard deviation per data point σ_w), and a purely time-correlated source (characterized by σ_r). Considering this, the white-noise component of the transit-depth uncertainty scales as:

$$\sigma_d = \frac{\sigma_w}{\sqrt{n}}, \quad (4.5)$$

with n the number of data points in the transit. On the other hand, the time-correlated standard deviation, σ_r , is independent of the number of data points. Hence, for any given signal, the uncertainty of a measurement should scale as:

$$\sigma_d = \sqrt{\frac{\sigma_w^2}{n} + \sigma_r^2}. \quad (4.6)$$

Note that for small n , σ_d is dominated by σ_w/\sqrt{n} , whereas as n increases, σ_d approaches σ_r . The time-averaging method uses this fact to estimate the contribution from the correlated noise. We followed the procedure described by Winn et al. (2007). First, we calculated the residuals between the data points and the best-fitting model. Then, we grouped the residuals in bins of N elements each, and calculated their mean values. Lastly, we calculated the standard deviation (or root mean squared, rms) of the binned residuals, rms_N . We repeated the process for a range of bin sizes from one to half the data size.

Now, let σ_1 be the rms value of the non-binned residuals (which is dominated by white noise). In the absence of correlated noise, the rms for the set of M bins, each containing N points, is given by the extrapolation of σ_1 (Winn et al. 2008):

$$\sigma_N = \frac{\sigma_1}{\sqrt{N}} \sqrt{\frac{M}{M-1}}. \quad (4.7)$$

The rms_N and σ_N curves are analogous to Equations (4.6) and (4.5), respectively. Their ratio, $\beta_N = \text{rms}_N/\sigma_N$, serves as a scaling factor to correct the uncertainties for time-correlated noise. One typically visualizes both curves in an rms vs. bin size plot (Figure 4.1).

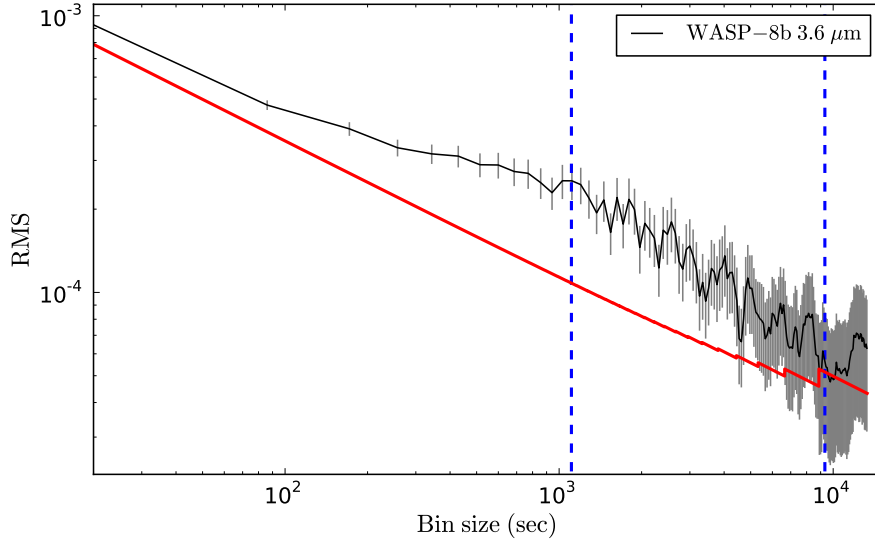


Figure 4.1: Binned residuals rms vs. bin size (black curve with gray error bars) of WASP-8b Spitzer eclipse at $3.6 \mu\text{m}$ (PI J. Harrington, Program ID 60003, see Cubillos et al. 2013). The red curve corresponds to the expected rms for white noise (Equation 4.7). The vertical dashed lines mark the durations of ingress/egress (left) and eclipse (right). The 1σ uncertainties of the rms curve correspond to $\sigma_N/\sqrt{2N}$ (Stevenson et al. 2012a); see Appendix 4.9 for the derivation.

4.3.2.1 Gaussian-noise Test

We have noted in the literature that some exoplanet-fit rms curves deviate below the σ_N curve (e.g., Stevenson et al. 2012a, Cubillos et al. 2013, Blečić et al. 2013). We studied that behavior further by analyzing the rms curves for zero-mean, random, normally-distributed signals. Such signals represent the residuals of an ideal fit to a data set affected only by uncorrelated noise. In this case, we expect the σ_N curve to be a good estimator of $\text{rms}_{\mathcal{N}}$.

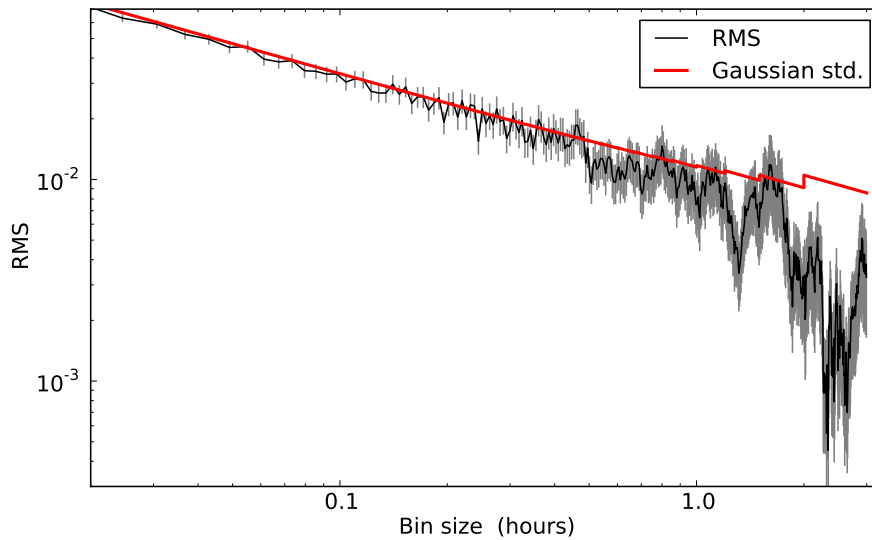


Figure 4.2: rms vs. bin size for a zero-mean normal-distribution. The error bars denote the 1σ uncertainties. The red curve corresponds to σ_N . There are 54,000 points, simulating a cadence of 0.4 seconds for a 6 hour observation.

We generated four zero-mean normal-distribution sets of 1000 realization each, using the Python routine `numpy.random.normal` with a standard deviation of 1. We determined the number of datapoints per trial by simulating cadences of 0.4 and 2 seconds and observation durations of 6 and 10 hours. These configurations correspond to the typical values for Spitzer transit or eclipse observations.

As expected, the rms curves deviated above σ_N (by more than one standard deviation) in less than 1% of the trials. On the other hand, more than a third of the trials showed large deviations of the rms curve ($> 3\sigma$) below σ_N (Figure 4.2), particularly when the bin size approached the observation time span. All four sets returned similar fractions of trials above and below σ_N . These not uncommon artifacts can partially or totally obstruct our ability to estimate correlated noise.

4.3.3 *Residual Permutation*

Residual permutation (also called prayer bead) is a nonparametric bootstrapping method from frequentist statistics. Nonparametric bootstrapping methods directly use the sampled data (typically via resampling) to generate a distribution that approximates the probability distribution of the data. The motivating idea is to shift the data while preserving the time ordering and, thus, preserving the correlation structure. While this is true, when there is correlated noise, the shifted datasets do not correspond to independent replications from any distribution, and thus do not exhibit the variability necessary for uncertainty quantification (e.g., computing confidence levels or estimator bias).

In the exoplanet field, the residual-permutation technique has been repeatedly used to estimate parameter uncertainties. However, the name of the technique has been loosely used to describe similar, but not equivalent procedures over the past decade. Bouchy et al. (2005), Gillon et al. (2007), and Southworth (2008) all describe different methods, when referring to residual permutations. Some authors reference Jenkins et al. (2002), who actually use a “segmented bootstrap”, applying the method for detection instead of parameter estimation. Furthermore, several authors have wrongly attributed the method to Moutou et al. (2004).

Currently, the most widely-used version of residual permutation is the one described by Southworth (2008) or Winn et al. (2008). This implementation computes the residuals between the light curve and the best-fitting model, cyclically shifts the residuals (preserving the point-to-point structure and thus the “redness” of the noise) by a given number of data points, adds the residuals back to the model, and finds a new set of best-fitting parameters. Usually, either one repeats the shift–fit

process for a large number of iterations with random shifts, or one sequentially shifts the residuals by one data point at a time, fitting all possible shifts. Each parameter uncertainty is then given by the respective standard deviation of the distribution of best-fitting values. Section 4.4.1 tests this implementation for an example with synthetic data. As expected, the method fails to estimate the parameter uncertainties.

4.3.4 Wavelet Analysis

Carter & Winn (2009) introduced to the exoplanet field a technique where the time-correlated noise is modeled using wavelet transforms (Deriche & Tewfik 1993, Wornell 1993, Wornell & Oppenheim 1992a,b). This method projects the time-series residuals into an orthonormal wavelet basis, where the off-diagonal terms of the covariance matrix become negligible, thus simplifying the likelihood function calculation. Furthermore, they assumed noise that has a power spectral density with frequency f , varying as $1/f^\gamma$. They parameterized the noise with three parameters, γ , σ_ω , and σ_r , as described in Equations (41)–(43) of Carter & Winn (2009).

A thorough review of wavelets is beyond the scope of this work; see Mallat (2008) and Wornell (1996) for more comprehensive discussions. Briefly, a wavelet transform projects a time-series signal onto a basis of functions that are dilations and translations of a compact parent (“wavelet”) function. The resulting transform has two dimensions, scale and time. The discrete wavelet transform (DWT) consists of the hierarchical application over M dilation scales of an orthonormal wavelet transform on a discrete time-series signal. For a signal consisting of $N = N_0 2^M$ uniformly-spaced samples (with N_0 integer), and a wavelet function with $2N_0$ coefficients, the DWT produces N_0 scaling coefficients and $N_0 2^{m-1}$ wavelet coefficients at each scale m , totaling $N_0(2^M - 1)$ wavelet coefficients.

4.3.4.1 Wavelet-based Likelihood

The likelihood function in the wavelet analysis is calculated in the following way. Let $\epsilon(t)$ be the fitting residuals of a time-series signal. Considering $\epsilon(t)$ as the contribution of a time-correlated ($\gamma \neq 0$) and an uncorrelated ($\gamma = 0$) component:

$$\epsilon(t) = \epsilon_\gamma(t) + \epsilon_0(t), \quad (4.8)$$

this method calculates the DWT of $\epsilon(t)$ to produce the wavelet, r_n^m , and scaling, \bar{r}_n^1 , coefficients of the signal. The variances of these coefficients are estimated, respectively, as:

$$\sigma_W^2 = \sigma_r^2 2^{-\gamma m} + \sigma_\omega^2 \quad (4.9)$$

$$\sigma_S^2 = \sigma_r^2 2^{-\gamma} g(\gamma) + \sigma_\omega^2, \quad (4.10)$$

where σ_ω and σ_r parameterize the standard deviation of the uncorrelated and the correlated-noise signals, respectively. See Appendix 4.10 for the derivation of $g(\gamma)$. Therefore, the wavelet-based likelihood function is given by

$$\mathcal{L}(\mathbf{x}, \sigma_\omega, \sigma_r) = \left\{ \prod_{m=1}^M \prod_{n=1}^{N_0 2^{m-1}} \frac{1}{\sqrt{2\pi\sigma_W^2}} \exp \left[-\frac{(r_n^m)^2}{2\sigma_W^2} \right] \right\} \times \left\{ \prod_{n=1}^{n_0} \frac{1}{\sqrt{2\pi\sigma_S^2}} \exp \left[-\frac{(\bar{r}_n^1)^2}{2\sigma_S^2} \right] \right\}. \quad (4.11)$$

Equation (4.11) allows one to fit a model, sample its parameter's posterior distribution, and determine the credible region, while taking into account the effects of time-correlated noise.

4.3.4.2 Wavelet-likelihood Errata

During our review and implementation of the wavelet-likelihood technique from Carter & Winn (2009), we found a few oversights in their equations and code (available in the Astronomical Source Code Library, ASCL¹). First, the index for the scale, m , of the likelihood function in their Equations (32) and (41) should start from 1 (however, the online code has the correct index value).

Next, the variance of the scaling coefficient in the ASCL code, Equation (34) of the paper, for $\gamma = 1$, is missing the factor $2^{-\gamma} = 2^{-1}$. The corrected equation should read:

$$\sigma_S^2 = \frac{\sigma_r^2}{4 \ln 2} + \sigma_\omega^2. \quad (4.12)$$

Lastly, Section 4.1 of Carter & Winn (2009) mentions that they used a data set of 1024 elements, and that their DWT produced 1023 wavelet coefficients and 1 scaling coefficient (implying $N_0 = 1$). This is inconsistent with the wavelet used (a second-order Daubechies wavelet), for which $N_0 = 2$. This wavelet's DWT returns 2 scaling coefficients and 1022 wavelet coefficients (for the given dataset). The ASCL code is also suited to perform a likelihood calculation assuming $N_0 = 1$, resulting in each likelihood term having an m value offset by 1.

4.4 Correlated-noise Tests for Exoplanet Eclipse Data

We carried out simulations to assess the performance of the correlated-noise estimators described in Section 4.3. We focused on estimating the secondary-eclipse depth in a light curve observation, creating synthetic light curves that represent Spitzer InfraRed Array Camera (IRAC) observations in terms of the S/N, known systematics, cadence, observation duration, and eclipse shape.

¹<http://asterisk.apod.com/viewtopic.php?f=35&t=21675>

In our first experiment we tested the estimators’ performances when the time-correlated noise is described by a signal with a $1/f$ power spectral distribution (similar to the experiment of Carter & Winn 2009). We tested the case when the observation time span is similar to the eclipse-event duration (Section 4.4.1, typical of secondary eclipse observations) and for the hypothetical case when the time span lasted an order of magnitude longer than the eclipse event (Section 4.4.2). In a second experiment (Section 4.4.3) we tested the estimators on a more realistic case by injecting a synthetic eclipse feature into a Spitzer phase-curve dataset.

4.4.1 Synthetic-noise Simulation

For this simulation we generated synthetic light curves by combining a Mandel & Agol (2002) eclipse model, a linear ramp model, and a signal with both correlated and uncorrelated noise. The light-curve parameters closely follow those of a Spitzer observation of the WASP-12 system (Table 4.1). The signal consisted of 1700 data points, with a cadence of ~ 12 seconds between data points, spanning an orbital-phase range from 0.39 to 0.63, about twice the eclipse duration.

Table 4.1: Synthetic Light-curve Parameters

Parameter	Value
Eclipse depth (counts)	98.1
Eclipse duration (phase)	0.1119
Eclipse mid point (phase)	0.5015
Eclipse ingress/egress time (phase)	0.013
Ramp slope (counts/phase)	0.006
System flux (counts)	25815
σ_ω (counts)	64.5
σ_r (counts)	0, 230, and 459

We created three sets of 5000 light-curve realizations each. For each realization, we generated a zero-mean random normal distribution, which we added to the light curve as the uncorrelated noise. We adjusted the variance of this signal (σ_ω^2) to yield an eclipse-depth signal-to-noise ratio of 30. Additionally, we generated purely-correlated $1/f$ signals ($\sigma_\omega = 0$) using a Gaussian random number generator with variances given by Equations (4.9) and (4.10). Then, we applied the inverse DWT to transform the signal from the wavelet basis to the time domain. Following the notation of Carter & Winn (2009), α denotes the ratio between the rms of the uncorrelated and correlated noise signals.

We left the first set with pure uncorrelated noise ($\alpha = 0$), we added to the second set a weak time-correlated signal ($\alpha = 0.25$), and we added to the third set a strong correlated signal ($\alpha = 0.5$). Figure 4.3 shows two synthetic light curves for $\alpha = 0.25$ and $\alpha = 0.5$. Note that our designations of “weak” and “strong” are, to some extent, arbitrary. We selected these limits based on our experience and tests: we observed that for $\alpha \lesssim 0.20$, the time-correlated signal becomes negligible compared to the uncorrelated-noise signal. On the other hand, ratios of $\alpha \sim 0.5$ are on the level of what we have observed in some cases (e.g., WASP-8b, Cubillos et al. 2013).

For each realization, we estimated the parameter posteriors using the methods described in Section 4.3. Our model-fitting routines only fixed the eclipse ingress/egress-time parameter (usually poorly-constrained by eclipse data), leaving the system flux, eclipse depth, eclipse midpoint, eclipse duration, and ramp slope free. First, we carried out a “white analysis” by using Equation (4.3) to estimate the model-parameter best-fitting values (using the Levenberg-Marquardt algorithm) and their posterior distributions (using MCMC).

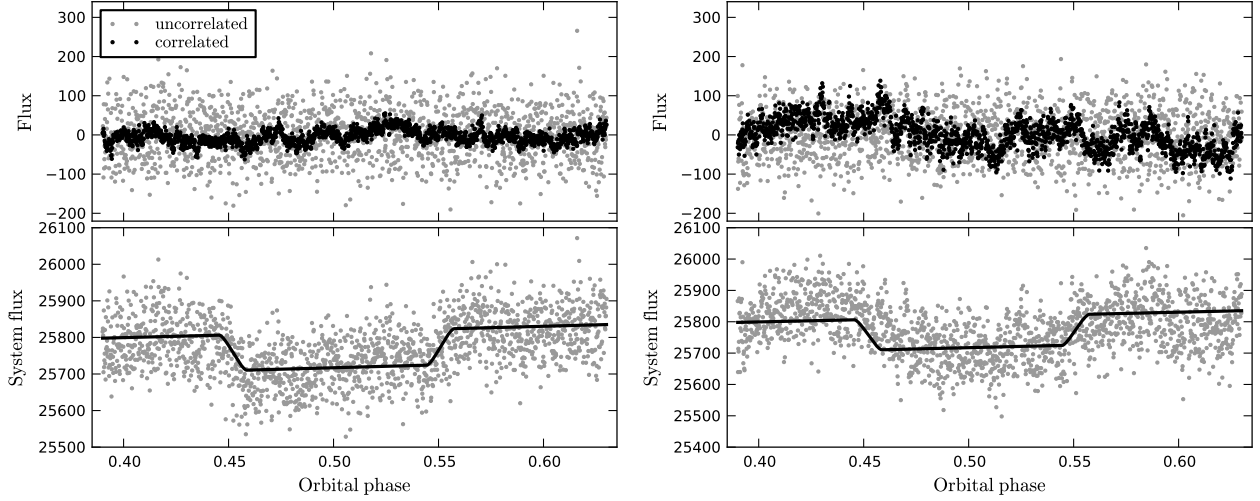


Figure 4.3: Simulated Spitzer time-series data sets. The top panels overplot the correlated (black) and uncorrelated (grey) noise components of the light curves vs. orbital phase. The bottom panels show the synthetic light curves (eclipse, ramp, and noise) vs. orbital phase in gray. The black solid line shows the noiseless model. The noise rms ratios are $\alpha = 0.25$ (left panels) and $\alpha = 0.5$ (right panels).

Next, we used the MCMC results to calculate the time-averaging rms-vs.-bin-size curves. We retrieved the β factor at three timescales: at the ingress time, at the eclipse duration, and at the time of maximum β (β_{\max} , Figure 4.4). In accordance with the discussion in Section 4.3.2.1, most β values at the eclipse-duration timescale (similar to the total observation duration) were underestimated ($\beta < 1$). We adopted β_{\max} as the scaling factor to calculate the time-averaging method uncertainties. We also ran the residual-permutation method by applying Equation (4.3) with the Levenberg-Marquardt algorithm. Finally, we applied the wavelet-based likelihood method in an MCMC guided by Equation (4.11). We simultaneously fit the noise parameters (σ_{ω} and σ_r)

and the model parameters, while keeping γ fixed at 1. We found that a Jeffrey's non-informative prior on σ_r handled the case with no correlated noise better. A Jeffrey's prior is a scale-invariant prior that has an equal probability per order of magnitude. It is a more convenient prior when the parameter may range over several orders of magnitude (Gregory 2005). The only requirement is that the parameter value must be positive.

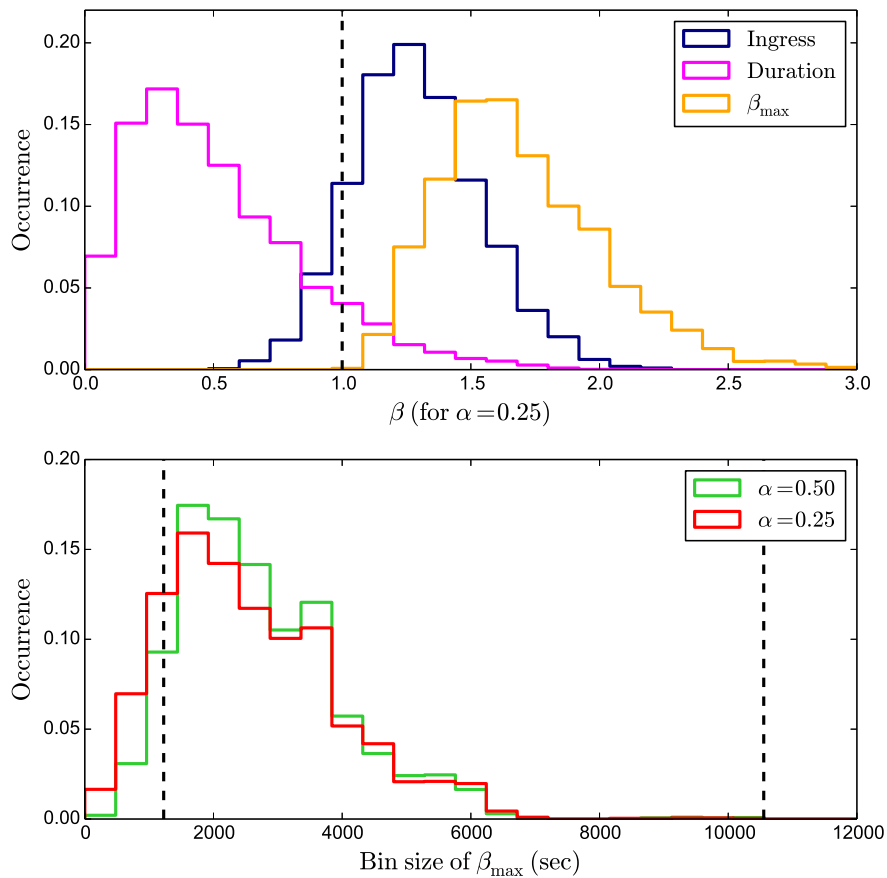


Figure 4.4: **Top:** Normalized distribution of β for the $\alpha = 0.25$ set. The histograms represent β measured at the ingress-time and eclipse-duration timescales, and at the maximum value of β . The distributions for the other two sets ($\alpha = 0$ and 0.5) were similar. **Bottom:** Normalized distribution of the bin sizes for β_{\max} . The vertical dashed lines indicate the ingress time and eclipse duration.

4.4.1.1 Results

To analyze the results, we proceeded in a similar way as Carter & Winn (2009): for the different sets and methods, we calculated the accuracy-to-uncertainty ratio (\mathcal{N}_p , the difference between the estimated, \hat{p} , and the true, p , value of a parameter, divided by the estimated uncertainty, $\hat{\sigma}_p$):

$$\mathcal{N}_p = \frac{\hat{p} - p}{\hat{\sigma}_p}. \quad (4.13)$$

A higher noise level in the light curve should worsen the model accuracy and increase the parameter uncertainties. In the ideal case, we expect the variation of these two quantities to scale such that the set's standard deviation of the accuracy-to-uncertainty ratio, $\sigma_{\mathcal{N}}$, approaches unity for large N . If $\sigma_{\mathcal{N}} > 1$, the method underestimates the uncertainties, and vice versa.

Figure 4.5 shows the distribution of estimated eclipse-depth uncertainties for each method and set. To find the ideal uncertainty level, we scaled the uncertainties of each set and method by a constant such that $\sigma_{\mathcal{N}} = 1$. The vertical dashed lines indicate the mean value of the scaled uncertainties. Note that $\sigma_{\mathcal{N}}$ depends on the particular distribution of $\{\hat{p}, \hat{\sigma}_p\}$ pairs, thus, the expected uncertainties differ for each method. Table 4.2 shows the standard deviation of the accuracy-to-uncertainty ratio for each set.

Table 4.2: $\sigma_{\mathcal{N}}$ for Synthetic-data Sets

α	White MCMC	R. Permutation	T. Averaging	Wavelet
0.00	1.01	2.00	0.95	1.13
0.25	2.23	2.47	1.42	0.90
0.50	3.83	2.27	1.58	0.85

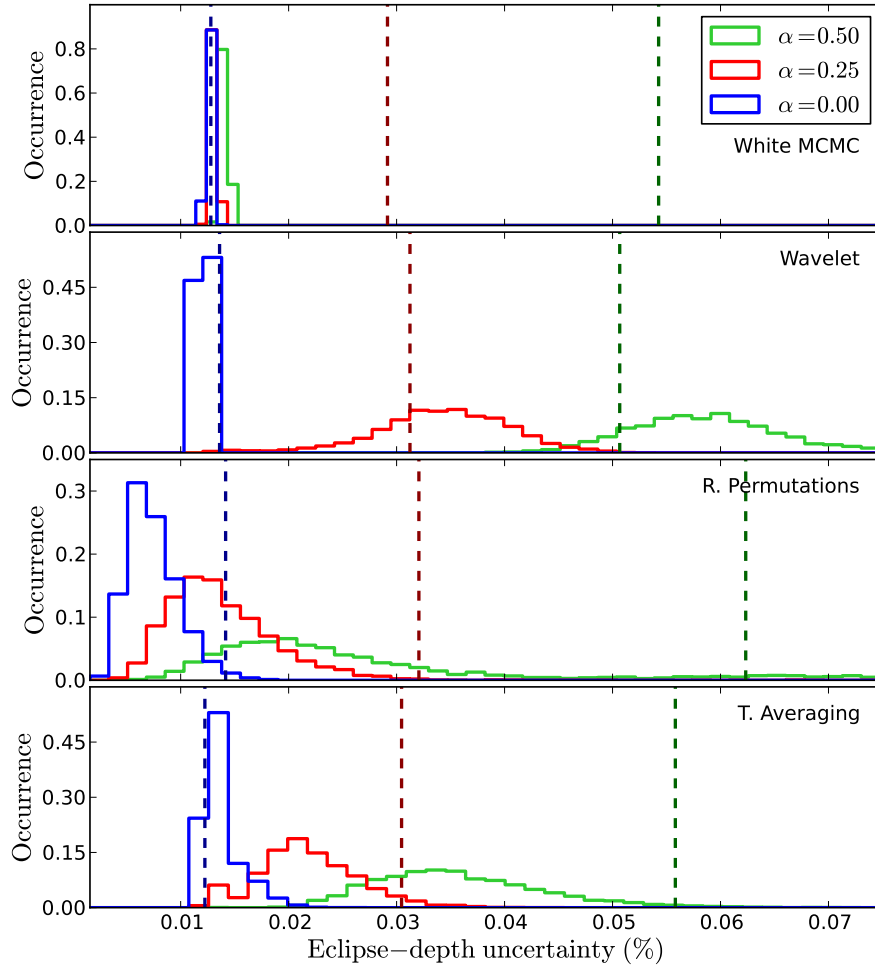


Figure 4.5: Distribution of the estimated eclipse-depth uncertainties for the MCMC (top panel), wavelet (second panel), residual-permutation (third panel), and time-averaging analysis (bottom panel). The vertical dashed lines indicate the expected mean uncertainty that would have yielded $\sigma_{\mathcal{N}} = 1$.

As expected, the white-MCMC analysis correctly estimated the uncertainties for the uncorrelated noise set, but it is insensitive to time-correlated noise. This is reflected in the clustering of the uncertainties at the same value, regardless of the amount of time-correlated noise (Fig. 4.5, top panel) and the increase of $\sigma_{\mathcal{N}}$ with increasing α (Table 4.2). The uncertainty distributions for the three other methods do correlate with α , but only at a qualitative level. The residual-permutation method produced the least-accurate results, underestimating the uncertainties, including the case

without correlated noise. The time-averaging method underestimated the uncertainties, whereas the wavelet analysis slightly overestimated the uncertainties (Fig. 4.5 and Table 4.2).

4.4.2 Long-duration Synthetic-noise Simulation

We tested the correlated-noise estimators in the regime where the time-averaging method is not affected by the artifacts described in Section 4.3.2.1. Here we replicated the previous experiment, but for a total observation time ~ 20 times longer than the eclipse duration (akin to a phase-curve observation). We generated the light curve with the same eclipse configuration as in Section 4.4.2, keeping the cadence (17,000 data points total) and the value of σ_ω at 64.5. To conserve the noise rms ratios at $\alpha = 0.25$ and 0.5, we set $\sigma_r = 774$ and 1549, respectively.

Upon applying the time-averaging analysis we confirmed that the β factor corresponding to the eclipse duration is less affected by the method's artifacts. Furthermore, we found that this β factor accurately corrects the uncertainties for the time-correlated noise (Figure 4.6).

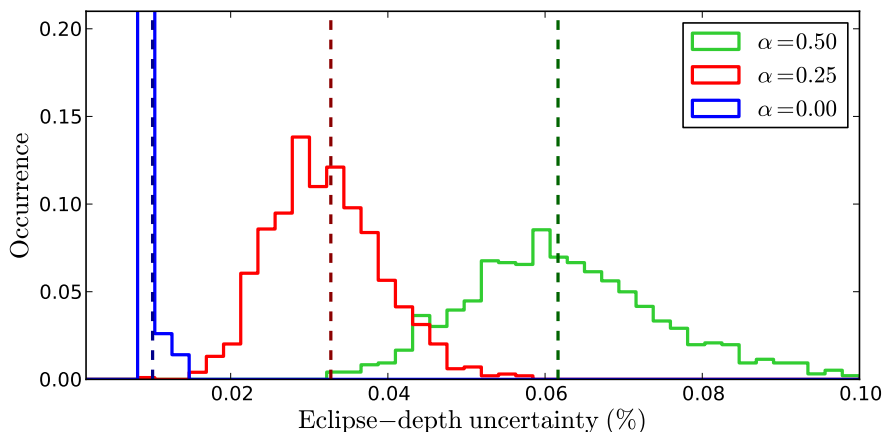


Figure 4.6: Distribution of estimated eclipse-depth uncertainties for the time-averaging analysis (using β of the eclipse duration). For these simulations, the length of the light curves was 20 times that of the eclipse duration. The vertical dashed lines indicate the expected mean uncertainty that would have yielded $\sigma_{\mathcal{N}} = 1$.

4.4.3 Simulation with Spitzer-IRAC Noise

In this section we tested the correlated-noise estimators for a real exoplanet signal known to be affected by correlated noise. Hence, we do not assume any functional form for the noise, we rather use the true instrumental noise as detected by the telescope. We selected the 4.5 μm Spitzer IRAC phase curve of the extrasolar planet HD 209458b (PI H. Knutson, Program ID 60021, AOR 38703872) published by Zellem et al. (2014). We generated a set of trials by injecting a synthetic eclipse signal, which we then recovered with the time-averaging and wavelet-likelihood techniques.

First we constructed a flat baseline light curve by removing the eclipse, transit, and phase-curve sinusoidal signals from the data set (but conserving the systematics). The data consisted of a 24 hour-long continuous observation of the HD 209458 system, starting shortly before an eclipse event and ending shortly after a transit event, covering the orbital phase from 0.42 to 1.05 (orbital period 3.52 days), with a mean cadence of 0.4 seconds (1.31×10^{-6} orbital phase span). We processed the Spitzer BCD data to obtain a raw light curve using the Photometry for Orbits, Eclipses, and Transits (POET) pipeline (Stevenson et al. 2010, 2012a,b, Campo et al. 2011, Nymeyer et al. 2011, Cubillos et al. 2013, 2014). We trimmed the data to the time span contained after the eclipse and before the transit (orbital phase from 0.52 to 0.98). Since the ramp variation is negligible after a few hours of observation, the resulting section of the dataset contained only the astrophysical signal (the stellar background and the planetary phase-curve variation) and the instrument’s intrapixel systematics (Charbonneau et al. 2005).

We then fit the remaining light curve with a BLISS map model (the intrapixel effect, Stevenson et al. 2012a), and a sinusoidal function (for the phase-curve variation, following Zellem et al. 2014):

$$F(t) = 1 + c_0 + c_1 \cos(2\pi t) + c_2 \sin(2\pi t), \quad (4.14)$$

where c_0 , c_1 , and c_2 are the model fitting parameters, and t is the time of the observation (measured in orbital phase). To avoid degeneracy with the other fitting parameters, we constrained c_0 by requiring $F(t_0) \equiv 1$, with t_0 the eclipse midpoint time. We finally subtracted the best-fitting sinusoidal model to remove the phase-curve variation.

To construct the trial samples, we injected a Mandel-Agol eclipse curve at random midpoints into the baseline. We drew the midpoints from a uniform distribution between orbital phases 0.65 and 0.85. We set the eclipse ingress/egress time to 19.8 min (0.0039 orbital phase span) and the eclipse depth to 0.125% of the system flux. To test how the time-averaging method performs as a function of the observing length-to-eclipse time span ratio, we generated two sets with eclipse durations of 2.9 hr (0.034 orbital phase span) and 1.5 hr (0.018 orbital phase span), with 3000 realizations each.

Our fitting model included the eclipse (Mandel and Agol) and the BLISS-map model. For the wavelet-likelihood analysis we trimmed the dataset to a time span of 7.2 hr (0.085 orbital phase span) around the eclipse midpoint, since the MCMC often failed to converge for larger datasets. We analyzed the results in the same manner as in Section 4.4.1.1. Figure 4.7 shows the distribution of the eclipse-depth uncertainties for each method and set. Table 4.3 presents the standard deviation of the uncertainty-to-accuracy ratios.

Table 4.3: σ_N for the HD 209458b Sets

Eclipse Duration (hr)	White MCMC	T. Averaging	Wavelet
2.9	2.772	1.553	1.176
1.5	2.293	1.241	1.462

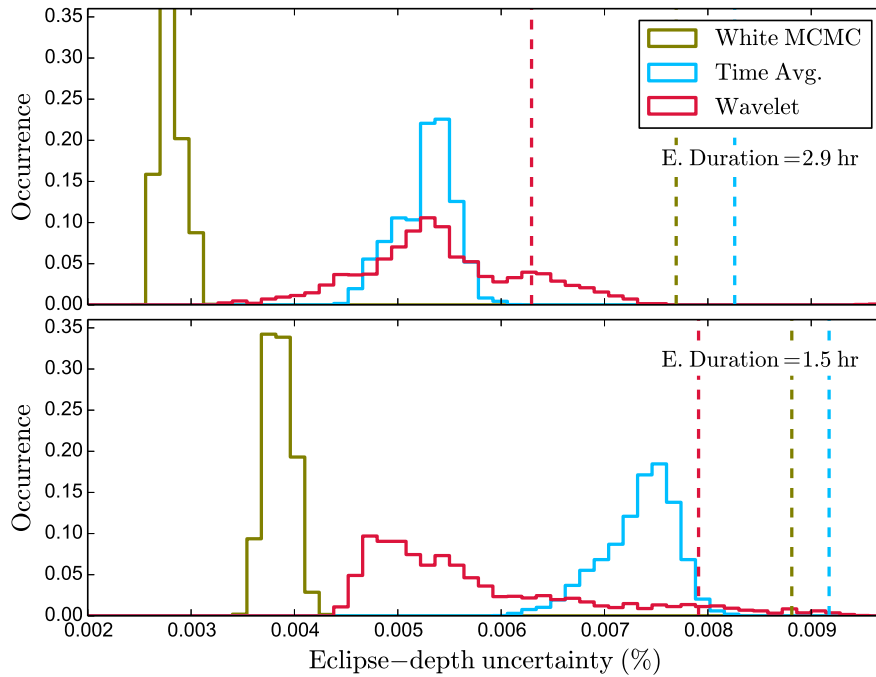


Figure 4.7: Distribution of estimated eclipse-depth uncertainties for long (top panel) and short (bottom panel) eclipse duration simulations. The vertical dashed lines indicate the expected mean uncertainty that would have yielded $\sigma_{\mathcal{N}} = 1$ for each method.

Figure 4.7 shows that, in general, the longer-eclipse set returns smaller uncertainties than the shorter-eclipse set. This is expected given the lower number of data points contributing in a shorter eclipse. Table 4.3 shows that both methods improved the estimation of the eclipse depth uncertainty, underestimating it from $\sim 20\%$ to 50% . The time-averaging method, as expected, performed better for the shorter-eclipse set (observation span-to-eclipse duration ratio of 25.5, compared to 15.5 for the longer-eclipse set). The wavelet-likelihood method, on the other hand, performed better for the longer-eclipse set.

4.5 Multi-Core Markov-Chain Monte Carlo (MC³) Code

We implemented all of the discussed statistical methods into the open-source Python module Multi-Core Markov-Chain Monte Carlo (MC³, github.com/pcubillos/MC3). Unlike other exoplanet model-fitting tools that are tailored to specific tasks, MC³ allows the user to define the modeling function and, thus, it is a general-purpose statistical package. We developed the main bulk of the code in Python, with several extensions written in C, combining simplicity and high performance. The code runs in a single CPU or in multiple parallel processors (through Message Passing Interface, MPI). MC³ provides statistically-robust model optimization (via Levenberg-Marquardt minimization) and credible-region estimation (via MCMC sampling) routines.

The MCMC random sampling is done via the Metropolis Random Walk (MRW, using multivariate Gaussian proposals) or the Differential-Evolution Markov-chain Monte Carlo algorithm (DEMC, ter Braak 2006). While the proposal step sizes of the MRW are predetermined by the user and have to be manually adjusted before each run, DEMC automatically adjusts the scale and orientation of the proposal distribution. To do so, DEMC runs several chains in parallel, computing the proposed jump for a given chain from the difference between the parameter states of two other randomly selected chains. As the chains converge toward the posterior distribution, the proposal jumps will be mainly oriented along the desired distribution and will have adequate scales. Therefore, DEMC improves the MCMC efficiency in two ways: (1) it increases the acceptance rate to optimal levels ($\gtrsim 25\%$, Roberts et al. 1997) by better sampling the phase space, and (2) it eliminates the heuristic need for the user to adjust the proposal jump scales.

The Metropolis-Hastings acceptance rule implements both the regular likelihood function (Eq. 4.3) and the wavelet-based likelihood (Eq. 4.11). The priors can be bounded or unbounded uniform, log-scale uniform (Jeffrey's), or Gaussian. To assess that the MCMC is working properly, the code performs a chain-convergence test using the Gelman & Rubin (1992) statistics. The code also produces several plots to help visualize the results: trace, rms-vs.-bin-size, marginal-posterior, and pairwise-posterior plots can indicate non-convergence, multi-modal posteriors, parameter correlations, correlated noise, or incorrect priors. At the end of the MCMC run the code returns the sampled posterior distribution of the parameters, their best-fitting values, their 68% credible region, and the acceptance rate of the MCMC. The majority of the routines of this module derive from our POET pipeline and, thus, have been thoroughly tested for years.

The core structure of MC^3 consists of a central hub, which drives the MCMC exploration, and the workers, which evaluate the model for the given free parameters. When run in parallel, the hub communicates with the workers through MPI, sending the free parameters and receiving the evaluated models back (transmitting the data as one-dimensional arrays). MC^3 assigns one CPU to each worker (i.e., one for each chain). When run in a single CPU, the hub evaluates the models *in situ*. Each cycle (iteration) of the MCMC comprises the following steps: (1) the hub generates the proposal state (the set of free parameters) for each chain, (2) the workers (or the hub) evaluate the model for the proposed state, (3) the hub computes the Metropolis ratio and accepts/rejects the proposal state for each chain.

The MC³ code runs from both the shell prompt and the Python interactive interpreter. The user can configure the MCMC run either through a configuration file, command line arguments (prompt), and/or function arguments (Python interpreter). The minimum required inputs are the modeling function, the data being fitted, and starting estimate values for the free parameters. As optional arguments, the user can supply the data uncertainties, priors, and any extra arguments of the modeling function (in a manner much like the `scipy.optimize.leastq` routine). Additionally, the package allows the user to configure multiple features of the MCMC, e.g.: number of chains, number of iterations, burn-in length, thinning factor, etc. The repository of the code includes a user manual and guided examples.

4.6 Conclusions

Time-correlated noise is an important source of uncertainty for faint signals such as exoplanet light curves. Unless all systematics of the data are well understood, the correlated noise must be taken into account to obtain a reliable estimation of the parameter uncertainties. We have reviewed three of the most widely used methods to assess time-correlated noise in exoplanet time-series data: time averaging, residual permutation, and wavelet-based likelihood. We expanded the limited literature of tests to assess the quantitative results of these techniques, focusing specifically on the case of Spitzer secondary-eclipse time-series data.

We found that the rms-vs.-bin-size curve of the time-averaging method can often present artifacts that partially or totally obstruct our assessment of the correlated noise with this method for typical eclipse or transit data. These artifacts are particularly prominent at timescales with the same order of magnitude as the total observation duration. The residual-permutation method is unsound as a tool for quantifying uncertainty in parameter estimates, because it does not produce ensembles that mimic the behavior of independent draws from a probability distribution. In our review and implementation of the wavelet method by Carter & Winn (2009), we found and corrected errors in the equations of the publication and the online code (Section 4.3.4.2).

We developed the Multi-Core Markov-Chain Monte Carlo open-source Python module (MC³, <https://github.com/pcubillos/MCcubed>). MC³ implements all of the statistical routines described in this paper, allowing the user to estimate best-fitting model parameters and their credible region, while letting the user provide the modeling function. Given the challenging nature of exoplanet observations, most analyses require a great deal of fine-tuning and use of advanced reduction and statistical techniques. By releasing our code to the community, we hope not only to provide access to the routines discussed here, but also to encourage researchers to consider open development and cross-validation of the software tools used in the field.

We tested the time-correlated analysis methods on synthetic exoplanet eclipse light curves, focusing on eclipse-depth estimation. In our first simulation, we tested the case when the time-correlated noise has a power spectral density of the form $1/f$. We generated synthetic light curves consistent with the S/N level, cadence, known telescope systematics, and observation duration of a Spitzer IRAC eclipse observation. The light curves are composed of a Mandel and Agol eclipse model, a linear ramp model, uncorrelated noise (random normal distribution), and $1/f$ time-correlated noise. The residual-permutation method returned the poorest results, largely underestimating the uncertainties. Both the time-averaging and the wavelet-likelihood methods provided better estimations of the uncertainties than a white MCMC analysis, although with some limitations: the

wavelet-likelihood method overestimated the eclipse-depth uncertainty by about 10%, whereas the time-averaging method underestimated the uncertainties by about 50%. When the eclipse duration is short compared to the total observation duration (e.g., a phase-curve observation), the time-averaging correction accurately estimates the eclipse-depth uncertainty for uncorrelated and $1/f$ -correlated noise.

In a further simulation, we generated eclipse light-curve samples by injecting an eclipse signal into a real Spitzer IRAC ($4.5 \mu\text{m}$) time-series dataset as a baseline. This experiment allowed us to assess the performance of the time-correlated estimators without assuming a specific shape of the time-correlated signal. We studied the results for two sets with a different eclipse duration each. Both the time-averaging and the wavelet-likelihood methods significantly improved the uncertainty estimations compared to a white MCMC analysis. However, they are not perfect, as in both cases the uncertainties are overestimated by $\sim 20 - 50\%$. Similar to the previous simulation, the time-averaging method performed better when the eclipse duration is shorter compared to the total observation time. In contrast, the wavelet-likelihood analysis performed better for the simulation with a longer eclipse duration. If the correlated noise present in other Spitzer data sets behaves in a similar manner as the one treated here, there is not yet a universally best method for assessing time-correlated noise.

4.7 Acknowledgements

We thank contributors to SciPy, Matplotlib, and the Python Programming Language, the free and open-source community. PC is supported by the Fulbright Program for Foreign Students. Part of this work is based on observations made with the *Spitzer Space Telescope*, which is operated by the Jet Propulsion Laboratory, California Institute of Technology under a contract with NASA. Support for this work was provided by NASA through an award issued by JPL/Caltech and through the NASA Science Mission Directorate's Astrophysics Data Analysis Program, grant NNH12ZDA001N.

4.8 Bayesian Credible Region

In the Bayesian context, given the posterior probability density, $p(\theta|\mathbf{D})$, of a parameter, θ , given the dataset, \mathbf{D} , the highest posterior density region (or credible region), R , is defined by

$$C = \int_R d\theta p(\theta|\mathbf{D}) \quad (4.15)$$

where C is the probability contained in the credible region. The region R is selected such that the posterior probability of any point inside R is larger than that of any point outside.

In the practice, to calculate the credible region, one constructs a histogram of the sampled posterior distribution (normalized such that the sum equals one) and sorts the bins in descending order. Then one sequentially adds the values of p until reaching C . The credible-region boundaries are given by the smallest and largest values of θ for the samples considered in the sum, if the region is contiguous.

4.9 Standard Deviation Uncertainty

The uncertainty of a parameter estimate in a problem with a fixed model dimension (number of parameters) and growing sample size typically decreases asymptotically at the \sqrt{N} rate. That is, for estimating a Gaussian mean from N samples with the standard deviation σ , which is known, the uncertainty is σ/\sqrt{N} . However, this result says nothing about the actual *size* of the uncertainty at any particular sample size. When σ is unknown, it becomes the target of estimation, instead of (or in addition to) the mean. Here, we elaborate on the derivation of the uncertainty for the standard deviation of a Gaussian. The derivation uses the Laplace approximation for a normal standard deviation and its uncertainty, i.e., it finds a Gaussian distribution with a peak and curvature matching the marginal probability density function.

Given a normal distribution of values with unknown mean μ and standard deviation σ , let b_i be the means for a sample of N groups of samples (“bins”) drawn from this distribution. The sample mean, \bar{b} , and the sample variance, s^2 , are defined as usual:

$$\bar{b} = \frac{1}{N} \sum_i b_i, \quad s^2 = \frac{1}{N} \sum_i (b_i - \bar{b})^2. \quad (4.16)$$

If the residual $r_i = b_i - \bar{b}$ and $r^2 = \sum_i r_i^2$, then the sample variance becomes $s^2 = r^2/N$.

The likelihood function for our normal distribution with (μ, σ) is:

$$\begin{aligned} \mathcal{L}(\mu, \sigma) &= \prod_i p(b_i | \mu, \sigma) \\ &= \prod_i \frac{1}{\sigma\sqrt{2\pi}} \exp\left[-\frac{(b_i - \mu)^2}{2\sigma^2}\right], \end{aligned} \quad (4.17)$$

so the likelihood can be written in terms of \bar{b} and r as:

$$\mathcal{L}(\mu, \sigma) = \frac{1}{\sigma^N (2\pi)^{N/2}} \exp\left(-\frac{r^2}{2\sigma^2}\right) \exp\left(-\frac{N(\mu - \bar{b})^2}{2\sigma^2}\right). \quad (4.18)$$

To estimate μ and σ , we will adopt a flat prior for μ and a log-flat prior for σ , corresponding to $p(\sigma) \propto 1/\sigma$. Then, the joint posterior probability $p(\mu, \sigma|D)$ for μ and σ , given the data D is:

$$p(\mu, \sigma|D) \propto p(\sigma) \times \mathcal{L}(\mu, \sigma), \quad (4.19)$$

with $p(\sigma)$ the prior probability on σ .

$$p(\mu, \sigma|D) \propto \frac{1}{\sigma^{N+1}} \exp\left(-\frac{r^2}{2\sigma^2}\right) \exp\left(-\frac{N(\mu - \bar{b})^2}{2\sigma^2}\right). \quad (4.20)$$

Calculate the marginal posterior density for σ by integrating over μ :

$$p(\sigma|D) \propto \int \frac{1}{\sigma^{N+1}} \exp\left(-\frac{r^2}{2\sigma^2}\right) \exp\left(-\frac{N(\mu - \bar{b})^2}{2\sigma^2}\right) d\mu. \quad (4.21)$$

The μ dependence is in the last exponential factor, a Gaussian that integrates to $\sigma\sqrt{2\pi}$. We denote the result as $f(\sigma)$:

$$p(\sigma|D) \propto \frac{1}{\sigma^N} \exp\left(-\frac{r^2}{2\sigma^2}\right) = f(\sigma). \quad (4.22)$$

We estimate σ with its mode, $\hat{\sigma}$, which maximizes $f(\sigma)$. The first derivative of $f(\sigma)$ is:

$$f'(\sigma) = f(\sigma) \left(\frac{r^2}{\sigma^3} - \frac{N}{\sigma} \right), \quad (4.23)$$

so that setting $f'(\hat{\sigma}) = 0$ gives $\hat{\sigma} = r/\sqrt{N} = s$, as one might expect.

For a simple estimate of the uncertainty, let's consider a Gaussian approximation with mean at $\hat{\sigma}$.

The curvature (second derivative) of σ at $\hat{\sigma}$:

$$f''(\sigma) = f'(\sigma) \left(\frac{r^2}{\sigma^3} - \frac{N}{\sigma} \right) + f(\sigma) \left(\frac{N}{\sigma^2} - \frac{3r^2}{\sigma^4} \right), \quad (4.24)$$

determines the standard deviation. When $f(x)$ is of the form of a normal distribution with mean m and standard deviation w , it is easy to show that $f''(m) = -f(m)/w^2$. So, if δ is the standard deviation for σ , in the normal approximation, that matches the curvature at the peak, we have $\delta^2 \approx -f(\hat{\sigma})/f''(\hat{\sigma})$. Evaluating Equation (4.24) at $\hat{\sigma}$, the first term vanishes (since $f'(\hat{\sigma}) = 0$), and the remaining term gives an approximate standard deviation of:

$$\delta \approx \frac{r}{N\sqrt{2}} = \frac{s}{\sqrt{2N}}. \quad (4.25)$$

So, the mean and standard deviation sum for σ for large N is:

$$\sigma = s \pm \frac{s}{\sqrt{2N}}. \quad (4.26)$$

4.10 Wavelet Coefficients Variance

Starting from the Equation (37) of Wornell (1993), we calculate the variance of the wavelet coefficients as:

$$\text{var } x_n^m = E[x_n^m x_n^m] = \frac{2^{-m}}{2\pi} \int_{-\infty}^{\infty} \frac{\sigma_x^2}{|\omega|^\gamma} |\Psi(2^{-m}\omega)|^2 d\omega, \quad (4.27)$$

with a change of variable, $u = 2^{-m}\omega$, we have:

$$\text{var } x_n^m = 2^{-\gamma m} \frac{1}{2\pi} \int_{-\infty}^{\infty} \frac{\sigma_x^2}{|u|^\gamma} |\Psi(u)|^2 du. \quad (4.28)$$

Now, let

$$\sigma^2 = \frac{1}{2\pi} \int_{-\infty}^{\infty} \frac{\sigma_x^2}{|\omega|^\gamma} |\Psi(\omega)|^2 d\omega, \quad (4.29)$$

we then obtain the equation that follows Equation (37) of Wornell (1993):

$$\text{var } x_n^m = 2^{-\gamma m} \sigma^2. \quad (4.30)$$

This variance corresponds to Equation (24) of Carter & Winn (2009). In their notation: $\langle \epsilon_n^m \epsilon_n^m \rangle = \text{var } x_n^m$, and $\sigma_r^2 = \sigma^2$.

If we assume an ideal bandpass —i.e., Eq. (3) of Wornell (1993)— we can work our Eq. (4.28) to obtain Eq. (45) of Wornell (1993). Note that Eq. (3) of Wornell (1993) should read $\Psi(\omega)$ instead of $\psi(\omega)$. Then:

$$\text{var } x_n^m = 2^{-\gamma m} \frac{2}{2\pi} \int_{\pi}^{2\pi} \frac{\sigma_x^2}{|\omega|^\gamma} d\omega. \quad (4.31)$$

$$= 2^{-\gamma m} \frac{\sigma_x^2 [2^{1-\gamma} - 1]}{\pi^\gamma (1 - \gamma)}, \quad (4.32)$$

For $\gamma \neq 1$, in the notation of Carter & Winn (2009), we have:

$$\sigma_r^2 = \frac{\sigma_x^2 [2^{1-\gamma} - 1]}{\pi^\gamma (1 - \gamma)}. \quad (4.33)$$

In analogy to Eq. (4.28), we can repeat the process for the scaling coefficient:

$$\text{var } a_n^m = 2^{-\gamma m} \frac{1}{2\pi} \int_{-\infty}^{\infty} \frac{\sigma_x^2}{|\omega|^\gamma} |\Phi(\omega)|^2 d\omega. \quad (4.34)$$

Assuming again an ideal bandpass —i.e., Eq. (10) of Wornell (1993)— we obtain for $\gamma \neq 1$:

$$\text{var } a_n^m = 2^{-\gamma m} \frac{2}{2\pi} \int_0^\pi \frac{\sigma_x^2}{|\omega|^\gamma} d\omega. \quad (4.35)$$

$$= 2^{-\gamma m} \frac{\sigma_x^2}{\pi^\gamma} \frac{1}{1 - \gamma}. \quad (4.36)$$

If we plug in σ_r^2 from Eq. (4.33), we have:

$$\text{var } a_n^m = 2^{-\gamma m} \sigma_r^2 \frac{1}{2^{1-\gamma} - 1}, \quad (4.37)$$

where we can recognize $g(\gamma)$ from Carter & Winn (2009):

$$g(\gamma) = \frac{1}{2^{1-\gamma} - 1}. \quad (4.38)$$

This is consistent with Carter & Winn (2009) code for $\gamma \neq 1$, where he has:

$$\text{sm2} = \sigma_r^2 2^{-\gamma m} \frac{1}{2^{1-\gamma} - 1}, \quad (4.39)$$

$$= \sigma_r^2 \frac{1}{2 - 2^\gamma}. \quad (\text{for } m = 1) \quad (4.40)$$

4.11 List of References

Agol, E., Cowan, N. B., Knutson, H. A., Deming, D., Steffen, J. H., Henry, G. W., & Charbonneau, D. 2010, *ApJ*, 721, 1861

Ballard, S., Charbonneau, D., Deming, D., Knutson, H. A., Christiansen, J. L., Holman, M. J., Fabrycky, D., Seager, S., & A'Hearn, M. F. 2010, *PASP*, 122, 1341

Bevington, P. R. & Robinson, D. K. 2003, *Data reduction and error analysis for the physical sciences*

Blecic, J., Harrington, J., Madhusudhan, N., Stevenson, K. B., Hardy, R. A., Cubillos, P. E., Hardin, M., Campo, C. J., Bowman, W. C., Nymeyer, S., Lored, T. J., Anderson, D. R., & Maxted, P. F. L. 2013, *ApJ*, 779, 5

Bouchy, F., Pont, F., Melo, C., Santos, N. C., Mayor, M., Queloz, D., & Udry, S. 2005, *A&A*, 431, 1105

- Campo, C. J., Harrington, J., Hardy, R. A., Stevenson, K. B., Nymeyer, S., Ragozzine, D., Lust, N. B., Anderson, D. R., Collier-Cameron, A., Blečić, J., Britt, C. B. T., Bowman, W. C., Wheatley, P. J., Loredó, T. J., Deming, D., Hebb, L., Hellier, C., Maxted, P. F. L., Pollaco, D., & West, R. G. 2011, *ApJ*, 727, 125
- Carter, J. A. & Winn, J. N. 2009, *ApJ*, 704, 51
- Charbonneau, D., Allen, L. E., Megeath, S. T., Torres, G., Alonso, R., Brown, T. M., Gilliland, R. L., Latham, D. W., Mandushev, G., O'Donovan, F. T., & Sozzetti, A. 2005, *ApJ*, 626, 523
- Cubillos, P., Harrington, J., Madhusudhan, N., Foster, A. S. D., Lust, N. B., Hardy, R. A., & Bowman, M. O. 2014, *ApJ*, 797, 42
- Cubillos, P., Harrington, J., Madhusudhan, N., Stevenson, K. B., Hardy, R. A., Blečić, J., Anderson, D. R., Hardin, M., & Campo, C. J. 2013, *ApJ*, 768, 42
- Deming, D., Fraine, J. D., Sada, P. V., Madhusudhan, N., Knutson, H. A., Harrington, J., Blečić, J., Nymeyer, S., Smith, A. M. S., & Jackson, B. 2014, In prep.
- Demory, B.-O., Gillon, M., Seager, S., Benneke, B., Deming, D., & Jackson, B. 2012, *ApJ*, 751, L28
- Deriche, M. & Tewfik, A. 1993, *Trans. Sig. Proc.*, 41, 2977
- Fazio, G. G., Hora, J. L., Allen, L. E., Ashby, M. L. N., Barmby, P., Deutsch, L. K., Huang, J.-S., Kleiner, S., Marengo, M., Megeath, S. T., Melnick, G. J., Pahre, M. A., Patten, B. M., Polizotti, J., Smith, H. A., Taylor, R. S., Wang, Z., Willner, S. P., Hoffmann, W. F., Pipher, J. L., Forrest, W. J., McMurty, C. W., McCreight, C. R., McKelvey, M. E., McMurray, R. E., Koch, D. G., Moseley, S. H., Arendt, R. G., Mentzell, J. E., Marx, C. T., Losch, P., Mayman, P., Eichhorn,

W., Krebs, D., Jhabvala, M., Gezari, D. Y., Fixsen, D. J., Flores, J., Shakoorzadeh, K., Jungo, R., Hakun, C., Workman, L., Karpati, G., Kichak, R., Whitley, R., Mann, S., Tollestrup, E. V., Eisenhardt, P., Stern, D., Gorjian, V., Bhattacharya, B., Carey, S., Nelson, B. O., Glaccum, W. J., Lacy, M., Lowrance, P. J., Laine, S., Reach, W. T., Stauffer, J. A., Surace, J. A., Wilson, G., Wright, E. L., Hoffman, A., Domingo, G., & Cohen, M. 2004, *ApJS*, 154, 10

Gelman, A. & Rubin, D. B. 1992, *Statistical Science*, 7, 457

Gibson, N. P. 2014, *MNRAS*, 445, 3401

Gibson, N. P., Aigrain, S., Roberts, S., Evans, T. M., Osborne, M., & Pont, F. 2012, *MNRAS*, 419, 2683

Gillon, M., Demory, B.-O., Barman, T., Bonfils, X., Mazeh, T., Pont, F., Udry, S., Mayor, M., & Queloz, D. 2007, *A&A*, 471, L51

Gregory, P. 2005, *Bayesian Logical Data Analysis for the Physical Sciences* (New York, NY, USA: Cambridge University Press)

Harrington, J., Luszcz, S., Seager, S., Deming, D., & Richardson, L. J. 2007, *Nature*, 447, 691

Jenkins, J. M., Caldwell, D. A., & Borucki, W. J. 2002, *ApJ*, 564, 495

Knutson, H. A., Charbonneau, D., Allen, L. E., Burrows, A., & Megeath, S. T. 2008, *ApJ*, 673, 526

Knutson, H. A., Charbonneau, D., Cowan, N. B., Fortney, J. J., Showman, A. P., Agol, E., & Henry, G. W. 2009, *ApJ*, 703, 769

- Lewis, N. K., Knutson, H. A., Showman, A. P., Cowan, N. B., Laughlin, G., Burrows, A., Deming, D., Crepp, J. R., Mighell, K. J., Agol, E., Bakos, G. Á., Charbonneau, D., Désert, J.-M., Fischer, D. A., Fortney, J. J., Hartman, J. D., Hinkley, S., Howard, A. W., Johnson, J. A., Kao, M., Langton, J., & Marcy, G. W. 2013, *ApJ*, 766, 95
- Madhusudhan, N. & Seager, S. 2009, *ApJ*, 707, 24
- Mallat, S. 2008, *A Wavelet Tour of Signal Processing, Third Edition: The Sparse Way*, 3rd edn. (Academic Press)
- Mandel, K. & Agol, E. 2002, *ApJ*, 580, L171
- Moutou, C., Pont, F., Bouchy, F., & Mayor, M. 2004, *A&A*, 424, L31
- Nymeyer, S., Harrington, J., Hardy, R. A., Stevenson, K. B., Campo, C. J., Madhusudhan, N., Collier-Cameron, A., Loredó, T. J., Blečić, J., Bowman, W. C., Britt, C. B. T., Cubillos, P., Hellier, C., Gillon, M., Maxted, P. F. L., Hebb, L., Wheatley, P. J., Pollacco, D., & Anderson, D. R. 2011, *ApJ*, 742, 35
- Pont, F., Zucker, S., & Queloz, D. 2006, *MNRAS*, 373, 231
- Roberts, G., Gelman, A., & Gilks, W. 1997, *Annals of Applied Probability*, 7, 110
- Seager, S. & Deming, D. 2010, *ARA&A*, 48, 631
- Sivia, D. & Skilling, J. 2006, *Data Analysis: A Bayesian Tutorial*, 2nd edn. (Oxford University Press, USA)
- Southworth, J. 2008, *MNRAS*, 386, 1644
- Stevenson, K., Harrington, J., Nymeyer, S., Madhusudhan, N., Seager, S., Bowman, W. C., Hardy, R. A., Deming, D., Rauscher, E., & Lust, N. B. 2010, *Nature*, 464, 1161

- Stevenson, K. B., Harrington, J., Fortney, J. J., Loredó, T. J., Hardy, R. A., Nymeyer, S., Bowman, W. C., Cubillos, P., Bowman, M. O., & Hardin, M. 2012a, *ApJ*, 754, 136
- Stevenson, K. B., Harrington, J., Lust, N. B., Lewis, N. K., Montagnier, G., Moses, J. I., Visscher, C., Blečić, J., Hardy, R. A., Cubillos, P., & Campo, C. J. 2012b, *ApJ*, 755, 9
- ter Braak, C. 2006, *Statistics and Computing*, 16, 239, 10.1007/s11222-006-8769-1
- Winn, J. N., Holman, M. J., Bakos, G. Á., Pál, A., Johnson, J. A., Williams, P. K. G., Shporer, A., Mazeh, T., Fernandez, J., Latham, D. W., & Gillon, M. 2007, *AJ*, 134, 1707
- Winn, J. N., Holman, M. J., Torres, G., McCullough, P., Johns-Krull, C., Latham, D. W., Shporer, A., Mazeh, T., Garcia-Melendo, E., Foote, C., Esquerdo, G., & Everett, M. 2008, *ApJ*, 683, 1076
- Wornell, G. & Oppenheim, A. 1992a, *Signal Processing, IEEE Transactions on*, 40, 611
- . 1992b, *Information Theory, IEEE Transactions on*, 38, 785
- Wornell, G. W. 1993, *Proceedings of the IEEE*, 81, 1428
- . 1996, *Signal Processing with Fractals: A Wavelet-based Approach* (Upper Saddle River, NJ: Prentice Hall PTR)
- Zellem, R. T., Lewis, N. K., Knutson, H. A., Griffith, C. A., Showman, A. P., Fortney, J. J., Cowan, N. B., Agol, E., Burrows, A., Charbonneau, D., Deming, D., Laughlin, G., & Langton, J. 2014, *ApJ*, 790, 53

**CHAPTER 5: THE BAYESIAN ATMOSPHERIC RADIATIVE
TRANSFER CODE FOR EXOPLANET MODELING AND
APPLICATION TO THE EXOPLANET HAT-P-11b**

**Patricio Cubillos¹, Joseph Harrington¹, Jasmina Blečić¹, Patricio M. Rojo², Nate B. Lust¹,
Ryan C. Challener¹, M. Oliver Bowman¹, Madison M. Stemm¹, Austin J. Foster¹, Sarah D.
Blumenthal¹, Andrew S. D. Foster¹, Dylan K. Bruce¹, Emerson DeLarme¹, Justin Garland¹**

*¹Planetary Sciences Group, Department of Physics, University of Central Florida, Orlando, FL
32816-2385, USA*

²Department of Astronomy, Universidad de Chile, Santiago, Chile

*In preparation for *The Astrophysical Journal*.*

5.1 Abstract

This and companion papers (Harrington et al. 2015, Blecic et al. 2015b) present the Bayesian Atmospheric Radiative Transfer (BART) code, an open-source, open-development package to characterize extrasolar-planet atmospheres. BART combines a thermochemical-equilibrium abundances (TEA), a radiative-transfer (Transit), and a Bayesian statistical (MC^3) module to constrain atmospheric temperatures and molecular abundances for given spectroscopic observations. The TEA Python code calculates thermochemical-equilibrium mixing ratios for gaseous molecular species (Blecic et al. 2015a). Transit is an efficient one-dimensional line-by-line radiative-transfer C code, developed by P. Rojo and further modified by the UCF exoplanet group. This radiative code produces transmission and hemisphere-integrated emission spectra. Transit handles the HITRAN, Partridge & Schwenke's H_2O , Schwenke's TiO , and Plez's VO line-by-line opacity data; and cross-section opacities from HITRAN, ExoMol, and Borysow et al.. Transit emission-spectra models agree with models from C. Morley (priv. comm.) within a few percent. The statistical package, MC^3 , is a general-purpose, model-fitting Python code that implements the classical and differential-evolution Markov-chain Monte Carlo algorithms in a multiprocessor environment. We applied BART to the Spitzer and Hubble transit observations of the Neptune-sized planet HAT-P-11b. We reproduced the conclusions of Fraine et al. (2014), constraining the H_2O abundance and finding an atmosphere enhanced in heavy elements. The BART source code and documentation is available at <https://github.com/exosports/BART>.

5.2 Introduction

Transiting exoplanets offer the most favorable scenario to characterize exoplanet atmospheres; as planets pass in front of or behind their host stars, the observed flux reveals the planetary size and emission, respectively. Furthermore, the planned survey missions will use the transit method to find exoplanets around the brightest stars in the solar neighborhood (Ricker et al. 2014, Wheatley et al. 2013, Broeg et al. 2013). Based on the current estimates of the exoplanet occurrence rate in our galaxy (e.g., Bonfils et al. 2013, Fressin et al. 2013, Dressing & Charbonneau 2015), we expect to find thousands of planets.

Furthermore, we are expecting a profound transformation in the state of exoplanet characterization with the arrival of the James Webb Space Telescope (JWST). Thanks to its superior collecting area (25 m^2), spectral coverage ($\sim 0.6 - 28.0 \text{ }\mu\text{m}$), and resolving power ($R = 4 - 3000$), JWST will be able to characterize a broad range of exoplanet atmospheres, with unprecedented detail. Hopefully, future ground- and space-based telescopes will help to overcome the current limitations, and reveal the properties of exoplanets, from rocky Earth-like worlds (e.g., Jenkins et al. 2015) to hot gas giants.

5.2.1 Atmospheric Modeling and Retrieval

There are numerous physical processes that shape planetary atmospheres: radiative processes, scattering (e.g., Biddle et al. 2014), circulation dynamics (e.g., Showman et al. 2013), chemical kinetics (e.g., Agúndez et al. 2012), photochemistry (e.g., Moses et al. 2011), cloud physics (e.g., Fortney 2005), etc. In addition, exoplanet signals are intrinsically faint, and the current data are sparse and of low signal-to-noise ratios. Thus, to properly extract and interpret the data requires advanced and robust techniques.

The Bayesian retrieval approach provides an ideal framework to fit poorly-constrained models in a statistically-robust manner. A retrieval that uses Markov-chain Monte Carlo (MCMC) algorithms can determine the best-fitting model solution and the parameters' credible intervals. An MCMC draws a large number of samples from the parameters' phase space, generating a posterior distribution proportional to the likelihood of the model. In this process, the data drive the exploration towards the most-probable solutions; the data quality (i.e., the error bars) determines the credible region for the model parameters (\sim the span of the distribution). Modern MCMC algorithms enable more efficient and automated exploration than in the past (ter Braak 2006, ter Braak & Vrugt 2008).

In the exoplanet field, the retrieval approach was pioneered by Madhusudhan & Seager (2010). They parameterized the temperature profile and scaled thermochemical-equilibrium molecular abundances of H_2O , CH_4 , CO , and CO_2 . Then, other groups followed, implementing different modeling schemes. For example, Benneke & Seager (2012) implemented a self-consistent chemistry and radiative-transfer model, parameterizing the metallicity, carbon-to-oxygen ratio, internal heat, albedo, heat redistribution, diffusion, and cloud properties. Lee et al. (2012) introduced the optimal-estimation algorithm for exoplanet atmospheric modeling. Line et al. (2013) parameterized the thermal profile and constant-with-height molecular abundances. Waldmann et al. (2015) presented a retrieval code using pattern recognition and nested sampling.

The radiative-transfer equation links the observed spectra to the atmospheric properties. The temperature, pressure, and composition of the atmosphere determine the shape of the observed spectrum. We can distinguish particular atmospheric species, since each one imprints a characteristic absorption pattern in the spectrum. The atmospheric temperature, gravity, and mean molecular mass determine the atmospheric scale height, and thus modulate the amplitude of the spectral features. High-altitude haze layers can flatten a spectrum (e.g., Kreidberg et al. 2014, Knutson et al. 2014).

Although the physics behind the radiative processes is well understood, we lack laboratory data for absorption at temperatures above ~ 1200 K —most available opacity databases were conceived for Earth-like temperatures. Besides, it is still little understood how the different processes interact under each particular circumstance to determine the atmospheric composition. As a consequence, the atmospheric modeling parameterization widely differs from group to group. Ideally, as better-quality data permit more robust constraints, we will incorporate this information into the models, and will better understand the physics.

This work is part of a series of three papers introducing the open-source Bayesian Atmospheric Radiative Transfer (BART) package for exoplanet characterization. Here, we focus on the radiative-transfer treatment and the description of the statistical module. For additional details about the project, see the companion papers Harrington et al. (2015) and Blečić et al. (2015b). Section 5.3 introduces the BART modeling package. This section describes the radiative-transfer and the Bayesian statistical modules, and presents validation examples. Section 5.4 shows our retrieval analysis of the extrasolar planet HAT-P-11b using BART. Finally, Section 5.5 presents our prospects for the BART project and summarizes our conclusions.

5.3 The Bayesian Atmospheric Radiative Transfer Package

The BART package is a Python and C code that characterizes the atmospheres of astrophysical bodies for given spectroscopic data. BART uses a Bayesian approach to constrain the atmospheric properties in a statistically-robust manner. Following the ‘Reproducible Research’ principles (see further details in Harrington et al. 2015), this is an open-source, open-development project, available under version control at <https://github.com/exosports/BART>. In its conceived design, the code retrieves the temperature and abundance profiles of spectroscopically-active species (as in Madhusudhan & Seager 2010). Note that, although we describe BART in the context of exoplanet atmospheric retrieval, the code can be extended for other applications.

The BART package includes three self-sufficient modules: the one-dimensional radiative-transfer code (Transit), the Thermochemical-Equilibrium Abundances code (TEA, Blečić et al. 2015a), and the Multi-Core Markov-Chain Monte Carlo code (MC³, Cubillos et al. 2015). The repository includes a user manual that explains the features of the code, describes the code inputs and outputs, and provides sample runs. A second document aimed at developers, the code manual, details in depth the data structures, the file formats, and the code workflow.

Figure 5.1 illustrates the interaction between BART and its submodules. The BART program is divided into two main sections. The initialization section constructs a one-dimensional atmospheric model of the pressure, temperature, and species’ abundances. Adopting the pressure as the independent variable, BART calculates the temperature profiles implementing the three-stream Eddington approximation model (Line et al. 2013). For the abundances, the user can opt for thermochemical-equilibrium (through the TEA module, Blečić et al. 2015a), or set vertically uniform values.

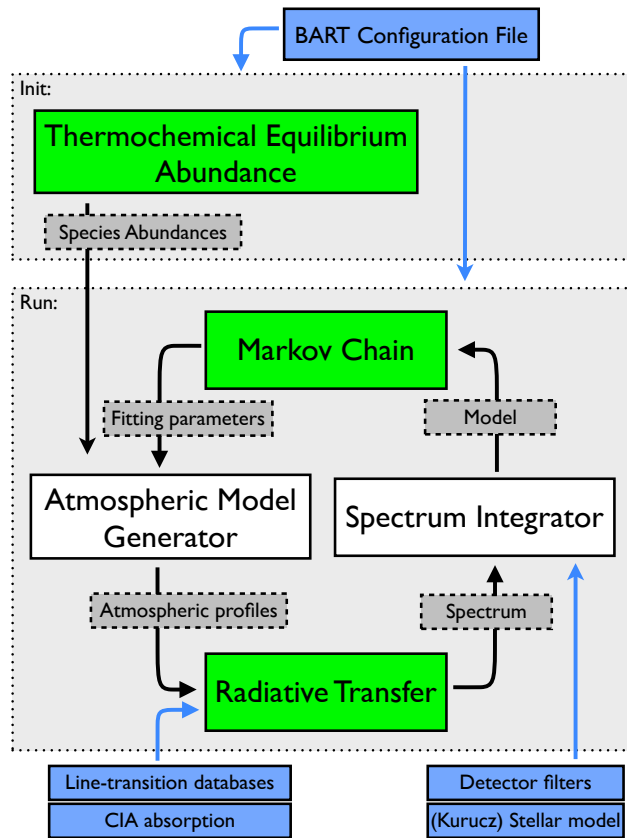


Figure 5.1: BART flow chart. The green boxes are the project’s submodules, the white boxes are additional BART routines, the blue boxes are input files, and the gray boxes are the data passed around. The BART configuration file sets up the parameters and inputs for all modules. The TEA module provides initial species’ abundance profiles for the atmospheric model. The statistical module drives the parameter exploration by drawing samples in a Markov-chain loop. The MCMC feeds the fitting parameters to the atmospheric model generator, which then computes the temperature, altitude, and abundance profiles. The radiative-transfer module calculates the planetary spectrum, which is later integrated over the bandpasses of the observations. The results are sent back to the MCMC, which compares them to the data and generates the set of fitting parameters for the next iteration.

After the initialization, BART samples the parameter phase space via a MCMC. First, MC³ draws a set of parameters that will define the atmospheric-model properties. Next, an atmospheric generator computes the temperature, abundance, and altitude of the atmospheric layers. Then, Transit calculates the spectrum for the given atmospheric model. After that, BART integrates the spectrum over the detector spectral-response filters. Finally, MC³ compares the filter-integrated values to the

data points (through χ^2 statistics) and generates a new set of fitting parameters. The data drives the parameter exploration through the Metropolis ratio. To estimate the parameters' credible region, the MCMC iterates this cycle thousands of times, populating the phase-space. The resulting posterior distribution of samples has a density proportional to the model probability. The following sections further detail the components of the BART code.

5.3.1 Thermochemical Equilibrium Abundance Module

The Python TEA code (Blecic et al. 2015a) calculates the mole mixing ratios (abundances) of atomic and molecular gaseous species under thermochemical equilibrium. TEA implements the methodology of White et al. (1958) and Eriksson (1971); given the elemental abundances, temperature, and pressure values, TEA minimizes the Gibbs free-energy of the system in an iterative, Lagrangian-optimization scheme.

Using TEA, Blecic et al. (2015a) successfully reproduced results from Burrows & Sharp (1999), the Chemical Equilibrium with Applications (CEA) code, and White et al. (1958). The TEA code and documentation are available at <https://github.com/dzesmin/TEA> under an open-source license.

BART uses the TEA module to calculate initial atmospheric abundances, for an initial, user-defined temperature profile. These initial profiles are used as the base to scale and explore different atmospheric abundances (see Sec. 5.3.2.2).

5.3.2 Atmospheric Model Generator

The model generator connects the statistical-driver with the radiative-transfer module. This module receives the free parameters, computes the corresponding atmospheric profiles (temperature, altitude, and abundances), and feeds the profiles to Transit. The temperature and altitude profiles are calculated from the given physical properties and model parameters, whereas the abundance profiles are calculated by scaling the input initial abundance profiles with the model free parameters (scaling factors).

5.3.2.1 Temperature Profile

The temperature profiles are calculated by applying the three-stream Eddington-approximation model of Line et al. (2013), which is a variation of the model of Parmentier & Guillot (2014). This model considers two heat sources, the internal planetary energy (infrared), and the incident stellar irradiation (optical). The energy transfer is modulated by an infrared and two optical streams, each one parameterized by a Plank mean opacity; in practice, the thermal stream is parameterized by the Plank mean thermal opacity, κ , whereas the optical streams are parameterized by the optical-to-infrared ratio of the mean opacities: γ_1 and γ_2 .

A parameter β modulates the absorbed stellar energy, working as a proxy for the albedo and day-to-night energy-redistribution factor. The input stellar irradiation is characterized by the temperature:

$$T_{\text{irr}} = \beta \left(\frac{R_s}{2a} \right)^{1/2} T_s, \quad (5.1)$$

where T_s and R_s are the stellar temperature and radius, respectively, and a is the orbital semi-major axis. A β value of unity corresponds to a planet with zero albedo and efficient energy redistribution.

The internal heat is characterized by an internal temperature, T_{int} .

The temperature at each pressure layer, p , is then given by:

$$T^4(p) = \frac{3T_{\text{int}}^4}{4} \left(\frac{2}{3} + \tau \right) + \frac{3T_{\text{irr}}^4}{4} (1 - \alpha) \xi_1(\tau) + \frac{3T_{\text{irr}}^4}{4} \alpha \xi_2(\tau), \quad (5.2)$$

with

$$\xi_i(\tau) = \frac{2}{3} + \frac{2}{3\gamma_i} \left[1 + \left(\frac{\gamma_i \tau}{2} - 1 \right) \exp(-\gamma_i \tau) \right] + \frac{2\gamma_i}{3} \left(1 - \frac{\tau^2}{2} \right) E_2(\gamma_i \tau), \quad (5.3)$$

where $\tau(p) = \kappa p/g$ is the thermal optical depth for the given atmospheric gravity, g ; $E_2(\gamma_i \tau)$ is the second-order exponential integral; and the parameter α partitions the flux between two optical streams. Since the internal flux has little impact on the spectra, T_{int} is fixed during the MCMC for our runs; the free parameters are then: κ , γ_1 , γ_2 , α , and β .

5.3.2.2 Molecular-Abundance Profiles

The code modifies the atmospheric composition by scaling the entire initial abundance profile with the abundance free parameter (f_X) for selected species X . Let $q_X^0(p)$ be the initial abundance profile at pressure p , then the modified abundances are calculated as:

$$q_X(p) = q_X^0(p) \times 10^{f_X}. \quad (5.4)$$

Since the abundances may vary over several orders of magnitude, the abundance free parameters modify the log-scale abundances. To preserve the total mixing ratio at 1.0, the code adjusts the abundances of H_2 and He at each layer (keeping the H_2/He abundance ratio constant).

By randomly scaling the abundances, the code can explore disequilibrium compositions. The user can define which atmospheric species vary their abundances. H_2O , CH_4 , CO , and CO_2 are the most-abundant spectroscopically-active species that shape the infrared spectrum. These are the standard species included in most exoplanet retrievals (e.g., Madhusudhan & Seager 2009, Line et al. 2013, Waldmann et al. 2015).

5.3.2.3 Altitude – Pressure

BART calculates the altitude (the radius) for each layer using the hydrostatic-equilibrium equation:

$$\frac{dp}{dz} = -\rho g, \quad (5.5)$$

where p , z , and ρ are the pressure, altitude, and mass density of the layers, respectively, and g is the atmospheric gravity.

For eclipse geometry, the emission spectrum depends on the relative altitude between the layers (Δz); however, for transit geometry, the transmission spectrum depends on the absolute altitude of the layers. Thus, in this case, the code fits for the radius at a fiducial pressure level (0.1 bar by default, but adjustable by the user).

5.3.3 Radiative Transfer

The radiative-transfer equation describes how light propagates as it travels through a medium. Let the specific intensity, I_ν , denote the power carried by rays per unit area, dA , per unit wavenumber, ν , in the interval $d\nu$ within a solid angle $d\Omega$. Then, the radiative-transfer equation for the specific intensity is given by:

$$\frac{dI_\nu}{ds} = -e_\nu(I_\nu - S_\nu), \quad (5.6)$$

where s is the path traveled by the light ray, e_ν is the atmospheric opacity, and S_ν is the source function (the intensity contributed by the atmosphere into the beam). The opacity depends on the atmospheric composition, pressure, and temperature.

The observed flux is the integral of the intensity over the solid angle. Therefore, by solving the radiative-transfer equation for the given observing geometry, we can model the observed transit and eclipse depths as a function of wavelength.

The Transit module solves the one-dimensional radiative-transfer equation for two relevant cases of exoplanet observations: the transmission spectrum for transit observations, and the hemisphere-integrated emission spectrum for eclipse observations. The model assumes hydrostatic balance, local thermodynamic equilibrium, and ideal gas law. The opacity comes from electronic, rotational, and vibrational line-transition absorptions (hereafter, simply called “line transitions”) and collision-induced absorption (CIA). Transit requires as inputs: (1) a configuration file that indicates the wavenumber sampling, observing geometry, input files, etc.; (2) a one-dimensional atmospheric model that specifies the atmospheric composition and the pressure, altitude, temperature, and species abundances of each layer; and (3) line-by-line and/or cross-section opacity files. The code was originally developed at Cornell University by Patricio Rojo, as part of his dissertation project with Joseph Harrington (Rojo 2006). Transit is a C, modular, object-oriented code, wrapped with SWIG¹ for use in Python. Our version of Transit is an open-source project hosted at <https://github.com/exosports/transit>.

The Transit program divides the spectrum calculation into two main sections: initialization and run (Figure 5.2). Once Transit executes the initialization, it can produce multiple spectrum models, updating the atmospheric model each time.

¹swig.org/

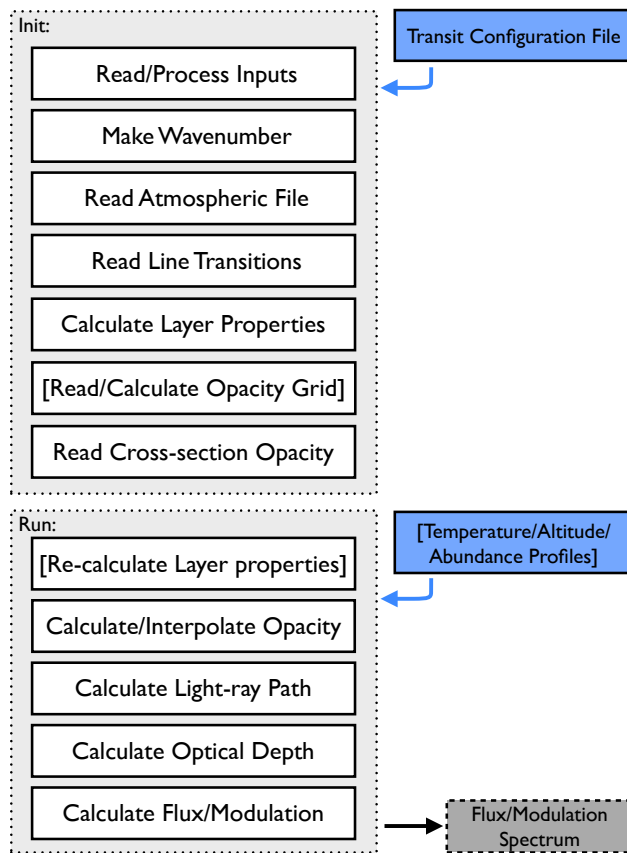


Figure 5.2: Transit flow chart. The white boxes denote the main routines, the blue boxes the code inputs, and the gray box the output spectrum file. The items in brackets are optional. Transit consists of two main blocks of code, initialization (read input files) and run (evaluate spectrum). The code sequentially executes the routines from the top down. When used for BART, the initialization block is executed once at the beginning of the run. Then, BART executes the spectrum-calculation block for each iteration of the Markov chain.

The first section of Transit reads and processes the input files. The routines in this section (1) read the configuration file, (2) create the (equi-spaced) wavenumber array, (3) read the atmospheric-model and line-transition opacity files, (4) calculate the density and altitude of the atmospheric layers, along with the partition function of the species, (5) compute or read a tabulated opacity grid (optional), and (6) read cross-section opacity files.

The opacity grid is a four-dimensional table of precomputed opacities. This table contains the opacities (in $\text{cm}^2 \text{gr}^{-1}$) evaluated over the wavenumber array, at each atmospheric pressure level, for a grid of temperatures, and for each absorbing species. The opacity grid speeds up the spectrum evaluation allowing Transit to interpolate the opacities from the table, instead of repeatedly computing the line-by-line calculations.

The second section of Transit computes the emission or transmission spectrum. This section's routines (1) update the atmospheric model (optional), (2) compute the opacity, either interpolating from the opacity grid or from line-by-line calculations, (3) calculate the light-ray path, (4) integrate the opacity over the ray paths to obtain the optical depth, and (5) calculate the intensity and flux spectra. The following sections further detail the spectral calculations, the opacity calculations, and the available databases.

5.3.3.1 *Transit Geometry*

During a transit event (Fig. 5.3) the planet blocks a fraction of the stellar light, which is proportional to the planet-to-star area ratio, R_p^2/R_s^2 . Since each species imprints a characteristic absorbing pattern as a function of wavelength, the planetary atmosphere modulates the transmission (or modulation) spectrum:

$$M_\nu = \frac{F_{\nu,O} - F_{\nu,T}}{F_{\nu,O}}, \quad (5.7)$$

where $F_{\nu,T}$ and $F_{\nu,O}$ are the observed fluxes during transit and out of transit, at wavenumber ν .

For transmission geometry, the planetary emission is small compared to the stellar intensity. Then, we can neglect the source-function term from Equation (5.6):

$$\frac{dI_\nu}{ds} = -e_\nu I_\nu. \quad (5.8)$$

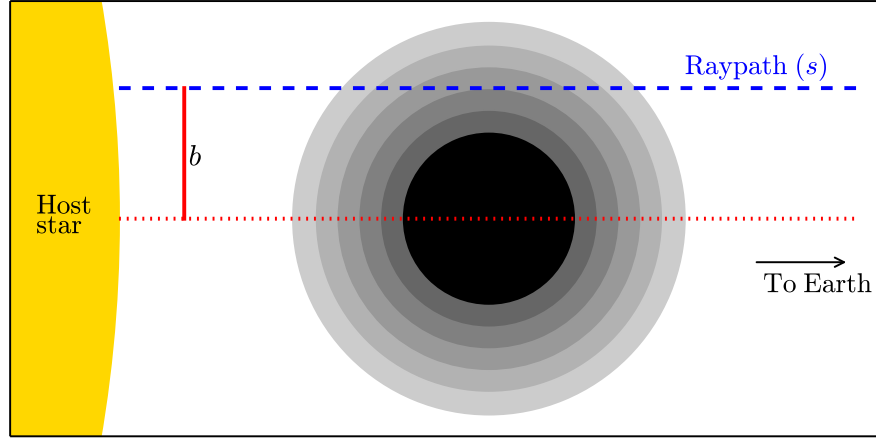


Figure 5.3: Transit-geometry observation diagram. The atmospheric model consists of a set of one-dimensional spherically-symmetrical shells (gray gradient) around the planet center (black). Given the geometry of the observation, all the observed light rays (e.g., blue dashed line) travel parallel to each other and, hence, the optical depth for each ray depends exclusively on the impact parameter (b) of the ray path.

Let I_ν^0 be the stellar specific intensity. By defining the optical depth along the path as:

$$\tau_\nu = \int_{\text{path}} e_\nu ds, \quad (5.9)$$

the solution for the transmission radiative-transfer equation becomes:

$$I_\nu = I_\nu^0 e^{-\tau_\nu}. \quad (5.10)$$

The specific flux, F_ν , is the integral of the specific intensity in the direction of the observer over the solid angle, $d\Omega$:

$$F_\nu = \int I_\nu \cos\theta d\Omega, \quad (5.11)$$

where θ is the angle between the ray beams and the normal vector of the detector. Since the distance from Earth to the system, d , is much larger than the distance from the star to the planet, the stellar radius, and the planetary radius ($d \gg a$, $d \gg R_s$, and $d \gg R_p$, respectively), we can assume that the observed rays travel in a parallel beam thorough the planetary atmosphere. Then, we can rewrite the solid-angle integral as an integral over the projected disk of the system:

$$F_\nu = \frac{2\pi}{d^2} \int_0^{R_s} I_\nu r dr. \quad (5.12)$$

For the out-of-transit flux, Equation (5.12) gives:

$$F_{\nu,O} = \pi I_\nu^0 \left(\frac{R_s}{d} \right)^2. \quad (5.13)$$

For the in-transit flux, we assume that the planetary atmosphere is a set of spherically-symmetrical homogeneous layers (Fig. 5.3). Then, the optical depth becomes a function of the impact parameter of the light ray, b : $\tau_\nu = \tau_\nu(b)$.

Consider now a planetary altitude, R_{top} , high enough such that $e^{-\tau_\nu(R_{\text{top}})} \approx 1$ (in practice, the top layer of the atmospheric model). In addition, we neglect the variation of limb-darkening over the projected area of the planet onto the star, and we correct the limb-darkening factor for the measured transit depth. Then, the in-transit specific flux becomes:

$$F_{\nu,T} = \frac{2\pi}{d^2} \int_0^{R_s} I_\nu^0 e^{-\tau_\nu(b)} r dr, \quad (5.14)$$

$$= \frac{2\pi}{d^2} I_\nu^0 \left[\int_0^{R_{\text{top}}} e^{-\tau_\nu} b db + \frac{R_s^2 - R_{\text{top}}^2}{2} \right]. \quad (5.15)$$

Finally, substituting Equations (5.13) and (5.15) into (5.7), we calculate the modulation spectrum as:

$$M_\nu = \frac{1}{R_s^2} \left[R_{\text{top}}^2 - 2 \int_0^{R_{\text{top}}} e^{-\tau_\nu} b db \right]. \quad (5.16)$$

5.3.3.2 Eclipse Geometry

An eclipse event reveals the planetary day-side emission. The Transit eclipse-geometry code (mainly implemented by J. Blecic) solves the radiative-transfer equation to obtain the emerging intensity at the top of the atmosphere. For this case, we adopt the plane-parallel approximation (Fig. 5.4), which models the atmosphere as a stratified set of plane horizontal homogeneous layers. Additionally, we adopt the Local Thermodynamic Equilibrium approximation, where the source function becomes the Planck function $B_\nu(T)$.

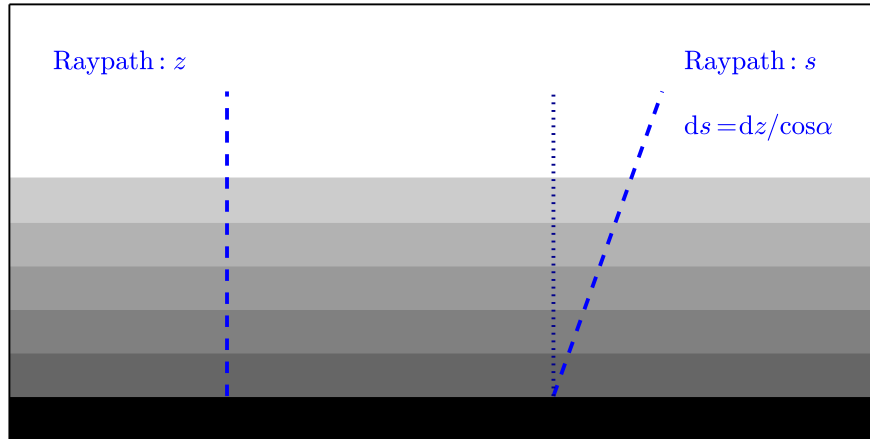


Figure 5.4: Diagram for eclipse-geometry observation. The atmospheric model consists of a set of plane-parallel layers (gray gradient) above the center of the planet (black). Transit calculates the emerging intensity along a set of paths (blue dashed lines) with a given incident inclination with respect to the normal vector of the planet, α .

Let $d\tau_{\nu,z} = -e_{\nu}dz$ be the vertical optical depth (with origin $\tau = 0$ at the top of the atmosphere). The path (ds) of a ray with an angle α , with respect to the normal vector, is related to the vertical path as: $ds = dz/\cos \alpha \equiv dz/\mu$. Then, the radiative-transfer equation becomes:

$$-\mu \frac{dI_{\nu}}{d\tau_{\nu,z}} = -I_{\nu} + S_{\nu}, \quad (5.17)$$

which can be rewritten as:

$$-\mu \frac{d}{d\tau_{\nu,z}} (I_{\nu} e^{-\tau_{\nu,z}/\mu}) = S_{\nu} e^{-\tau_{\nu,z}/\mu}. \quad (5.18)$$

Transit calculates the emergent intensity by integrating Equation (5.18) from the deep layers to the top of the atmosphere. At depth, the atmosphere is optically thick ($\tau = \tau_b \gg 1$), such that $\exp(-\tau_b/\mu) \rightarrow 0$. Therefore, the intensity at the top of the atmosphere is given by:

$$I_{\nu}(\tau = 0, \mu) = \int_0^{\tau_b} B_{\nu} e^{-\tau/\mu} d\tau/\mu. \quad (5.19)$$

By changing variables from the angle θ to the angle on the planet hemisphere, α (related by: $d \sin \theta = R_p \sin \alpha$), the emergent flux (Eq. 5.11) becomes:

$$F_{\nu} = \left(\frac{R_p}{d} \right)^2 \int_0^{2\pi} \int_0^{\pi/2} I_{\nu} \cos(\alpha) \sin(\alpha) d\alpha d\phi \quad (5.20)$$

$$= 2\pi \left(\frac{R_p}{d} \right)^2 \int_0^1 I_{\nu} \mu d\mu. \quad (5.21)$$

Transit approximates this integral by summing over a discrete set of angles:

$$F_{\nu} \approx \pi \left(\frac{R_p}{d} \right)^2 \sum_i \langle I_{\nu}(\mu_i) \rangle \Delta\mu_i^2. \quad (5.22)$$

Additionally, Transit approximates the average intensity in each angle interval by the intensity of the mean angle, $\langle I_\nu(\mu) \rangle \approx I_\nu(\langle \mu \rangle)$. Transit computes $I_\nu(\langle \mu \rangle)$ through a Simpson numerical integration of Equation (5.19) and then returns the surface emergent flux:

$$F_\nu^{\text{surf}} \approx \pi \sum_i \langle I_\nu(\mu_i) \rangle \Delta\mu_i^2. \quad (5.23)$$

5.3.3.3 *Collision-induced Absorption*

Collision-induced absorption is one of the main sources of atmospheric opacity. Sec. 5.3.3.5 details how Transit incorporate the CIA calculations. CIA occurs when particles without an intrinsic electric dipole moment collide. The collisions induce a transient dipole moment, which allows dipole transitions. The short interaction time of the collisions broadens the line profiles, generating a smooth CIA spectrum. The CIA opacity scales with the density of the colliding species, and thus becomes more relevant at the deeper, higher-pressure layers of the atmosphere (Sharp & Burrows 2007). For gas-giant planets, the two most important CIA sources are H₂–H₂ and, to a lesser extent, H₂–He collisions.

5.3.3.4 *Line-transition Absorption*

A species absorbs or emits photons at specific wavelengths, corresponding to the characteristic energies between its electronic, rotational, and vibrational transitions, giving rise to line-transition opacities. The atmospheric temperature and pressure determine the strength and shape of a species' line transitions.

Transit calculates the line-transition opacity, e_ν , in a line-by-line scheme, adding the contribution from each broadened line-transition, j :

$$e_\nu = \sum_j S_j V(\nu - \nu_j), \quad (5.24)$$

where ν_j is the wavenumber of the line transition, S_j is the line strength (in cm^{-2}), and V is the line profile (Voigt). The line strength is given by:

$$S_j = \frac{\pi e^2}{m_e c^2} \frac{(gf)_j}{Z_i(T)} n_i \exp\left(-\frac{hcE_{\text{low}}^j}{k_B T}\right) \left\{ 1 - \exp\left(-\frac{hc\nu_j}{k_B T}\right) \right\}, \quad (5.25)$$

where gf_j and E_{low}^j are the weighted oscillator strength and lower state energy level (in cm^{-1}) of the line transition, respectively; Z_i and n_i are the partition function and number density of the isotope i , respectively; T is the atmospheric temperature; e and m_e are the electron's charge and mass, respectively; c is the speed of light, h is Planck's constant; and k_B is the Boltzmann's constant.

The Voigt profile considers the Doppler and the Michelson-Lorentz collision broadening. The Doppler and Lorentz half-widths at half maximum (HWHM, Goody 1995) are, respectively:

$$\alpha_d = \frac{\nu_j}{c} \sqrt{\frac{2k_B T \ln 2}{m_i}}, \quad (5.26)$$

$$\alpha_l = \frac{1}{c} \sum_a n_a d_a^2 \sqrt{\frac{2k_B T}{\pi} \left(\frac{1}{m_i} + \frac{1}{m_a} \right)} \quad (5.27)$$

where m_i is the mass of the absorbing species and d_a is the collision diameter between the interacting particles. The sum goes over all species, a , in the atmosphere. Transit pre-computes, during the initialization section, a set of Voigt profiles (following the algorithm of Pierluissi 1977) for a grid of Doppler and Lorentz HWHM.

The Transit code implements a series of steps to improve the performance of the line-by-line opacity calculation (Eq. 5.24). When multiple lines of a same isotope fall in the same wavenumber bin, the code adds the line strengths before broadening the line over the wavenumber array—note that the line-strength calculation is fast compared to the Voigt-profile broadening. Additionally, a line-strength cutoff (a user-adjustable parameter) prevents the computation of the weaker lines that do not contribute significantly. Our cutoff is relative to the largest line strength in each layer instead of the fixed-temperature cutoff of previous works (e.g., Sharp & Burrows 2007, Line et al. 2012) because of the large strength variation with temperature. Lastly, Transit automatically adjusts the wavenumber sampling at each layer to avoid under- or oversampling the line profiles.

5.3.3.5 Opacity Databases

The CIA input files of Transit (cross-section opacity files) are ASCII tables of the opacity (in units of $\text{cm}^{-1}\text{amagat}^{-2}$, with $1 \text{ amagat} = n_0 = 2.68679 \times 10^{19} \text{ molecules cm}^{-3}$) as a function of wavenumber and temperature. Transit provides Python scripts to reformat the CIA data files given by A. Borysow² and HITRAN (Richard et al. 2012) into its internal format.

To evaluate the CIA opacity in the atmosphere, Transit performs a bicubic interpolation (wavenumber and temperature) from the tabulated CIA opacities ($e_{\text{cia}}^{\text{t}}$), and scales the values to units of cm^{-1} (e_{cia}), multiplying by the number density of the species:

$$e_{\text{cia}} = e_{\text{cia}}^{\text{t}} \frac{n_1 n_2}{n_0 n_0}, \quad (5.28)$$

²astro.ku.dk/~aborysow/programs

where n_1 and n_2 are the number densities of the colliding species (in units of molecules cm^{-3}). Figure 5.5 shows Transit emission spectra for pure H_2 – H_2 and H_2 – He CIA opacities. When compared against the models of C. Morley (priv. comm.), we agree to better than 0.5%. We also noted that the HITRAN absorption is weaker than the Borysow absorption, producing emission spectra 2%–8% stronger for this atmospheric model.

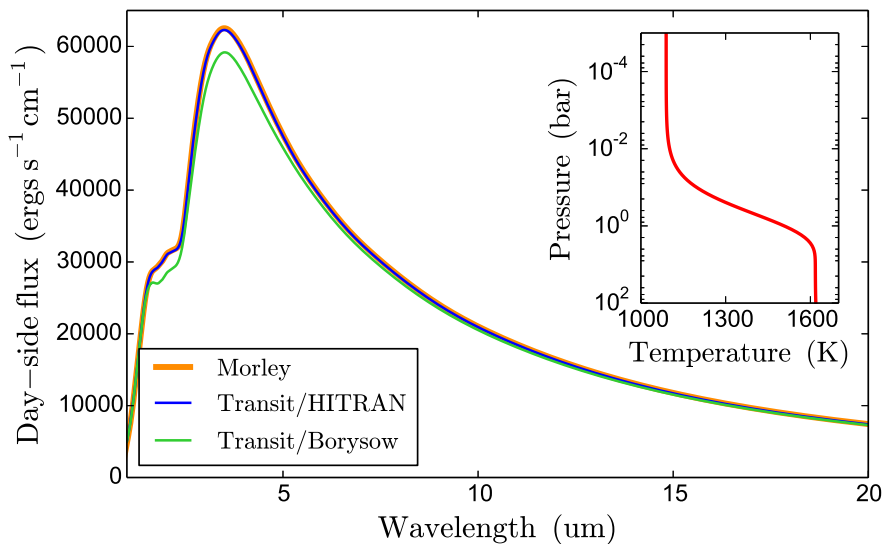


Figure 5.5: Model emission spectra for pure collision-induced absorption. The blue and green curves show the Transit spectra for HITRAN and Borysow CIA opacities, respectively. The orange curve shows the HITRAN CIA spectrum of C. Morley. All spectra were calculated for an atmospheric model with uniform mole mixing ratios composed of 85% H_2 and 15% He , for a planet with a $1 R_{\text{Jup}}$ radius and a surface gravity of 22 m s^{-2} . The inset shows the atmospheric temperature profile as a function of pressure.

Transit treats the cross-section line-transition opacity inputs in a similar manner as the CIA data files, except that the opacity is given in $\text{cm}^{-1}\text{amagat}^{-1}$ units. Transit provides a routine to re-format HITRAN and ExoMol³ cross-section data files into the format required by Transit.

³ <http://exomol.com/data/data-types/xsec>

Transit stores the line-by-line opacity data into a Transit Line Information (TLI) binary file. A TLI file contains a header and the line-transition data. The header contains the number and names of databases, species, and isotopes, and the partition function per isotope as a function of temperature. The line-transition data consist of four arrays with the transition's wavelength, lower-state energy, oscillator strength, and isotope ID. The original Transit line-reading code has been rewritten in Python to make it easier for users to add functions to read additional line-list formats. As of this writing, the Transit line reader can process line-transition files from the HITEMP/HITRAN lists (Rothman et al. 2010, 2013), the H₂O list from Partridge & Schwenke (1997), the TiO list from Schwenke (1998), and the VO list from B. Plez (priv. comm.).

Most line-by-line databases provide tabulated partition-function files. For the HITRAN and HITEMP databases, Transit provides an adaptation⁴ of the Total Internal Partition Sums code⁵ (TIPS, Laraia et al. 2011).

Figure 5.6 shows an example of the emission spectra of H₂O, CO, CO₂, and CH₄. A comparison with the Morley models shows a good agreement for all four cases. Figure 5.7 shows an example of the TiO and VO opacity spectra. The Transit spectra agree with that of Sharp & Burrows (2007).

⁴<https://github.com/pcubillos/ctips>

⁵http://faculty.uml.edu/robert_gamache/software/index.htm

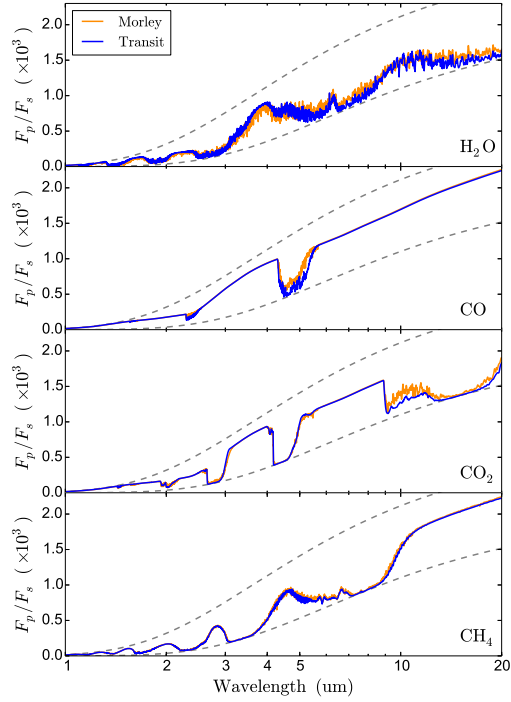


Figure 5.6: Model planet-to-star flux ratio spectra for water, carbon monoxide, carbon dioxide, and methane (top to bottom panels). The blue and orange solid curves show the Transit and the Morley radiative-transfer spectra, respectively (Gaussian-smoothed for better visualization). The planetary atmospheric model is the same as in Fig. (5.5), with additional uniform mixing ratios of 10^{-4} for the respective species in each panel. The stellar model corresponds to a blackbody spectrum of a $1 R_{\odot}$ radius and 5700 K surface-temperature star. The dashed grey lines indicate the flux ratio for planetary blackbody spectra at 1090 and 1620 K (atmospheric maximum and minimum temperatures). The CIA opacity comes from Richard et al. (2012). For H_2O and CH_4 both models used the line lists from (Partridge & Schwenke 1997) and Yurchenko & Tennyson (2014), respectively. For CO, the Morley models used the line list from Goorvitch (1994), whereas Transit used the HITEMP line list (which is based on the Goorvitch line list). For CO_2 , Morley used Huang et al. (2013) and Huang et al. (2014), whereas Transit used HITEMP. The largest differences correspond to CO and CO_2 , the molecules that correspond to different databases. There are also some differences in the H_2O spectrum.

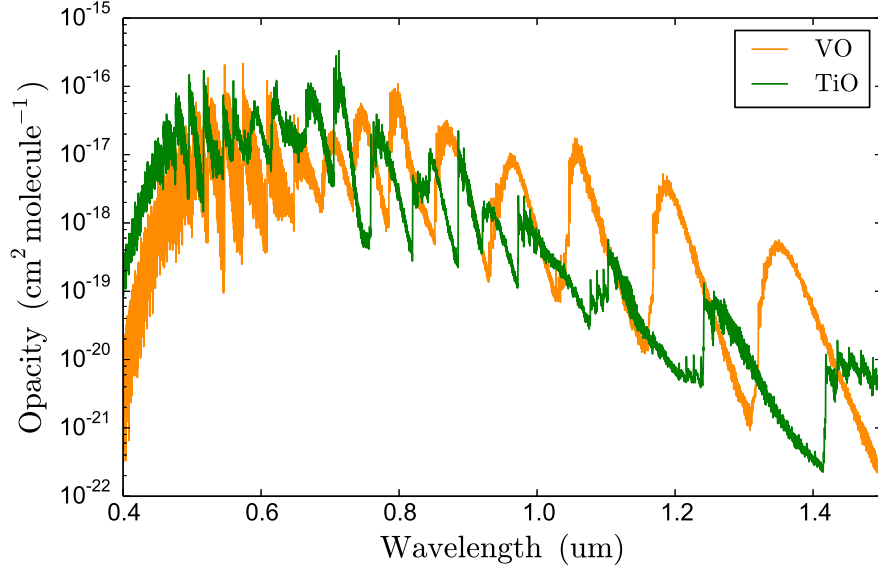


Figure 5.7: Near-infrared titanium- and vanadium-oxide opacity spectra. Transit calculated the opacities at a temperature of 2200 K and a pressure of 10.13 bar (10 atm). Our models are consistent with Figures (4) and (5) of Sharp & Burrows (2007).

5.3.4 Spectrum Band Integration

To compare the model spectra to the data, BART integrates the spectra over the detector transmission filters (also called filter bands). The filters describe the spectral response curve for each observing band. For transit geometry, the observed transit depths are directly compared to the band-integrated transmission spectra. On the other hand, for eclipse geometry, the observed eclipse depths correspond to the planet-to-star flux ratio:

$$F_p/F_s = \frac{F_p^{\text{surf}}}{F_s^{\text{surf}}} \left(\frac{R_p}{R_s} \right)^2, \quad (5.29)$$

where F_p^{surf} is the surface flux spectrum of the star. BART incorporates the Kurucz models for the stellar spectra (Castelli & Kurucz 2004).

5.3.5 *Statistical MCMC Driver*

To drive the MCMC exploration, BART uses the open-source module, Multi-Core Markov-Chain Monte Carlo (MC³, Cubillos et al. 2015), hosted at <https://github.com/pcubillos/MCcubed>. MC³ is a general-purpose, model-fitting software. The code is written in Python with several C-code extensions, and has parallel multiprocessor capacity. To explore the parameter phase space, BART uses the Differential-Evolution Markov-chain Monte Carlo algorithm (DEMC, ter Braak 2006) implemented in MC³.

The posterior in the Metropolis-Hastings acceptance rule can take uniform non-informative, Jeffrey's non-informative, or Gaussian informative priors. MC³ checks for the MCMC convergence via the Gelman & Rubin (1992) statistics. An MC³ run returns the sampled parameter posterior distribution, the best-fitting values, the limits of the 68% credible region, and the acceptance rate. At the end of the MCMC run, the program produces several plots to help visualize the results. Trace plots show the sequence of values along the MCMC iterations for each free parameter. Marginal-posterior plots show the posterior probability distribution for each free parameter. Pairwise-posterior plots show the two-dimensional posterior distribution for all the combinations of free-parameter pairs. These plots help to identify non-convergence, multi-modal posteriors, correlations, or incorrect priors.

5.3.5.1 MC^3 Usage for BART

BART and MC^3 implement the same configuration-file format, allowing the user to define all parameters in a single file. The BART code runs best on multiple processors. BART includes a modified worker program that allows the code to separate the initialization from the MCMC-loop code (see Sec. 5.3). This worker routine is comprised of the atmospheric model generator, the run section of Transit (see Fig. 5.3), and the spectrum integrator. During the MCMC loop, the data transferred through MPI are the free-parameter values and the simulated observations obtained by band-integrating the model spectra (see Fig. 5.1). The line-by-line opacity calculation in Transit is the most computationally demanding task (typically 95% of the run time). Thus, a BART run avoids this step by using an opacity table, either loaded or calculated during the initialization. Transit running times vary largely depending on the CPU performance and modeling configuration.

5.3.6 Retrieval Validation Test

In this section, we applied the BART analysis to synthetic observations to test the retrieval code. We generated an atmospheric model for a hot-Jupiter planet with the characteristics of the system HD 209458. The system parameters are $R_p = 1.35 R_{\text{Jup}}$, $R_s = 1.145 R_{\odot}$, and $T_s = 6075$ K. Figure 5.8, right panel, shows the input temperature-pressure profile (red curve). TEA calculated the thermochemical-equilibrium abundances for this atmospheric model, given solar elemental abundances (Asplund et al. 2009).

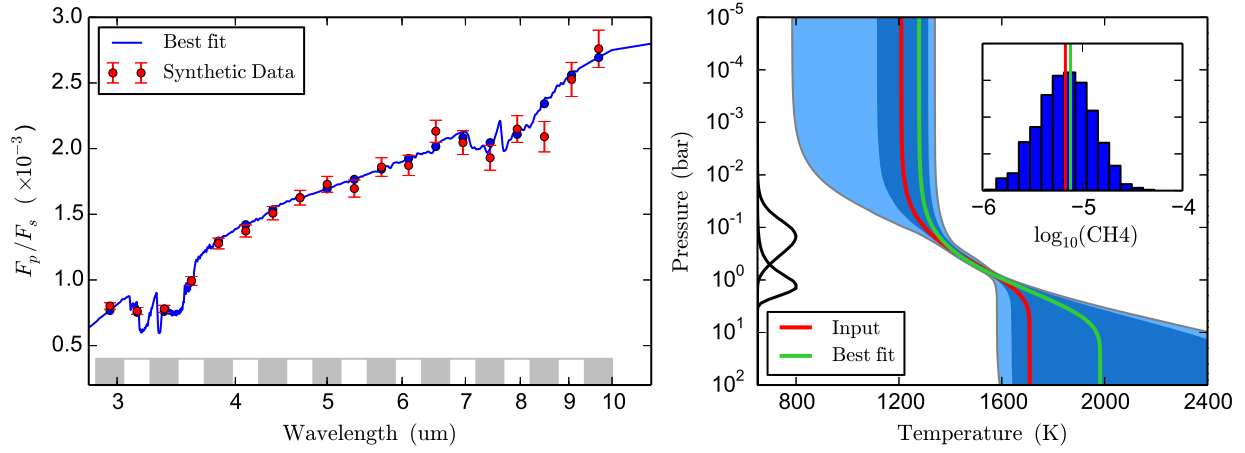


Figure 5.8: BART retrieval for a synthetic model spectrum. The left panel shows the planet-to-star flux ratio for a synthetic observation (red points with error bars) and the retrieved best-fitting model (blue curve). The bottom gray/white boxes show the filter bands for each data point. The right panel shows the retrieved temperature profile and methane-abundance posteriors. The dark- and light-blue shaded areas show the 68% and 95% credible regions, respectively. The black solid curves on the left show two typical contribution functions for this simulation (for further details, see Blečić et al. 2015b). The inset shows the posterior histogram for the methane abundance scale factor.

The atmospheric model considered the opacities only from H₂-H₂ and H₂-He CIA (Richard et al. 2012), and CH₄ line transitions (Rothman et al. 2013). We generated a synthetic emission spectrum, with $\sim 6\times$ enhanced methane abundance, over the 2–10 μm range (the range covered by the Spitzer’s Infrared Array Camera detectors). We integrated the spectrum over 19 synthetic broad filter bands to generate the synthetic observations. We further added Poisson noise to the synthetic datapoints, giving a signal-to-noise ratio of 26 per point on average.

We configured BART to retrieve the methane abundance and a simplified version of the three-stream Eddington-approximation temperature model. We kept α fixed at a value of 0.0, which gives zero weight to the stream controlled by γ_2 . Thus, only $\log \kappa$, $\log \gamma_1$, and β remained as fitting parameters. Figure 5.8 shows the retrieval results and the input models. The best-fitting model and the posterior distributions of the temperature profile and the CH_4 abundance agree with the input values to within the 68% credible region. The better constrained region of the atmosphere (around 1 bar) agrees well with the peak of the contribution curves for these observing bands (the altitude where the atmosphere changes from optically thin to optically thick).

5.4 Application to HAT-P-11b

In this section we analyzed the transit observations of the Neptune-sized planet HAT-P-11b. We re-analyzed the Spitzer data, retrieved the planet’s atmospheric properties, and compared our results to the similar analysis by Fraine et al. (2014, hereafter F14).

The exoplanet HAT-P-11b (Bakos et al. 2010) is slightly larger than Neptune in mass ($26 M_{\oplus}$) and radius ($4.7 R_{\oplus}$). The planet orbits a K4 dwarf star ($R_s = 0.75 R_{\odot}$, $T_s = 4780$ K), at a distance of 0.053 AU, with a period of 5 days. Given these parameters, the planetary equilibrium temperature (temperature at which the emission as blackbody balances the absorbed energy, assuming zero albedo and efficient heat redistribution) is $T_{\text{eq}} = 878$ K.

F14 observed transits of HAT-P-11b with the Hubble Space Telescope’s (HST) Wide Field Camera 3 (WFC3) and the Spitzer’s Infrared Array Camera (IRAC) 3.6 and 4.5 μm bands. The WFC3 spectroscopic data covers the 1.1 to 1.7 μm region of the spectrum with a spectral resolution of ~ 75 . F14 obtained Kepler Space Telescope data concurrently with the Spitzer observations, allowing them to model star spots on the surface of the star. F14 characterized the atmospheric composition with the Self-Consistent Atmospheric Retrieval Framework for Exoplanets (SCARLET) tool (Benneke 2015). They detected water absorption features and estimated a best-fitting metallicity of 190 times the solar metallicity.

Note, however, that the activity of the host star may introduce a variation in the observed transit depths at different epochs. Although F14 estimated a transit depth uncertainty of 51 p.p.m., their best-fitting offset between the WFC3 and Spitzer data was ~ 93 p.p.m.

5.4.1 Analysis of the Spitzer Data

We re-analyzed the HAT-P-11b Spitzer transmission light curves with our Photometry for Orbits, Eclipses, and Transits (POET) pipeline (Stevenson et al. 2010, 2012a,b, Campo et al. 2011, Nymeyer et al. 2011, Cubillos et al. 2013, 2014). The Spitzer Space Telescope (warm-mission) obtained four transit light curves of HAT-P-11b (PI Deming, program ID 80128) using the IRAC instrument: two visits at 3.6 μm (2011 Jul 07 and Aug 15) and two visits at 4.5 μm (2011 Aug 05 and Aug 29). The telescope observed in sub-array mode with a cadence of 0.4 s.

The POET analysis started by reading the Spitzer basic calibrated data (BCD) frames (Spitzer pipeline version 18.18.0). POET discarded bad pixels, determined the target position on the detector (fitting a two-dimensional Gaussian function), and calculated aperture photometry to produce a raw light curve. For each event, we tested circular apertures with radii ranging from 1.75 to 4.0 pixels (in 0.25 pixel increments).

POET simultaneously modeled the out-of-transit system flux, eclipse curve, and telescope systematics with a Levenberg-Marquardt minimizer and a Markov-chain Monte Carlo routine. The Spitzer IRAC systematics include temporal and intra-pixel sensitivity variations (Charbonneau et al. 2005). We modeled the temporal systematic with a set of time-dependent “ramp” models (polynomial, exponential, and logarithmic functions, and combinations of them; Cubillos et al. 2013, 2014). We modeled the intra-pixel systematics with the Bi-Linearly Interpolated Sub-pixel Sensitivity (BLISS) map model (Stevenson et al. 2012a). We used a Mandel & Agol (2002) model for the transit light curve. The transit model fit the planet-to-star radius ratio (R_p/R_s), transit mid-point time, cosine of inclination, and semi-major axis-to-stellar radius ratio (a/R_s). We adopted the same limb-darkening parameters as F14. We set the BLISS map grid size to the RMS of the frame-to-frame pointing jitter; changing the grid size did not impact the transit depth.

We determined the best-fitting aperture by minimizing the standard deviation of the normalized residuals (SDNR) between the data and the best-fitting model. Both 3.6 μm datasets showed a clear SDNR minimum at an aperture radius of 3.0 pixels. Similarly, both 4.5 μm datasets showed a clear SDNR minimum at 2.5 pixels. In all cases, the transit depth remained consistent (within 1σ) across the apertures.

We determined the best-fitting ramp model by minimizing the Bayesian Information Criterion (BIC). The value of BIC between two competing models (\mathcal{M}_1 and \mathcal{M}_2) indicates the fractional probability, $p(\mathcal{M}_2|D)$, of being the correct model (see Cubillos et al. 2014). Tables 5.1 – 5.4 show the best-fitting ramps for each dataset.

Table 5.1: 3.6 μm Visit 1 - Ramp Model Fits

Ramp	R_p/R_s^a	ΔBIC	$p(\mathcal{M}_2 D)$
exponential	0.05835(19)	0.0	...
linear	0.05767(24)	2.3	0.24
quadratic	0.05839(35)	2.9	0.19
logarithmic	0.05766(22)	13.4	1.2×10^{-3}

Note. ^a For this and the following tables, the values quoted in parentheses indicate the 1σ uncertainty corresponding to the least significant digits.

Table 5.2: 3.6 μm Visit 2 - Ramp Model Fits

Ramp	R_p/R_s	ΔBIC	$p(\mathcal{M}_2 D)$
exponential	0.05691(28)	0.0	...
exponential + linear	0.05687(26)	10.9	4.3×10^{-3}
logarithmic	0.05713(32)	20.2	4.1×10^{-5}
quadratic	0.05729(30)	105.8	1.1×10^{-23}

At 3.6 μm , the rising-exponential ramp outperformed the other models in both visits. Since the second visit at 3.6 μm showed evidence of correlated noise (Fig. 5.9), we applied the time-averaging correction factor, and increased the data uncertainties by a factor of 1.5 (see Cubillos et al. 2015). At 4.5 μm , the no-ramp model outperformed the other models in both visits. However, for the first visit, we noted a slight linear trend in the residuals for the no-ramp model; thus, we adopted the linear model.

To obtain final transit depths we ran a joint fit combining all four events. In this fit, we shared the cosine of inclination and a/R_s parameters among all events. We also shared the R_p/R_s parameter between the events in the same wavelength band. Figure 5.10 shows the systematics-corrected light-curve data and joint best-fitting model. Table 5.5 summarizes the joint-fit model setup and results.

Table 5.3: 4.5 μm visit 1 - Ramp Model Fits

Ramp	R_p/R_s	ΔBIC	$p(\mathcal{M}_2 D)$
no ramp	0.05798(33)	0.0	...
linear	0.05813(31)	3.0	0.18
quadratic	0.05807(36)	13.9	9.6×10^{-4}
exponential	0.05814(38)	14.0	9.1×10^{-4}

Table 5.4: 4.5 μm visit 2 - Ramp Model Fits

Ramp	R_p/R_s	ΔBIC	$p(\mathcal{M}_2 D)$
no ramp	0.05814(35)	0.0	...
linear	0.05808(33)	10.9	4.3×10^{-3}
quadratic	0.05812(35)	21.9	1.8×10^{-5}
exponential	0.05814(29)	22.1	1.6×10^{-5}

The Spitzer transit depth of POET and F14 are consistent to each other within 1σ . Furthermore, the depth uncertainties also agreed, suggesting that both reduction pipelines are statistically robust. This is relevant, considering that there have been disagreements when different groups analyze the same exoplanet light curve (Hansen et al. 2014).

5.4.2 Atmospheric Retrieval

We modeled the HAT-P-11b infrared spectra from 1.0 to 5.5 μm . The atmospheric model included HITEMP opacities for H_2O , CO , and CO_2 (Rothman et al. 2010), and HITRAN opacities for CH_4 , NH_3 , C_2H_2 , and HCN (Rothman et al. 2013). The model also included CIA opacities for $\text{H}_2\text{-H}_2$ and $\text{H}_2\text{-He}$ (Richard et al. 2012).

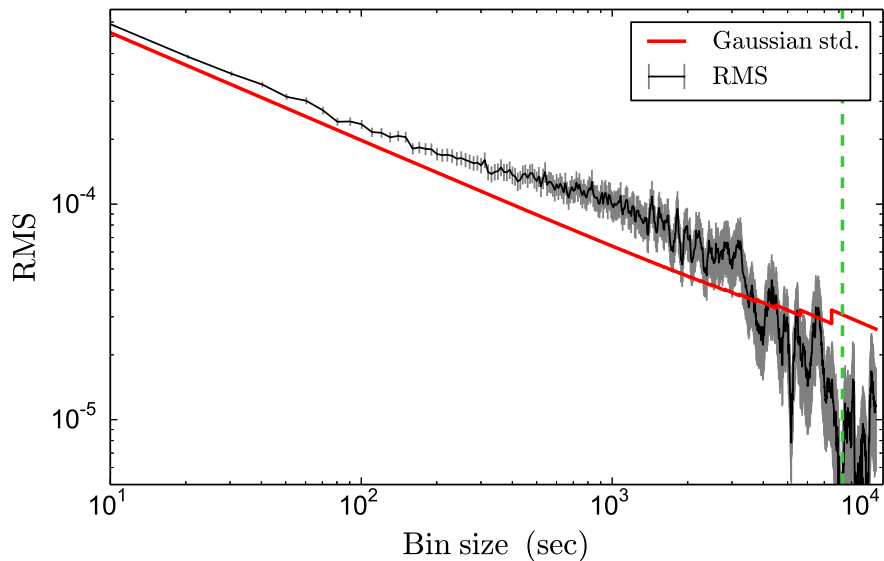


Figure 5.9: Fit residuals’ rms (black curve with 1σ uncertainties) vs. bin size for the second visit at $3.6\ \mu\text{m}$. The red curve shows the expected rms for Gaussian (uncorrelated) noise. The green dashed vertical line marks the transit duration time.

We modeled the atmosphere with a set of 150 layers, equi-spaced in log-pressure, ranging from 10^{-2} to 10^{-8} bar. We produced an initial temperature profile ranging from 785 K at the top of the atmosphere to 1030 K at the bottom of the atmosphere. TEA calculated the initial thermochemical-equilibrium abundances (Fig. 5.11, bottom left) for this atmospheric model, assuming solar elemental abundances (Asplund et al. 2009). H_2 and He represent the bulk of the atmospheric composition, with abundances of $\sim 85\%$ and $\sim 15\%$, respectively.

For the calculation of the line-transition opacities, we set a cutoff at 10^{-6} times the strongest lines. This threshold preserves over $\sim 99\%$ of the total opacity per channel, while significantly speeding up the line-by-line calculations.

Table 5.5: HAT-P-11b Best Joint-fit Eclipse Light-curve Parameters

Waveband (μm)	3.6 (visit 1)	3.6 (visit 2)	4.5 (visit 1)	4.5 (visit 2)
Mean x position (pix)	14.91	14.89	14.61	14.74
Mean y position (pix)	15.13	15.12	15.06	15.02
x -position consistency ^a (pix)	0.004	0.005	0.012	0.010
y -position consistency ^a (pix)	0.011	0.006	0.005	0.004
Aperture photometry radius (pixels)	3.0	3.0	2.5	2.5
System flux F_s (μJy)	469650(13)	468700(17)	285088.9(7.3)	285512.3(5.3)
Transit midpoint (MJD_{UTC}) ^b	3630.7152(16)	3309.5283(16)	3630.7152(16)	3309.5283(16)
Transit midpoint (MJD_{TDB}) ^b	3630.7159(16)	3309.5290(16)	3630.7159(16)	3309.5290(16)
Transit duration (t_{4-1} , hrs)	2.351(5)	2.351(5)	2.351(5)	2.351(5)
R_p/R_*	0.05791(22)	0.05791(22)	0.05816(25)	0.05816(25)
$\cos(i)$ (deg)	89.52(12)	89.52(12)	89.52(12)	89.52(12)
a/R_*	16.664(89)	16.664(89)	16.664(89)	16.664(89)
Limb darkening coefficient, c_1	0.5750	0.5750	0.6094	0.6094
Limb darkening coefficient, c_2	-0.3825	-0.3825	-0.7325	-0.7325
Limb darkening coefficient, c_3	0.3112	0.3112	0.7237	0.7237
Limb darkening coefficient, c_4	-0.1099	-0.1099	-0.2666	-0.2666
Ramp equation ($R(t)$)	Rising exp.	Rising exp.	Linramp	None
Ramp, linear term (r_1)	0.00077(27)	...
Ramp, exponential term (t_0)	-13.7(3.1)	29.8(2.6)
Ramp, exponential term (r_1)	-18.3(2.4)	11.5(1.6)
Number of free parameters ^c	7	7	6	5
Total number of frames	62592	62592	62592	62592
Frames used ^d	57999	56150	60962	62229
Rejected frames (%)	7.34	10.29	2.60	0.58
BIC	206372.4	206372.4	206372.4	206372.4
SDNR	0.0031105	0.0031215	0.0042603	0.0042751
Uncertainty scaling factor	0.980	1.477	1.083	1.086
Photon-limited S/N (%)	85.31	56.99	85.95	85.61

Notes.
^a rms frame-to-frame position difference.

^b $\text{MJD} = \text{BJD} - 2,450,000$.

^c In the individual fits.

^d We exclude frames during instrument/telescope settling, for insufficient points at a given BLISS bin, and for bad pixels in the photometry aperture.

The retrieval model included a total of nine free parameters. Three parameters, $\log \kappa$, $\log \gamma_1$, and β of the three-stream Eddington approximation model, fit the temperature profile (while fixing $\alpha = 0.0$). Four additional parameters scaled the log-abundance profiles of H_2O , CH_4 , CO , and CO_2 (while keeping the abundances of NH_3 , C_2H_2 , and HCN fixed at their initial values). One parameter fit the planet radius at 0.1 bar. Finally, following F14, a free parameter fit the offset of the WFC3 transit-depth data relative to the Spitzer data.

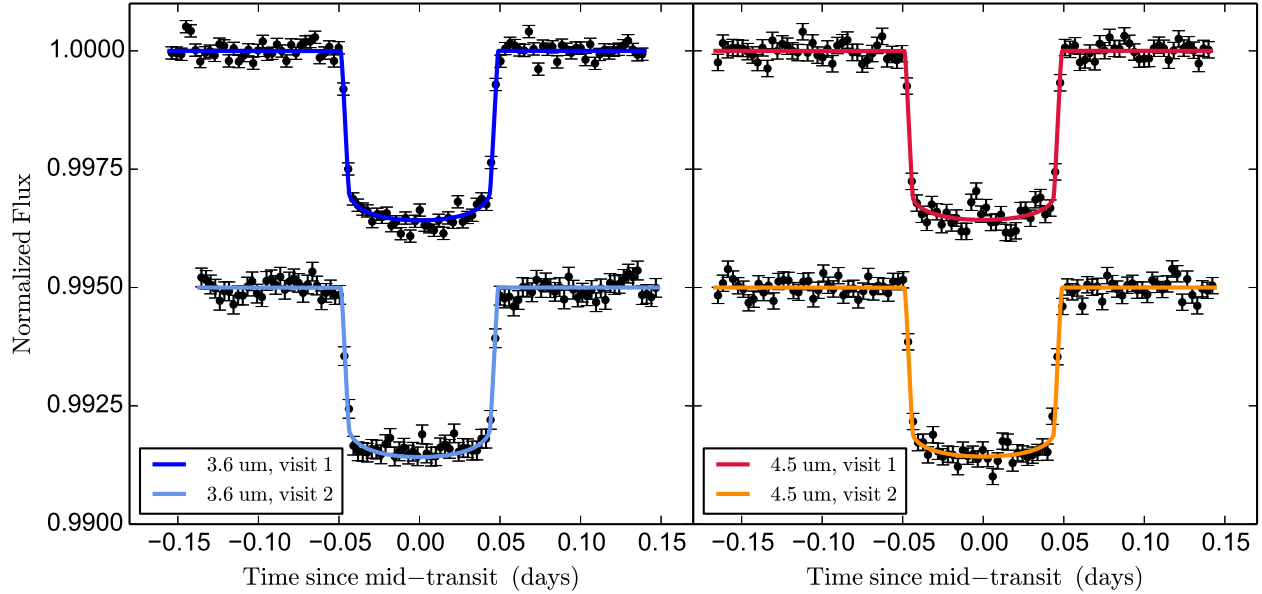


Figure 5.10: Normalized, systematics-corrected Spitzer HAT-P-11b transit light curves (black points) with the best-fitting models (colored solid curves). The error bars denote the 1σ uncertainties. For clarity, we binned the data points and vertically shifted the curves.

Figure 5.11 shows the atmospheric retrieval results. Our best-fitting model provided a good description of the dataset. BART estimated a WFC3 offset of 120 ± 20 p.p.m (shifted downwards) between the WFC3 and Spitzer data. This agrees at the $1-2\sigma$ level with the best-fitting offset of F14. BART found a best-fitting 0.1 bar planetary radius of $29,750 \pm 200$ km. The CO and CO₂ abundances remained unconstrained (flat posterior histograms). This is consistent with the weak absorption pattern from these molecules at wavelengths shorter than $4 \mu\text{m}$. The best option to detect CO and CO₂ would be through their strong absorption bands in the $4.5 \mu\text{m}$ filter. However, our two Spitzer channels have nearly equal depths. The CH₄ posterior histogram is nearly flat, showing a slight, insignificant peak above 10^{-4} .

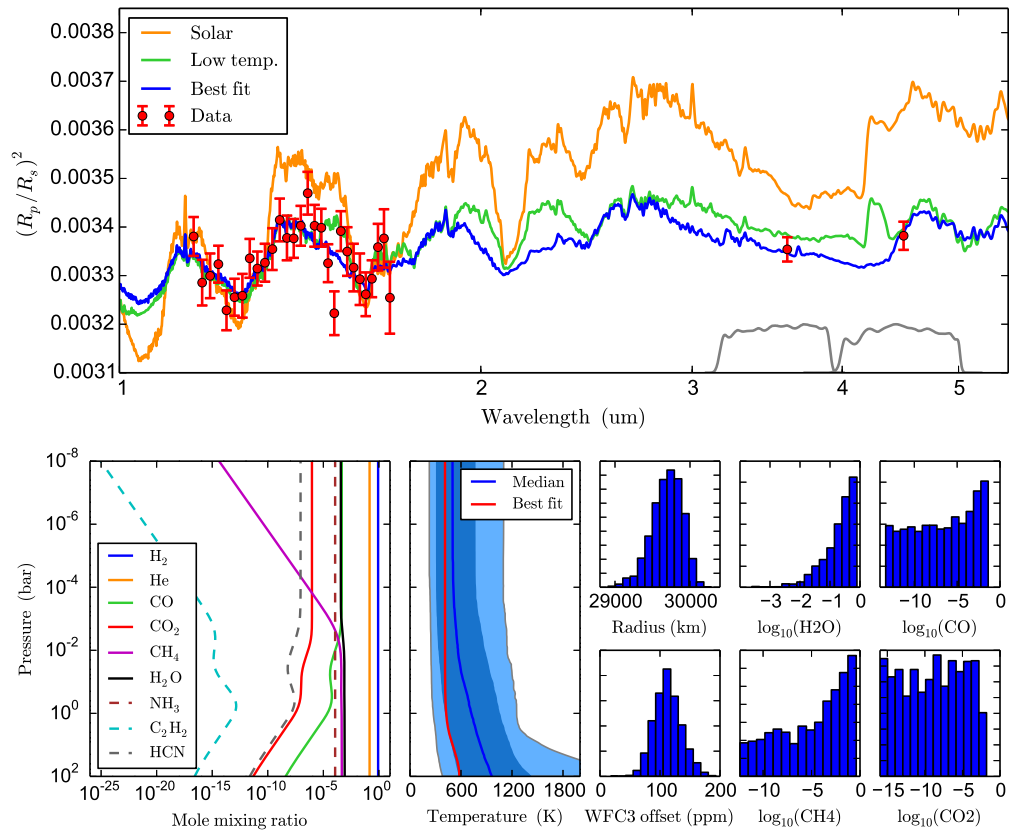


Figure 5.11: **Top:** HAT-P-11b transmission spectra. The red points with error bars denote the HST WFC3 (1 – 2 μm) and Spitzer IRAC (3.6 and 4.5 μm) data with 1σ uncertainties. The WFC3 points were adjusted downwards according to the retrieved best-fitting offset (121 p.p.m.). The blue curve shows the BART-retrieved best-fitting spectrum. The orange and green curves show sample models with solar abundances at equilibrium (~ 900 K) and low (~ 400 K) temperatures, respectively. The gray curves at the bottom show the Spitzer transmission filters. **Bottom:** The left panel shows the initial thermochemical-equilibrium abundances of the atmospheric model. The central panel shows the posterior distribution of the temperature profile. The dark and light regions denote the 68% and 95% credible regions (1 and 2σ). The right panels show the posterior histograms for the 0.1 bar radius, the WFC3 offset, and the 0.1 bar abundances of H_2O , CH_4 , CO , and CO_2 .

The constraint on the H_2O abundance is the most interesting case. The H_2O abundance posterior suggests an enhancement above 100 times the solar abundance. The best-fitting and mean abundances are 120 times and 230 times the solar abundance. Our estimated atmospheric compositions agree well with the results from F14, finding an enhancement in heavy elements and a robust detection of H_2O .

The key to constraining the water abundance is the amplitude of the absorption features, which is related to the atmospheric scale height:

$$H = \frac{k_B T}{\mu g}, \quad (5.30)$$

where μ is the mean molecular mass. The scale height is the characteristic (vertical) distance over which the pressure changes by a factor of e . For a smaller scale height, the atmosphere changes from optically thin to optically thick over a smaller altitude range.

A higher abundance of heavy elements implies a higher mean molecular mass, and hence a smaller scale height. Then, the amplitude of the modulation spectrum is smaller (compare, for example, the amplitudes of the solar and best-fitting models in Fig. 5.11, top panel). Equivalently, lower temperatures would also decrease the scale height, as shown in Fig. 5.11. The higher H₂O abundance, thus, allows BART to match the amplitude of the spectrum between 1 and 2 μm .

5.5 Discussion

5.5.1 *Open Source, Open Development*

We designed BART as an open-source, open-development project. The project's license will let anybody access, copy, modify, and redistribute the code. Researchers can freely use the BART code for publications, as long as they make public any modification to the code along with the scientific article. With each publication, we will include a compendium to reproduce all of the BART analyses from the scientific article. We believe that reproducibility is one of the main principles of the scientific method, thus we encourage the community to:

1. Promote ‘Reproducible Research’ (Stodden 2009). As computer programs increase in complexity, the ability to reproduce an experiment solely from an article’s description demands a significant time investment, or worse, the article may not contain all relevant information. The idea of reproducible research is to allow anyone to reproduce any published experiment.
2. Make exoplanet characterization a community effort, rather than individual attempts. Planetary atmospheres modeling is a multi-disciplinary endeavor involving: radiative processes, atmospheric chemistry, circulation dynamics, cloud physics, and more. The modular design of BART allows members of the scientific community to directly contribute their expertise with ideas and code.
3. Promote code verification. Although the independent groups properly test their own models, there is a lack of code verification between competing models. By making the inputs and outputs public, members of the community can directly compare the results from different codes for the same input. By making the source code public, we facilitate code debugging and verification.

5.5.2 *Conclusions*

Here we presented the open-source, open-development BART code to characterize exoplanet atmospheres in a statistically-robust manner. The project’s source code and documentation are available at <https://github.com/exosports/BART>. The BART package includes three self-sufficient sub-modules: (1) the Transit radiative-transfer code (<https://github.com/exosports/transit>), (2) the TEA thermochemical-equilibrium abundances code (<https://github.com/dzesmin/TEA>), and (3) the MC³ Bayesian statistical module (<https://github.com/pcubillos/MCcubed>). The documentation includes a user manual describing the inputs, outputs, and usage of the BART code. A second, more-detailed code manual describes in depth the routines and file structures of the code.

The Transit module solves the radiative-transfer equation to calculate transmission or emission spectra. It accounts for line-transition and collision-induced absorption opacities, which can be provided as line-by-line or cross-section files. The Transit spectra agree well with C. Morley's model emission spectra and Sharp & Burrows (2007) opacity spectra. The TEA module is further described in Blečić et al. (2015a). The MC³ statistics module is a general-purpose model-fitting package written in Python and C (Cubillos et al. 2015). MC³ provides least-square minimization, advanced MCMC sampling, and correlated-noise estimation algorithms.

The BART project is the outcome of the collaborative effort by the UCF exoplanet group members and is jointly presented in this work, in Harrington et al. (2015), and in Blečić et al. (2015b). The following list details the tasks where I contributed substantially. I revised and modified the complete Transit code from P. Rojo to improve the code performance, improve the code design, add comments, and remove obsolete functions. I implemented Transit's opacity-grid calculations and interpolation, Simpson integration, opacity threshold, and Voigt-profile precalculation. I refactored the CIA code into a general code that handles cross-section absorption data for single or pairs of species. I reimplemented the H₂O line reader for the Partridge & Schwenke database from C to Python and added support for the HITRAN, TiO Schwenke, and VO Plez databases. I implemented the CTIPS submodule to calculate the partition function for the HITRAN species. For the BART module, I implemented the three-stream Eddington temperature-profile model, developed the MPI communication framework, and implemented the spectrum integration over the filter transmission. I wrote the MC³ statistical module and documentation.

The diversity of physical processes involved in atmospheric modeling calls for the development of collaborative projects. By releasing our code to the community, we hope to (1) allow reproducible research, (2) provide access to the routines discussed here, (3) promote open development and cross validation of the software tools used in the field, and (4) promote exoplanet characterization as a collaborative effort.

We further applied the BART atmospheric analysis to the Spitzer and Hubble transit observations of HAT-P-11b. Our results agree well with those of Fraine et al. (2014). Both analyses detected H₂O absorption and estimated an enhancement in heavy elements of a few hundred times the solar composition. Other species abundances (CH₄, CO, and CO₂) remained unconstrained. The low signal-to-noise ratio and limited spectral coverage of present measurements limit the scientific yield from these observations. The analysis of HAT-P-11b is an example of these difficulties. The unknown absolute calibration of the system flux introduces an uncertainty in the transit-depth measurements between non-simultaneous observations. This extra degree of freedom can mask spectral features, limiting our capacity to lay atmospheric constraints.

Fortunately, the field has motivated new efforts to calculate laboratory opacity data at higher temperatures (e.g., Tennyson & Yurchenko 2012, Hargreaves et al. 2012, 2015a,b) and build dedicated instrumentation. The laboratory advancements complement the development of next-generation telescopes; for example, JWST's large collecting area (~ 6.5 m primary diameter), fine resolving power ($R = 4 - 3000$), and broad spectral coverage ($\sim 0.6 - 28.0$ μm) will unveil unprecedented details of these worlds. The tools we have presented here prepare us to better study the diversity of exoplanet atmospheres that will be observed in the future.

5.6 Acknowledgements

We thank Caroline Morley and Jonathan Fortney for useful conversations and for providing radiative-transfer spectra for comparison. We thank contributors to SciPy, Matplotlib, and the Python Programming Language; the open-source development website GitHub.com; and contributors to the free and open-source community. PC is supported by the Fulbright Program for Foreign Students. Support for this work was provided by NASA through the Science Mission Directorate's Planetary Atmospheres Program, grant NNX12AI69G, and the Astrophysics Data Analysis Program, grant NNH12ZDA001N. Part of this work is based on observations made with the Spitzer Space Telescope, which is operated by the Jet Propulsion Laboratory, California Institute of Technology under a contract with NASA.

5.7 List of References

- Agúndez, M., Venot, O., Iro, N., Selsis, F., Hersant, F., Hébrard, E., & Dobrijevic, M. 2012, *A&A*, 548, A73
- Asplund, M., Grevesse, N., Sauval, A. J., & Scott, P. 2009, *ARA&A*, 47, 481
- Bakos, G. Á., Torres, G., Pál, A., Hartman, J., Kovács, G., Noyes, R. W., Latham, D. W., Sasselov, D. D., Sipőcz, B., Esquerdo, G. A., Fischer, D. A., Johnson, J. A., Marcy, G. W., Butler, R. P., Isaacson, H., Howard, A., Vogt, S., Kovács, G., Fernandez, J., Moór, A., Stefanik, R. P., Lázár, J., Papp, I., & Sári, P. 2010, *ApJ*, 710, 1724
- Benneke, B. 2015, *ArXiv e-prints*, 1504.07655
- Benneke, B. & Seager, S. 2012, *ApJ*, 753, 100

- Biddle, L. I., Pearson, K. A., Crossfield, I. J. M., Fulton, B. J., Ciceri, S., Eastman, J., Barman, T., Mann, A. W., Henry, G. W., Howard, A. W., Williamson, M. H., Sinukoff, E., Dragomir, D., Vican, L., Mancini, L., Southworth, J., Greenberg, A., Turner, J. D., Thompson, R., Taylor, B. W., Levine, S. E., & Webber, M. W. 2014, *MNRAS*, 443, 1810
- Blecic, J., Harrington, J., & Bowman, M. O. 2015a, submitted
- Blecic, J., Harrington, J., Cubillos, P., Rojo, P., Bowman, M. O., Foster, A. S. D., Stemm, M., & Lust, N. B. 2015b, in prep.
- Bonfils, X., Delfosse, X., Udry, S., Forveille, T., Mayor, M., Perrier, C., Bouchy, F., Gillon, M., Lovis, C., Pepe, F., Queloz, D., Santos, N. C., Ségransan, D., & Bertaux, J.-L. 2013, *A&A*, 549, A109
- Borysow, A., Jorgensen, U. G., & Fu, Y. 2001, *J. Quant. Spec. Radiat. Transf.*, 68, 235
- Broeg, C., Fortier, A., Ehrenreich, D., Alibert, Y., Baumjohann, W., Benz, W., Deleuil, M., Gillon, M., Ivanov, A., Liseau, R., Meyer, M., Oloffson, G., Pagano, I., Piotto, G., Pollacco, D., Queloz, D., Ragozzini, R., Renotte, E., Steller, M., & Thomas, N. 2013, in *European Physical Journal Web of Conferences*, Vol. 47, 3005
- Burrows, A. & Sharp, C. M. 1999, *ApJ*, 512, 843
- Campo, C. J., Harrington, J., Hardy, R. A., Stevenson, K. B., Nymeyer, S., Ragozzini, D., Lust, N. B., Anderson, D. R., Collier-Cameron, A., Blecic, J., Britt, C. B. T., Bowman, W. C., Wheatley, P. J., Lored, T. J., Deming, D., Hebb, L., Hellier, C., Maxted, P. F. L., Pollaco, D., & West, R. G. 2011, *ApJ*, 727, 125
- Castelli, F. & Kurucz, R. L. 2004, *ArXiv Astrophysics e-prints*, 0405087
- Charbonneau, D., Allen, L. E., Megeath, S. T., Torres, G., Alonso, R., Brown, T. M., Gilliland, R. L., Latham, D. W., Mandushev, G., O'Donovan, F. T., & Sozzetti, A. 2005, *ApJ*, 626, 523

- Cubillos, P., Harrington, J., Loredano, T., Lust, N., Blečić, J., & Stemm, M. 2015, in prep.
- Cubillos, P., Harrington, J., Madhusudhan, N., Foster, A. S. D., Lust, N. B., Hardy, R. A., & Bowman, M. O. 2014, *ApJ*, 797, 42
- Cubillos, P., Harrington, J., Madhusudhan, N., Stevenson, K. B., Hardy, R. A., Blečić, J., Anderson, D. R., Hardin, M., & Campo, C. J. 2013, *ApJ*, 768, 42
- Dressing, C. D. & Charbonneau, D. 2015, *ApJ*, 807, 45
- Eriksson, G. 1971, *Acta Chem.Scand.*
- Fortney, J. J. 2005, *MNRAS*, 364, 649
- Fraine, J., Deming, D., Benneke, B., Knutson, H., Jordán, A., Espinoza, N., Madhusudhan, N., Wilkins, A., & Todorov, K. 2014, *Nature*, 513, 526
- Fressin, F., Torres, G., Charbonneau, D., Bryson, S. T., Christiansen, J., Dressing, C. D., Jenkins, J. M., Walkowicz, L. M., & Batalha, N. M. 2013, *ApJ*, 766, 81
- Gelman, A. & Rubin, D. B. 1992, *Statistical Science*, 7, 457
- Goody, R. 1995, *Principles of Atmospheric Physics and Chemistry*, Oxford University Press, ISBN-10: 0195093623, ISBN-13: 9780195093629
- Goorvitch, D. 1994, *ApJS*, 95, 535
- Hansen, C. J., Schwartz, J. C., & Cowan, N. B. 2014, *MNRAS*, 444, 3632
- Hargreaves, R. J., Beale, C. A., Michaux, L., Irfan, M., & Bernath, P. F. 2012, *ApJ*, 757, 46
- Hargreaves, R. J., Bernath, P. F., Bailey, J., & Dulick, M. 2015a, *ApJ*, 813, 12
- Hargreaves, R. J., Buzan, E., Dulick, M., & Bernath, P. F. 2015b, *ArXiv e-prints*, 1510.07010

- Harrington, J., Cubillos, P., Blečić, J., Rojo, P., Bowman, M. O., Foster, A. S. D., Stemm, M., & Lust, N. B. 2015, in prep.
- Huang, X., Freedman, R. S., Tashkun, S. A., Schwenke, D. W., & Lee, T. J. 2013, *J. Quant. Spec. Radiat. Transf.*, 130, 134
- Huang, X., Gamache, R. R., Freedman, R. S., Schwenke, D. W., & Lee, T. J. 2014, *J. Quant. Spec. Radiat. Transf.*, 147, 134
- Jenkins, J. M., Twicken, J. D., Batalha, N. M., Caldwell, D. A., Cochran, W. D., Endl, M., Latham, D. W., Esquerdo, G. A., Seader, S., Bieryla, A., Petigura, E., Ciardi, D. R., Marcy, G. W., Isaacson, H., Huber, D., Rowe, J. F., Torres, G., Bryson, S. T., Buchhave, L., Ramirez, I., Wolfgang, A., Li, J., Campbell, J. R., Tenenbaum, P., Sanderfer, D., Henze, C. E., Catanzarite, J. H., Gilliland, R. L., & Borucki, W. J. 2015, *AJ*, 150, 56
- Knutson, H. A., Benneke, B., Deming, D., & Homeier, D. 2014, *Nature*, 505, 66
- Kreidberg, L., Bean, J. L., Désert, J.-M., Benneke, B., Deming, D., Stevenson, K. B., Seager, S., Berta-Thompson, Z., Seifahrt, A., & Homeier, D. 2014, *Nature*, 505, 69
- Laraia, A. L., Gamache, R. R., Lamouroux, J., Gordon, I. E., & Rothman, L. S. 2011, *Icarus*, 215, 391
- Lee, J.-M., Fletcher, L. N., & Irwin, P. G. J. 2012, *MNRAS*, 420, 170
- Line, M. R., Wolf, A. S., Zhang, X., Knutson, H., Kammer, J. A., Ellison, E., Deroo, P., Crisp, D., & Yung, Y. L. 2013, *ApJ*, 775, 137
- Line, M. R., Zhang, X., Vasisht, G., Natraj, V., Chen, P., & Yung, Y. L. 2012, *ApJ*, 749, 93
- Madhusudhan, N. & Seager, S. 2009, *ApJ*, 707, 24

—. 2010, *ApJ*, 725, 261

Mandel, K. & Agol, E. 2002, *ApJ*, 580, L171

Moses, J. I., Visscher, C., Fortney, J. J., Showman, A. P., Lewis, N. K., Griffith, C. A., Klippenstein, S. J., Shabram, M., Friedson, A. J., Marley, M. S., & Freedman, R. S. 2011, *ApJ*, 737, 15

Nymeyer, S., Harrington, J., Hardy, R. A., Stevenson, K. B., Campo, C. J., Madhusudhan, N., Collier-Cameron, A., Loredó, T. J., Blečić, J., Bowman, W. C., Britt, C. B. T., Cubillos, P., Hellier, C., Gillon, M., Maxted, P. F. L., Hebb, L., Wheatley, P. J., Pollacco, D., & Anderson, D. R. 2011, *ApJ*, 742, 35

Parmentier, V. & Guillot, T. 2014, *A&A*, 562, A133

Partridge, H. & Schwenke, D. W. 1997, *J. Chem. Phys.*, 106, 4618

Pierluissi, J. 1977, *J. Quant. Spec. Radiat. Transf.*, 18, 555

Plez, B. 1998, *A&A*, 337, 495

Richard, C., Gordon, I. E., Rothman, L. S., Abel, M., Frommhold, L., Gustafsson, M., Hartmann, J.-M., Hermans, C., Lafferty, W. J., Orton, G. S., Smith, K. M., & Tran, H. 2012, *J. Quant. Spec. Radiat. Transf.*, 113, 1276

Ricker, G. R., Winn, J. N., Vanderspek, R., Latham, D. W., Bakos, G. Á., Bean, J. L., Bert-Thompson, Z. K., Brown, T. M., Buchhave, L., Butler, N. R., Butler, R. P., Chaplin, W. J., Charbonneau, D., Christensen-Dalsgaard, J., Clampin, M., Deming, D., Doty, J., De Lee, N., Dressing, C., Dunham, E. W., Endl, M., Fressin, F., Ge, J., Henning, T., Holman, M. J., Howard, A. W., Ida, S., Jenkins, J., Jernigan, G., Johnson, J. A., Kaltenegger, L., Kawai, N., Kjeldsen,

H., Laughlin, G., Levine, A. M., Lin, D., Lissauer, J. J., MacQueen, P., Marcy, G., McCullough, P. R., Morton, T. D., Narita, N., Paegert, M., Palle, E., Pepe, F., Pepper, J., Quirrenbach, A., Rinehart, S. A., Sasselov, D., Sato, B., Seager, S., Sozzetti, A., Stassun, K. G., Sullivan, P., Szentgyorgyi, A., Torres, G., Udry, S., & Villaseñor, J. 2014, in *Society of Photo-Optical Instrumentation Engineers (SPIE) Conference Series*, Vol. 9143, 20

Rojo, P. M. 2006, PhD thesis, Cornell University

Rothman, L. S., Gordon, I. E., Babikov, Y., Barbe, A., Chris Benner, D., Bernath, P. F., Birk, M., Bizzocchi, L., Boudon, V., Brown, L. R., Campargue, A., Chance, K., Cohen, E. A., Coudert, L. H., Devi, V. M., Drouin, B. J., Fayt, A., Flaud, J.-M., Gamache, R. R., Harrison, J. J., Hartmann, J.-M., Hill, C., Hodges, J. T., Jacquemart, D., Jolly, A., Lamouroux, J., Le Roy, R. J., Li, G., Long, D. A., Lyulin, O. M., Mackie, C. J., Massie, S. T., Mikhailenko, S., Müller, H. S. P., Naumenko, O. V., Nikitin, A. V., Orphal, J., Perevalov, V., Perrin, A., Polovtseva, E. R., Richard, C., Smith, M. A. H., Starikova, E., Sung, K., Tashkun, S., Tennyson, J., Toon, G. C., Tyuterev, V. G., & Wagner, G. 2013, *J. Quant. Spec. Radiat. Transf.*, 130, 4

Rothman, L. S., Gordon, I. E., Barber, R. J., Dothe, H., Gamache, R. R., Goldman, A., Perevalov, V. I., Tashkun, S. A., & Tennyson, J. 2010, *J. Quant. Spec. Radiat. Transf.*, 111, 2139

Schwenke, D. W. 1998, *Faraday Discussions*, 109, 321

Sharp, C. M. & Burrows, A. 2007, *ApJS*, 168, 140

Showman, A. P., Fortney, J. J., Lewis, N. K., & Shabram, M. 2013, *ApJ*, 762, 24

Stevenson, K., Harrington, J., Nymeyer, S., Madhusudhan, N., Seager, S., Bowman, W. C., Hardy, R. A., Deming, D., Rauscher, E., & Lust, N. B. 2010, *Nature*, 464, 1161

Stevenson, K. B., Harrington, J., Fortney, J. J., Lored, T. J., Hardy, R. A., Nymeyer, S., Bowman, W. C., Cubillos, P., Bowman, M. O., & Hardin, M. 2012a, *ApJ*, 754, 136

Stevenson, K. B., Harrington, J., Lust, N. B., Lewis, N. K., Montagnier, G., Moses, J. I., Visscher, C., Blečić, J., Hardy, R. A., Cubillos, P., & Campo, C. J. 2012b, *ApJ*, 755, 9

Stodden, V. 2009, *Computing in Science & Engineering*, 11, 35

Tennyson, J. & Yurchenko, S. N. 2012, *MNRAS*, 425, 21

ter Braak, C. J. F. 2006, *Statistics and Computing*, 16, 239

ter Braak, C. J. F. & Vrugt, J. A. 2008, *Statistics and Computing*, 18, 435

Waldmann, I. P., Tinetti, G., Rocchetto, M., Barton, E. J., Yurchenko, S. N., & Tennyson, J. 2015, *ApJ*, 802, 107

Wheatley, P. J., Pollacco, D. L., Queloz, D., Rauer, H., Watson, C. A., West, R. G., Chazelas, B., Loudon, T. M., Walker, S., Bannister, N., Bento, J., Burleigh, M., Cabrera, J., Eig Müller, P., Erikson, A., Genolet, L., Goad, M., Grange, A., Jordán, A., Lawrie, K., McCormac, J., & Neveu, M. 2013, in *European Physical Journal Web of Conferences*, Vol. 47, 13002

White, W. B., Johnson, S. M., & Dantzig, G. B. 1958, *J. Chem. Phys.*, 28, 751

Yurchenko, S. N. & Tennyson, J. 2014, *MNRAS*, 440, 1649